Building the Foundation for a Hydrogeology Model of the Rio Hondo Watershed, NM

by

Jevon J. Harding

Submitted in Partial Fulfillment

of the Requirements for the Degree of

Master of Science in Hydrology

New Mexico Institute of Mining and Technology

Socorro, New Mexico

August, 2012

"What makes the desert beautiful," said the little prince, "is that somewhere it hides a well."

Antoine de Saint-Exupéry, *The Little Prince*

ABSTRACT

Many hydrogeology models, particularly in mountainous regions, assume that the groundwater divides coincide with topographic surface-water divides. However, even in low permeability areas with high topographic relief, groundwater divides can be influenced by neighboring surface watersheds or can change over time due to different environmental forcings. This implies that a hydrogeology model should encompass an area greater than simply the topographically-defined watershed. This work attempts to frame some objective guidelines for picking an appropriate model width that will account for groundwater divides that may not coincide with surface-water divides.

Hydrogeologic models in mountainous regions will also often assume that groundwater flow only occurs in shallow layers and arbitrarily assigns a bottom model boundary at some "impermeable" bedrock depth. However, many mountainous regions, even in low permeability crystalline settings, can still host significant amounts of deep groundwater flow. These deep flows can be significant contributors to basin aquifers abutting the mountain block. This mountain block recharge (MBR) is particularly relevant for mountain-fronting basin aquifers in the western United States since contributions from deep old water indicate an increased buffering capacity against the effects of climate change. We therefore also address how to pick an optimal model thickness that can account for the possibility of deep flowpaths in mountainous areas.

Using COMSOL Multiphysics Earth Science Module, we simulate cross-sections of a 3D regional groundwater flow system using a Tóth-like model. Focusing on one particular valley of interest within the regional model, we analyzed the sensitivity of groundwater discharge and the mean age of that discharge to changes in model width, model thickness, regional slope, local hummock amplitude, permeability decay depth, anisotropy, and heterogeneity in the form of alternating geologic layers. For each of these simulations, we also noted the position of the groundwater divides, since these change location under different environmental conditions. The results of these simulations indicate that in almost all scenarios, model widths that are wider than the surface watershed provide more reliable discharge and mean age results. The surface watershed divides can be substituted for the groundwater divides only under certain circumstances and only if the system is well characterized. For instance, when permeability is known to decay rapidly with depth, the surface watershed is sufficient. But ideally, the model width would encompass the surface watersheds to either side of the watershed of interest. If this is not computationally possible, it is still recommended to extend the boundaries at least to the neighboring topographic lows. An ideal model thickness was defined as the point where the discharge and mean age in the valley of interest, as well as the groundwater divide locations, stop changing. For a base-case scenario tested here, this was approximately 2500 m but this method can also be applied to systems with different environmental conditions to find an ideal model thickness for specific watersheds.

This modeling effort has the goal of laying a foundation for a hydrogeology model to be built for the Rio Hondo watershed in northern NM. In keeping with this aim, field sampling was also carried out in the Rio Hondo watershed and surrounding area in order to establish a baseline characterization of stable

isotopes and major ions in area waters. These results indicate that there is some contribution from deep mountain block groundwater flow to the basin aquifer and surface flows. This makes the guidelines that we outline for objectively choosing model boundaries particularly relevant since they provide a basis for choosing model boundaries that will correctly account for the existence of deep groundwater flow in the Rio Hondo region.

Keywords: Rio Hondo; Taos; New Mexico; hydrogeology; mountain block recharge

ACKNOWLEDGMENTS

This project was funded by NSF NM EPSCoR RII3: "Climate Change Impacts on New Mexico's Mountain Sources of Water." This research would not have been possible without our NM EPSCoR collaborators, particularly Laura Crossey and her students Tyler van Riper and Chad Bryant from UNM, Carlos Ochoa, Sam Fernald, and Dustin Rapp from NMSU and, of course, the NM EPSCoR staff, especially Mary Jo Daniel. In my field area, I am grateful for the generosity of everyone who helped me with my sampling efforts, especially Kei Braun and the Taos Ski Valley Ski Patrol, Ham Brown, Neal Ogden, Eric Patterson, Max Couton, Nancy Turbett, Peter Merscher, and Palemon Martinez. Thanks also to Wayne Sleep from the USDA NRCS, George Ingersoll from the USGS, the Pattison Land Trust, and the US Forest Service Questa Ranger District office.

I would like to thank my research advisor John Wilson for his support and guidance. He helped me find my own way through graduate school and believed in me even when I didn't believe in myself. And, most importantly, he answered all (well, almost all) my late-night, stressed-out texts and emails. Fred Phillips is one of the best and funniest teachers I've ever had. I thank him for his insightful input to this research and for constantly challenging everything I thought I knew. I thank Mark Person for his help on my committee and, of course, for putting up with my gaffes as his teaching assistant - yes, I was the one who dropped a slug down the monitoring well during the slug test lab. I also thank Andy Campbell

for being a constant source of invaluable information without whom there would be no stable isotopes work presented in this thesis.

During my time at New Mexico Tech, I have been lucky enough to be part of a department that has more than once reminded me of just one large, geeky family. I would like to extend my love and thanks to all the members of the Earth and Environmental Science family but in particular, my fellow E&ES graduate students (aka NMT Friday Club), the other members of the Wilson research group, and the demi-goddesses of the E&ES office known as Pat Valentine and Leigh Davidson who did everything in their power to keep me (and the entire department) going in the right direction. I would also like to thank my real family who have loved and supported me through this crazy period in my life called graduate school.

This thesis was typeset with LaTeX[1] by the author.

[1]The LaTeX document preparation system was developed by Leslie Lamport as a special version of Donald Knuth's TeX program for computer typesetting. TeX is a trademark of the American Mathematical Society. The LaTeX macro package for the New Mexico Institute of Mining and Technology thesis format was written for the Tech Computer Center by John W. Shipman.

CONTENTS

LIST OF TABLES

LIST OF FIGURES

This thesis is accepted on behalf of the faculty of the Institute by the following committee:

John Wilson, Advisor

I release this document to the New Mexico Institute of Mining and Technology.

Jevon J. Harding Date

CHAPTER 1

INTRODUCTION

1.1 Background

For both socio-economic and environmental reasons, the Rio Hondo, which drains the Sangre de Cristo Mountains north of Taos, NM, is of vital importance when considering the effects of climate change on New Mexico. Climate models predict a decrease in snowfall and snowpack for New Mexico, meaning this snow-fed mountain watershed is potentially very vulnerable to climate change (NMOSE, 2006b). In this research, we try to build a better understanding of the hydrologic mechanisms in the mountain block and in the adjacent valley. This has important social implications at both the local and the state level. Locally, the lower reaches of the the Rio Hondo provide water to a dozen traditional New Mexican acequia irrigation systems that have been in place for centuries. And as a tributary to the Rio Grande, the Rio Hondo contributes to the state-wide water supply. The Rio Grande and other Western rivers are largely dependent on similar snow-fed mountainous tributaries, so the Rio Hondo is a useful case study to represent other climate-vulnerable rivers in New Mexico and across the western United States.

Although climate and land use change have perhaps lent more urgency to the research described here, interest in the hydrology of this region is nothing new. Due to rising concerns about the growing water demands in Taos Valley, as

well as the requirements of the decades-long Abeyta adjudication process, there have already been several hydrologic studies of the entire Taos Basin (Garrabrant, 1993; Johnson, 1999; Drakos et al., 2004; Barroll et al., 2006). Portions of the Rio Hondo have also specifically been studied in detail. A study of the Arroyo Hondo area describes the hydrogeology of the downstream section of the river, near its confluence with the Rio Grande (Johnson et al., 2009). Other studies have focused on the hydrogeology of the Arroyo Seco area where the Rio Hondo crosses the mountain front (Rawling, 2005; Golder Associates, 2009). This thesis aims to build off of and add to the existing body of work, focusing specifically on determining the subsurface hydrologic connection between the mountain block and the valley aquifer.

The Sangre de Cristo Mountains are composed of igneous and metamorphic rock with low primary permeability but high secondary permeability due to fractures and faults. However, in past work in the Taos Basin, this secondary permeability has been ignored. Hearne and Dewey (1988), for instance, assumed the mountain block itself was impermeable and contributed nothing to the basin aquifer. Any recharge to the valley aquifer from the mountain block was attributed to stream seepage. Another basin-centered model of the Taos Basin used contributions from the mountain block as a boundary condition, calculated using a water budget calibration (Barroll et al., 2006). This method assumed very little, if any, contribution from hydrologic processes occuring within the mountain block itself. In actuality though, significant amounts of water can flow through fractures and faults in the bedrock, creating deep groundwater flow paths that eventually discharge to the valley aquifer (Wilson and Guan, 2004). The mountain block recharge (MBR), or the transfer of subsurface water from the mountain bedrock to the basin aquifer, can be up to 38% of the annual precipitation in a

highly permeable mountain block (Huntley, 1979) although it is likely lower in the less permeable rock of the Sangre de Cristo Mountains. A model using a point-simulation-based approach for the entire Sangre de Cristo range placed the upper bound of MBR at 35% of the water yield (Guan, 2005). A study in the northern Sangre de Cristo Mountains bordering the San Luis Basin calculated MBR as a smaller, but still significant percentage - 14% of average annual precipitation (Huntley, 1979). This estimate agrees with a study in the southern Sangre de Cristos near Santa Fe that calculated that contributions from the mountain block, including subsurface flow from the mountain block, was 13% of annual precipitation (Wasiolek, 1995). Mountain block recharge in the San Gabriel Mountains in California, a crystalline mountain range in California, was calculated to be 16% of the annual precipitation (Umstot and Wilson, 2011). Studies have not been carried out specifically for the central Sangre de Cristos near the Rio Hondo watershed, but these studies from similar geologic environments indicate that MBR could constitute a similar percentage of this region's water budget. Indeed, geologic characterization along the southern edge of the Taos Basin indicates areas where faulting appears to greatly increase MBR to the valley (Bauer et al., 1999). An area near Taos Pueblo, just south of the Rio Hondo, contains certain areas along the mountain front where faults can be conducive to downward groundwater flow (Kelson et al., 2004). Ludington et al. (2004) also suggests that the widespread fractures and faults in the Red River area, just north of Rio Hondo, make the bedrock a significant contributor to groundwater. However, an existing hydrologic model for the Taos Basin assumed that the groundwater contribution from the mountain block was only 1.3% of the annual precipitation (Barroll et al., 2006). If, as suggested above, the mountain block contribution is actually significantly higher, then this assumption could have important implications for

the water budget calculation in the Taos Basin. Seasonal water budgets in the southern Sangre de Cristos also suggest that deep recharge in the mountain block mainly occurs during the winter and spring, indicating a strong dependence on snowpack and snow melt (Wasiolek, 1995). Since these are the factors most likely to be affected by climate change, a better understanding of MBR is necessary for future water management and planning activities in this region.

1.2 Scope

Determining the contributions of MBR in the Rio Hondo area relies on an integrated approach including field observations and mountain block-centered modeling. The eventual objective is to construct a coupled surface and groundwater 3D model for the Rio Hondo watershed. Since this model will also vary temporally, it can actually be considered a true 4D model. In order to lay the foundation for designing this model, this thesis has three main goals:

1) Characterize the physical properties of the watershed (including streamflow, geology, topography, precipitation, and vegetation) in order to constrain proposed hydrological mechanisms.

2) Establish the isotopic and chemical composition of source waters within the Rio Hondo watershed and apply this information to the determination of flow paths and residence times.

3) Determine the appropriate spatial scope (width and depth) for a model that will most accurately represent subsurface flow in the mountain block, as well as surface flow and hillslope processes across the Rio Hondo study watershed.

Chapter 2 focuses on the first goal, discussing the physical characteristics of the Rio Hondo region and providing a compilation of the available spatial and temporal datasets. Chapter 3 addresses the second goal with results from a field sampling campaign to determine the isotopic and chemical composition of different source waters in the region. Chapter 4 attempts to accomplish the third goal by presenting results from a coupled porous flow and solute transport groundwater model of a mountainous area with prescribed head water-table boundary conditions. This modeling exercise helps establish a set of general guidelines for choosing an appropriate boundary extent for models under various physical conditions. While this modeling effort considers generic conditions and can be applied generally to other areas, special attention is paid to the particular conditions found in New Mexico and the Rio Hondo watershed.

CHAPTER 2

DESCRIPTION OF THE RIO HONDO WATERSHED AND SURROUNDING AREA

2.1 Introduction

The Rio Hondo is a perennial river at the northern edge of the Taos Basin in northern New Mexico [Figure 2.1]. It drains a 194 km^2 watershed with headwaters in the Sangre de Cristo Mountains near Taos Ski Valley and Wheeler Peak, the highest point in New Mexico. Apart from the ski resort and surrounding village, the upstream section of the river is largely undeveloped and controlled by Carson National Forest. From the mountain front to the confluence with the Rio Grande, the basin is dominated by traditional Hispanic acequia-irrigated farmland. It empties into the Rio Grande at the Arroyo Hondo Gorge near John Dunne Bridge. In addition to serving as a major source of water to the villages of Taos Ski Valley (Twining) at the upstream end and Valdez and Arroyo Hondo downstream, the Rio Hondo basin also contributes water to the upper Rio Grande, making it one of only three perennial tributaries in the Taos Basin. Like many other Rio Grande tributaries, it is a largely snow-dominated watershed. This makes it more vulnerable to the reduced snowpack and warming temperatures predicted for northern New Mexico due to climate change (NMOSE, 2006b). Therefore, although it is not a large contributor to the river, exploring its hydrology can help us understand similar mountain-fed Rio Grande tributaries. By studying the hydrologic

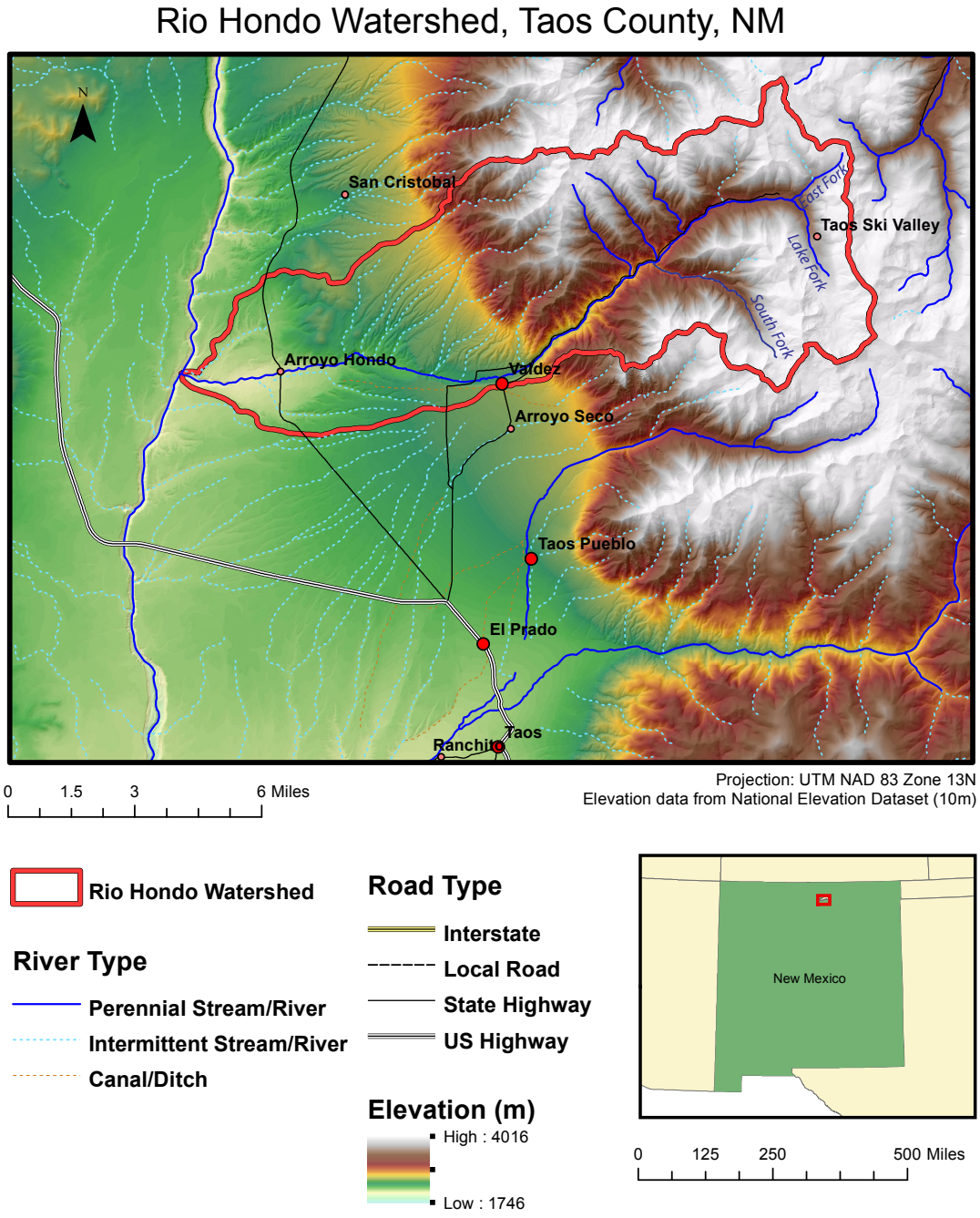

Figure 2.1: Location of the Rio Hondo watershed. Elevation data from USDA (2012).

processes of the Rio Hondo watershed, we can better assess possible impacts of climate and land use change on both local water users and those downstream users and ecosystems dependent on the flows of the Rio Grande and its tributaries.

2.2 Previous Investigations

Apart from a paper about the effects of Taos Ski Valley development on downstream farmers (Rodriguez, 1987), the Rio Hondo has not yet been studied as a single hydrologic unit. However, several previous studies focus on the hydrology of the Taos Basin as a whole and so are particularly relevant for the Rio Hondo, since the river drains into the northern portion of this region. Due to rising concerns about the growing water demands in Taos Valley, there have been several papers aimed at better understanding the hydrology of the area. A USGS report (Garrabrant, 1993) assessed surface and groundwater resources in order to inform water management in the area. The NM Bureau of Geology performed an evaluation of surface-water drainages in the Taos Basin (Johnson, 1999) and then Drakos et al. (2004) evaluated the aquifer systems in the area, further characterizing the groundwater and hydrogeology. This work helped lay the groundwork for the Taos Regional Water Plan (Daniel B. Stephens & Associates, 2008) which described the current water situation and outlined a plan for meeting future water demands in the Taos Water Planning Region.

The decades-long Abeyta adjudication, which aimed to assign all surface-water rights in the basin, also motivated hydrology research in the area. As part of the process, the NM Office of the State Engineer developed a groundwater model to better understand the effects of groundwater development (Barroll et al., 2006) on surface flows. The final adjudication settlement agreement

(NMOSE, 2006a), though not a hydrogeology study per se, is still important for understanding the current distribution of water rights in the Rio Hondo watershed. The settlement requires the use of groundwater to offset some surface-water depletions, which has a significant effect on portions of Arroyo Seco, just south of the Rio Hondo watershed along the mountain-front.

The downstream section of the Rio Hondo near Arroyo Hondo and the confluence with the Rio Grande was the subject of Johnson et al. (2009), which assessed geology and groundwater resources as part of the Aquifer Mapping program by the NM Bureau of Geology. Another section of the watershed that abuts the mountain front near Valdez was the subject of Rawling (2005). This paper also examines the Arroyo Seco and El Salto regions which, while not falling directly into the Rio Hondo watershed, are adjacent to it along the mountain front, making it relevant for any exploration of deep groundwater flow and mountain block recharge in the area. Similarly, Golder Associates (2009) assesses the hydrogeology of the El Salto region as a preliminary step for building a community water supply system.

2.3 Physical Setting

2.3.1 Physiography

The Rio Hondo watershed can be classified under the larger physiographic divisions of the San Luis Basin, a deep sedimentary basin that is part of the Rio Grande rift. The area from the mountain front to the confluence with the Rio Grande falls into the Costilla Plains province of the San Luis Basin. This province is characterized by largely undissected alluvial deposits over underlying basalt layers. It is narrow, only a few miles across, and bounded by the Rio Grande to

the west, the Sangre de Cristos to the east, and the Alamosa Basin at its northern end (Upson, 1939). The agricultural areas within the Costilla Plains portion of the Rio Hondo watershed are characterized by silty or clay loam. The mountainous upstream section is characterized by steep rocky outcrops with only some cobbly loam along the slopes and in the river valley [Figure 2.2].

Like the other perennial rivers in the Taos Basin, the Rio Hondo originates in the Sangre de Cristo Mountains, the eastern prong of the southern Rocky Mountains. The headwaters are located in a steep upper canyon, near the Taos Ski Valley resort, in an area characterized by high relief outcrops of fractured crystalline rock and mixed evergreen and deciduous forest. From there, the river flows westward through an 8-mile mountain valley flanked by the same mix of rocky outcrops and forest. At the mountain front, the river descends into a narrow low-lying agricultural valley at Valdez. This valley, also called the Rio Hondo Canyon, is bounded to the south by a higher flat alluvial plateau at Arroyo Seco and to the north by an extruding tongue of Sangre de Cristo foothills. The river passes through a narrow gorge at the Gates of Valdez (Cañoncito) before spreading into another low-lying, but wider, agricultural valley at Arroyo Hondo. The river passes through a steep narrow gorge again before discharging to the Rio Grande at the John Dunne Bridge. On average, the river runs 4.6 m wide and 0.3 m deep during normal flows. The river bed is comprised of large boulders mixed with cobbles and gravel (Rodriguez, 1987). From Wheeler Peak (4011 m) to the confluence with the Rio Grande (1972 m), the Rio Hondo watershed covers an impressive elevation range of greater than 2000 m.

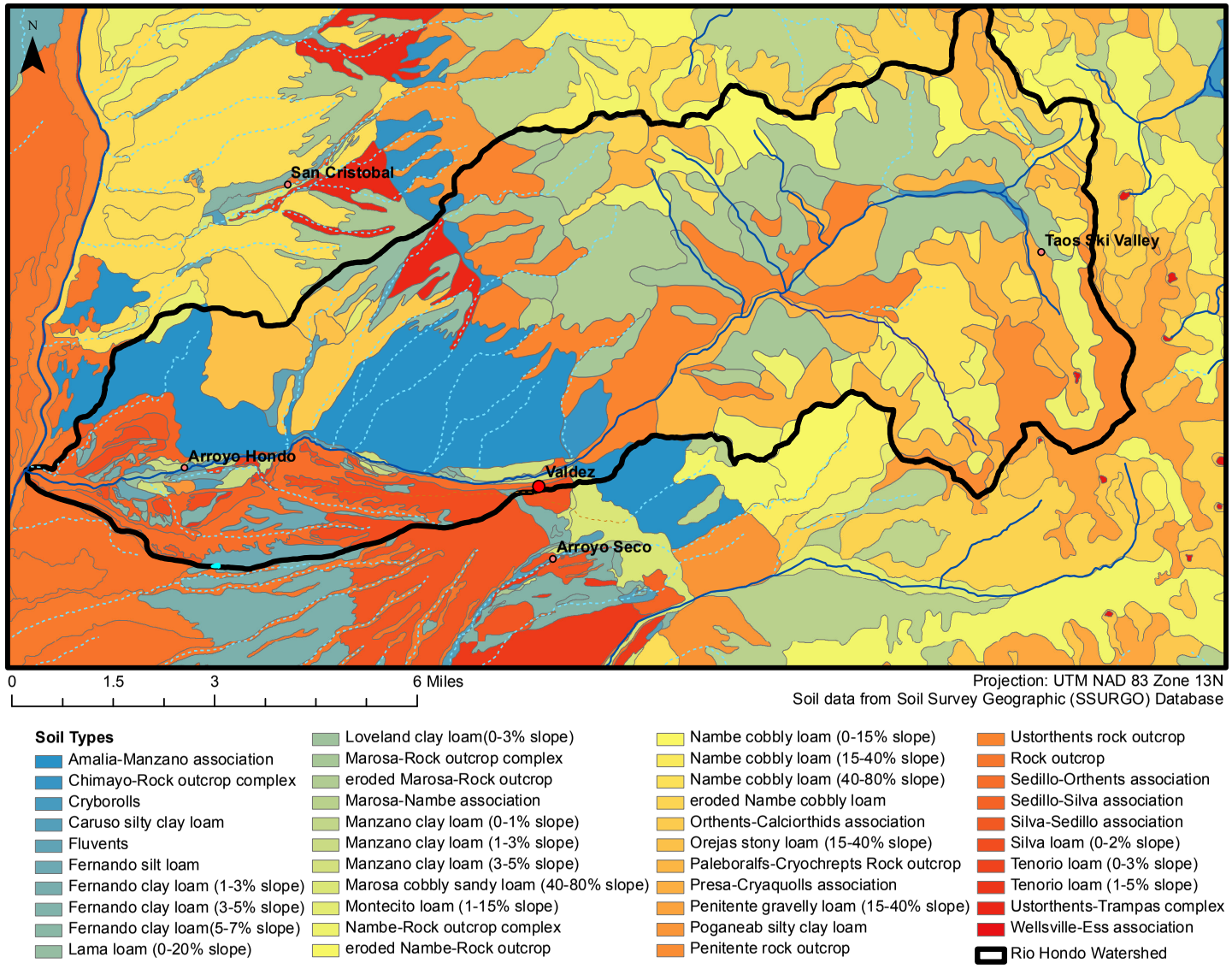

Figure 2.2: Soil types in the Rio Hondo watershed. Map data from USDA (2008).

2.3.2 Climate

The Rio Hondo watershed is a semiarid desert environment characterized by dry, sunny days and often large temperature swings at night. There is a marked difference between the climate of the mountainous region and the climate of the mountain-front basin. The mountains receive more precipitation (51 - 89 cm/yr) than the low-lying basin (18 - 38 cm/yr) (OSU, 2001) [Figure 2.3]. Mountain precipitation is also heavily dependent on snowfall, with snow accounting for 1/3 the annual precipitation, as opposed to only $13 - 18\%$ in the basin. This explains why, while March is the wettest month and June the driest in the mountains, the wettest months in the basin are July and August, with the winter months the driest. Summer thundershowers, often associated with the monsoon season, account for the majority of annual precipitation (Garrabrant, 1993). As well as having vastly different precipitation patterns, the uplands and mountain-front basin also have significantly different temperatures throughout the year. The temperature in the mountains ranges from -16 - 16°C (3 - 61°F) while the basin is consistently warmer, ranging from -12 - 31°C (11 - 87°F). The average annual temperature at the highest point of the watershed is -1.7°C (29°F) compared to 8.3 °C (47°F) in the basin near the confluence with the Rio Grande (OSU, 2001) [Figure 2.4].

2.3.3 Land and Water Use

Carson National Forest controls the majority of land above the mountain front in the Rio Hondo watershed. The village of Taos Ski Valley lies in the valley of the steep upper canyon at Lake Fork. There are also a few private homes and

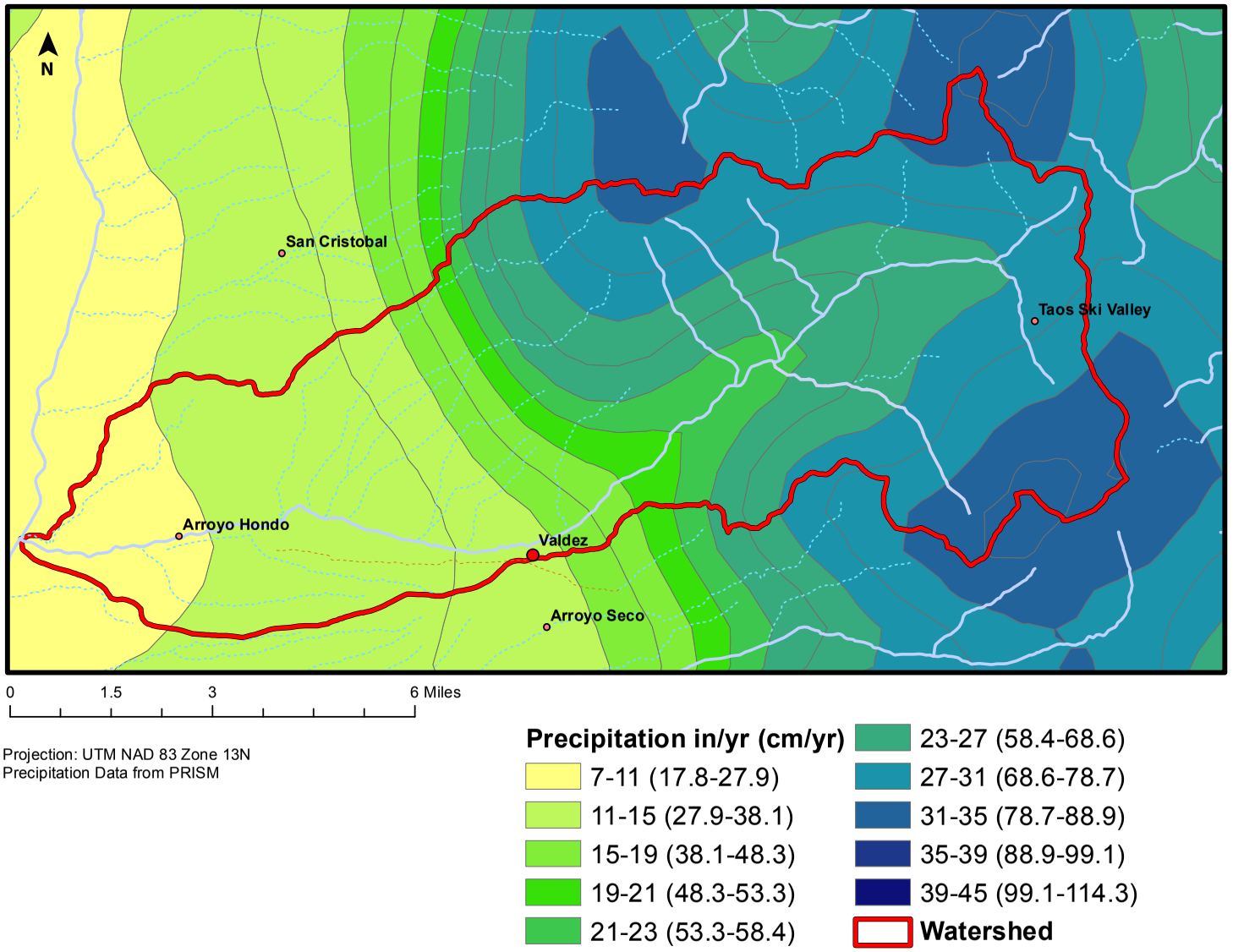

Figure 2.3: Precipitation patterns in the Rio Hondo watershed. Map data from OSU (2001).

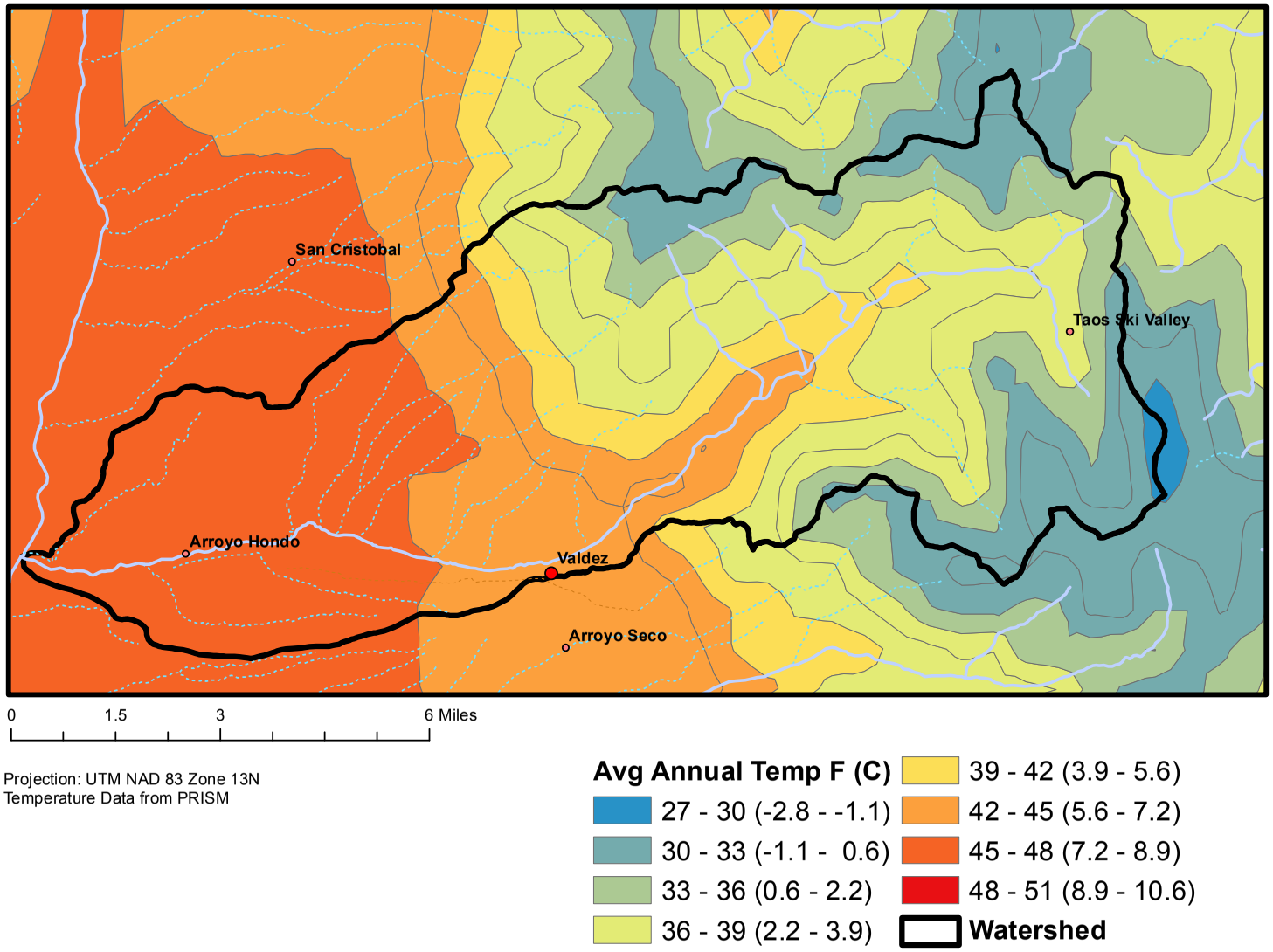

Figure 2.4: Average annual temperature in the Rio Hondo watershed. Map data from OSU (2001).

hotels in the Rio Hondo river valley along the road up to the ski resort. However, besides the east-facing slope that comprises the ski resort, the forested slopes are mostly undeveloped with only some hiking and biking trails maintained by the Forest Service and a private land trust [Figure 2.5]. From the mountain front to the Rio Grande, land use is predominantly for flood-irrigated agricultural and grazing lands as well as roads and private homes.

In the mountains, groundwater is the main source of water. The town and resort of Taos Ski Valley rely on a groundwater spring on the west-facing slope of Lake Fork which provides approximately 128,000 m^3/year (104 acre-feet/yr) (Daniel B. Stephens & Associates, 2008). Some surface-water is also used for snow-making in the winter. Hotels and private residences not supplied by Taos Ski Valley draw water from private wells.

In the basin from the mountain front to the Rio Grande, surface-water comprises 90% of water use, most of which is used for irrigated agriculture (Daniel B. Stephens & Associates, 2008). Most farmers in this area use flood irrigation supplied by irrigation ditches called acequias [Figure 2.6]. Many of these ditches are centuries-old and still governed on the same community-based principles established by the original Spanish settlers in this region. Several Mutual Domestic Water Consumers Associations (MDWCAs) in the area provide groundwater from community wells for domestic use. Annual groundwater withdrawals for these MDWCAs are given in Table 2.1. For additional domestic uses and livestock watering, homeowners and farmers rely on private wells.

2.3.4 Vegetation

Because it covers such a large range in elevation, the study area contains widely differing ecologic zones, including at least 3 of the 5 "life zones" of north

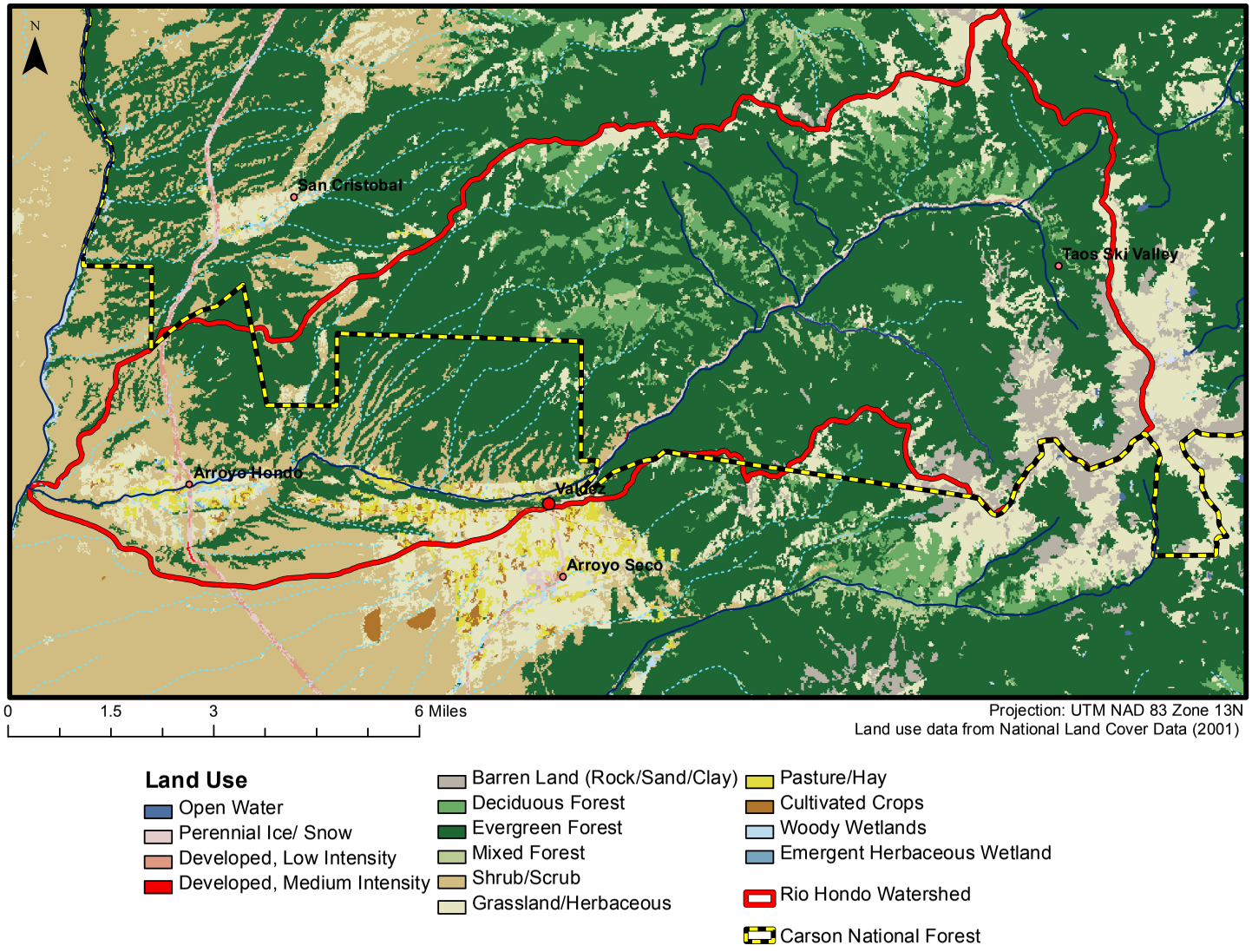

Figure 2.5: Land Use in the Rio Hondo watershed. Map data from USGS (2006).

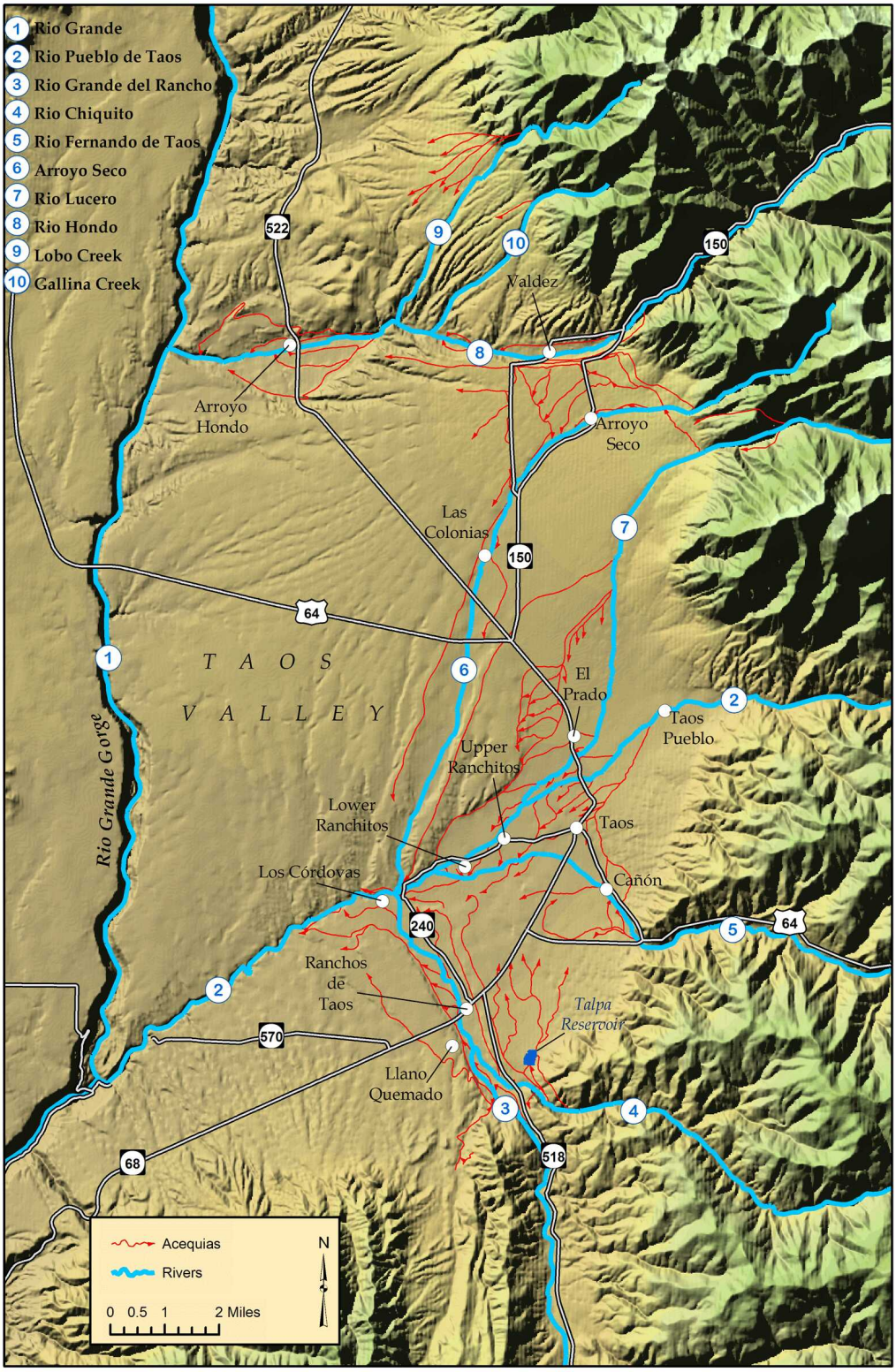

Figure 2.6: Acequias in Taos County. The Rio Hondo is stream no. 8. Map by Rodriguez (2010)

MDCWA Name	Annual Use (acre-feet/yr)	Annual Use (m^3/yr)
Arroyo Seco	35.5	43,800
El Salto	17.6	21,700
Lower Arroyo Hondo	14.2	17,500
Upper Arroyo Hondo	8.7	10,700
Lower Des Montes	38.1	47,000
Upper Des Montes	64.2	79,200
Valdez	5.8	7,200

Table 2.1: Annual groundwater withdrawals for MDWCAs in Rio Hondo area (Daniel B. Stephens & Associates, 2008)

central New Mexico (Rodriguez, 1987). Apart from the permanent ice and alpine meadows found at some of the highest peaks, the top of the watershed is dominated by mixed deciduous and evergreen forest containing pine, spruce, fir, and aspen [Figure 2.7]. This area, which is part of Carson National Forest, extends to the mountain front, where vegetation and ownership abruptly change. The upper river valley at Valdez, which is deeply incised into the basin-fill sediments, largely consists of privately-owned, flood-irrigated agricultural fields. The piedmont to the north of the river at this point is dominated by pinyon-juniper woodland. The lower Rio Hondo valley near Arroyo Hondo, is dominated by agriculture lands interspersed with grazing pastures. The mountain-front mesa near Arroyo Seco, just south of the Rio Hondo valley, is also highly agriculturally developed. Moving westward, however, the mesa transitions from agricultural land to largely sagebrush shrubland all the way to the Rio Grande.

2.4 Geologic Framework

2.4.1 Regional Geologic Setting

The geology of northern New Mexico and our study area is largely dominated by the uplifted Sangre de Cristo Mountains to the east and the south-

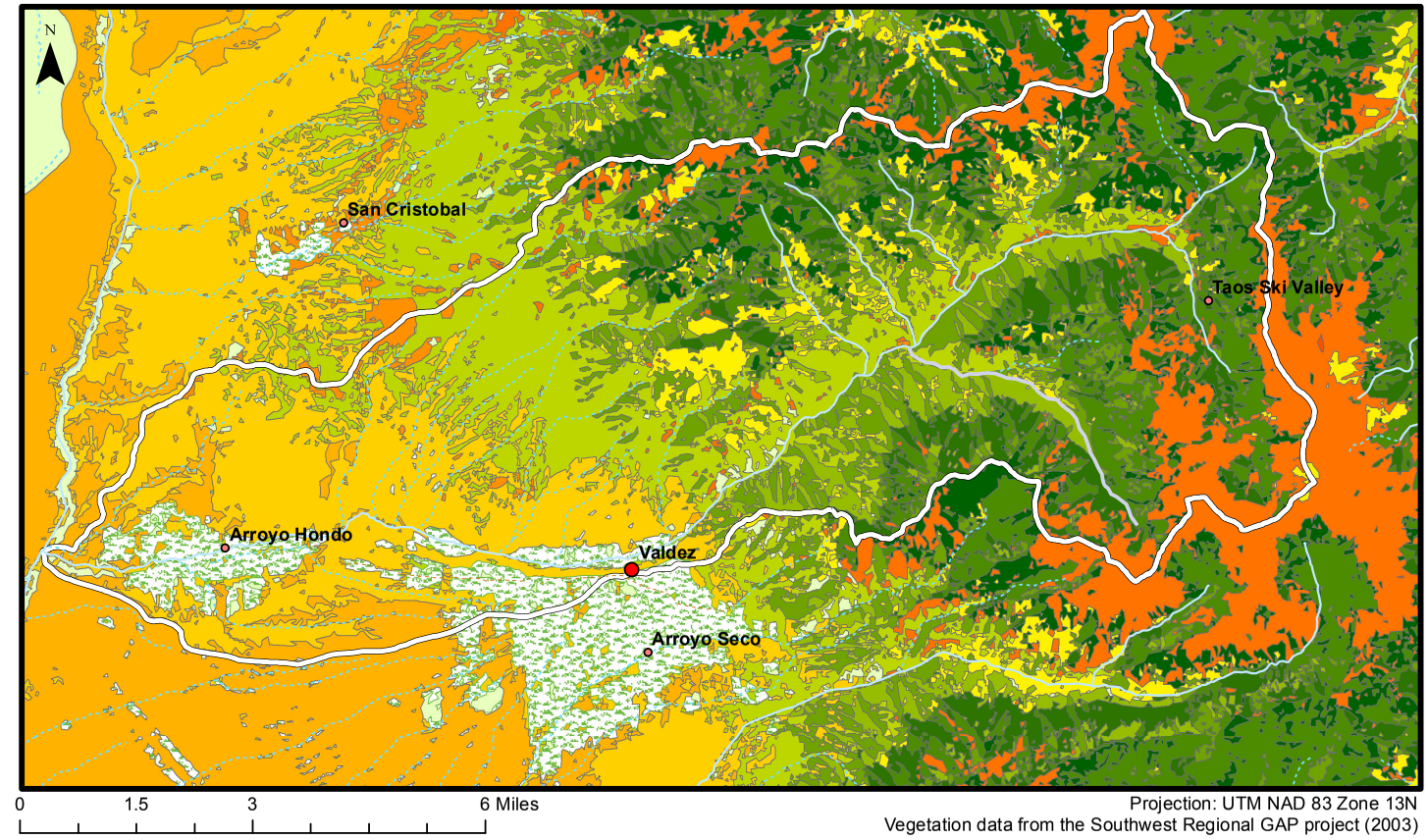

Figure 2.7: Vegetation patterns in the Rio Hondo watershed. Map data from USGS (2004).

ern San Luis Basin bounded by the Rio Grande Gorge to the west. The Sangre de Cristo range forms the narrow-spined eastern prong of the southern Rocky Mountains and lies along a normal fault at the eastern edge of the Rio Grande rift. It is essentially an upthrown fault block of Proterozoic metamorphic and igneous rock intruded by Tertiary granite [Figure 2.8]. The crystalline rock is highly fractured, with small faults and fracture zones evident throughout the mountain block. There is also extensive fracturing along the mountain front, where the mountain block meets the alluvial San Luis Basin.

The San Luis Basin is part of the northern Rio Grande rift and stretches from southern Colorado to just south of the Taos Basin. It is a deep sedimentary basin filled with alluvial sediments weathered from the neighboring mountains. The Santa Fe Group consists of poorly-lithified late Tertiary/early Quaternary rift-fill sediment deposited prior to the formation of the Rio Grande. It is overlain by more recent Quaternary alluvial fan and stream deposits. Cerro Negro, a dacite volcano dome, is visible as bluffs at the Gates of Valdez and extends north of the river as well. The Servilleta basalt formation is often found beneath and intermixed with the Santa Fe, particularly west of Gates of Valdez (geologic description summarized from Rawling (2005)).

2.4.2 Structure

The dominant structural features of this region are associated with the Rio Grande Rift. The rift formed during extensional tectonic activity about 30 million years ago that created deep, sedimentary basins bounded by uplifted mountain blocks along a north-south line through the center of New Mexico. In our study area, the sedimentary basin is the San Luis Basin and the uplifted mountain block

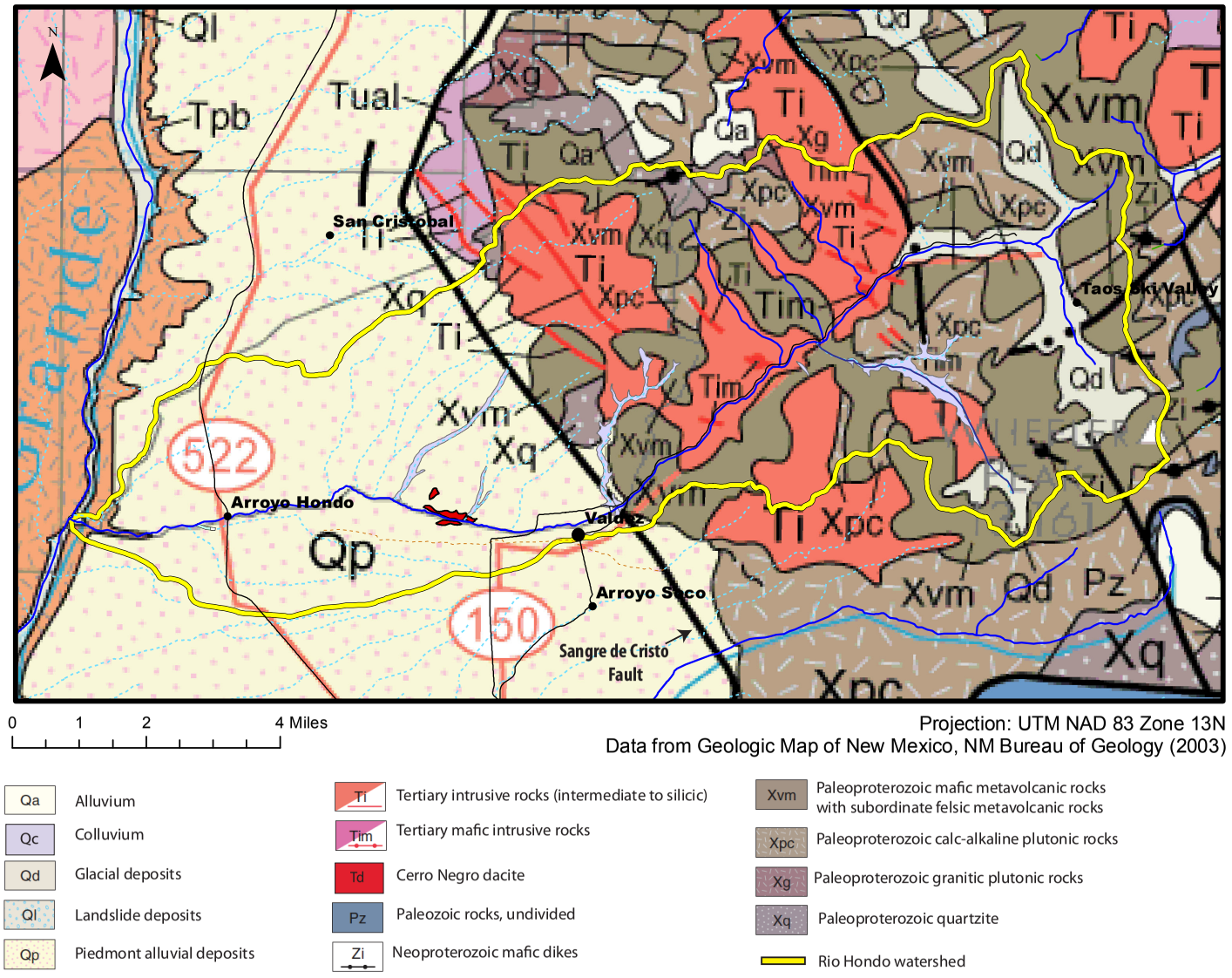

Figure 2.8: Geology of the Rio Hondo watershed. Note the exposed Cerro Negro dacite at Gates of Valdez. Map data from NMBGMR (2003) and G.N. Green (1997).

to the east is the Sangre de Cristo Mountains. The mountain block is uplifted along the Sangre de Cristo fault zone, a major normal fault along the mountain front. The study area actually falls into the Hondo section of the southern Sangre de Cristo fault zone, which stretches from Taos Pueblo in the south to San Cristobal in the north (Ruleman and Machette, 2007). This fault runs southeast to northwest but is not visible at the surface except at the mountain-front mouth of the Rio Hondo Canyon. The Sangre de Cristo fault includes several interlinked fault strands that seem to coalesce into one strand north of Rio Hondo (Rawling, 2005). There are also some smaller faults and fracture zones in the mountain block likely associated with Tertiary granite intrusions and rhyolite dikes. At the western end of the study area, the Rio Hondo is thought to cross the buried Airport Fault, an east-down normal rift fault. In the Hondo Mesa just south of the lower Rio Hondo watershed, it causes 30.5 m of offset in the basalt (Johnson et al., 2009). An aeromagnetic survey of Taos area (Grauch et al., 2004) does provide some information on subsurface features in the basin, indicating the presence of basement prongs that jut into the basin at the mountain front but drop off to the west. However, the survey focuses on the Taos Basin south and west of the Rio Hondo, cutting off much of the western end of Rio Hondo watershed near Arroyo Hondo and unfortunately, does not extend far enough east to be able to interpret structure within the mountain block.

2.4.3 Hydrologic Characteristics of Geologic Units

Although the crystalline rocks in the mountain block generally have low primary permeability, their secondary permeability, created by fractures and faults, make these formations significant components of the hydrologic system. Above

the mountain front, Johnson (1999) estimated that 19% of the annual Rio Hondo discharge comes from groundwater. This is caused by the high permeability and low storage of this fractured crystalline bedrock in the mountain block .

At the mountain front, both Arroyo Seco and Rio Hondo groundwater potentiometric contours (Rawling, 2005) indicate that the streams are gaining and that, in general, groundwater flows east across the mountain front from the crystalline mountain block into the poorly-lithified basin-fill sediments. However, groundwater flow is complicated by the Sangre de Cristo fault zone. Depending on highly localized geologic variations, the interlinked fault strands can cause groundwater to flow up, down, or horizontally. In certain parts of El Salto, for instance, the shallow part of the fault is cemented and mostly impermeable, forcing water to discharge to the basin at depth and then flow upwards as it moves further into the basin. A distributed temperature sensing (DTS) survey along the mountain front in the Rio Hondo riverbed indicated upwelling of ground water flow along the mountain fronting fault zone [Appendix A]. In other places however, water flows directly from mountain block to valley, seemingly without restriction (Rawling, 2005).

Along the mountain front, the Blueberry Hill alluvial fan deposits (part of the Santa Fe group) provide a shallow alluvial aquifer and deeper brecciated zones of fractured bedrock provide a discontinuous but productive bedrock aquifer. Further into the valley, the alluvial sediments overlie buried Cerro Negro dacite which is exposed at the Gates of Valdez. Here, Drakos et al. (2004) and Rawling (2005) found a region of downward flow from the shallow alluvial aquifer to the volcanic rocks. Some wells are able to draw from productive fractured zones in the Cerro Negro dacite but this formation is alternately highly transmissive and

nearly impermeable. The Airport Fault terminates both the Cerro Negro formation and the shallow alluvial aquifer and acts as a downward conduit for groundwater into the Servilleta formation basalts. From here to the Rio Grande Gorge, groundwater wells largely draw from this deeper volcanic-alluvial aquifer.

Within the Rio Hondo river valley itself, the Quaternary alluvial deposits form a stream-connected aquifer system that can be tapped by shallow wells. The river is gaining from the mountain front to the Gates of Valdez but transitions to generally neutral or losing as it flows westward (Rawling, 2005). There are some semi-perched zones in alluvial deposits and terrace beds near the river due to recharge from irrigation and the obstruction of downward flow from the Cerro Negro dacite, which in these areas behaves as an underlying low permeability confining unit. However, in localized fracture or rubble zones, the Cerro Negro itself can also serve as a productive aquifer (Johnson et al., 2009).

2.5 Water Resources

2.5.1 Surface Water Resources

The Rio Hondo is fed by several high elevation tributaries, the largest of which are Lake Fork, East Fork, and South Fork [Figure 2.1]. Williams Lake is the largest water body in the watershed and sits near the headwaters of Lake Fork. Total Rio Hondo mountain discharge is measured at a USGS gauging station right above the mountain front at Valdez and averages 31,889,000 m^3/year (25,853 acre-feet/year) (Johnson, 1999). Highest flows occur during snowmelt in May and June. Lowest flows occur in the winter when much of the river ices over.

The river is a gaining river at the mountain front but transitions to a neutral or losing river as it travels further into the basin past the Gates of Valdez

(Rawling, 2005). When the river crosses through sections underlain by the low permeability dacite flows of the Cerro Negro, the river is neutral since there is essentially no groundwater flow (Johnson et al., 2009). While the stream is predominantly losing downstream of the Gates of Valdez, estimates based on data from a now-defunct USGS gauge near Arroyo Hondo [Appendix B] suggest that the baseflow contributes up to 37% of the stream discharge, at least at this location. This is likely due to gains from permeable Santa Fe basin-fill sediments (Johnson, 1999). The drainages to the south of the river valley on the alluvial plateau do not receive mountain recharge and so only run during storms. Drainages to the north of the river are better developed but are similarly ephemeral.

Since most water in the river comes from snowmelt and mountain groundwater sourced from snow, the potential impacts of climate change are of great concern. NMOSE (2006b) notes that wintertime temperature in New Mexico has increased an average of 0.8°C since the 1960's, with the effect most pronounced in northern New Mexico. Decreases in snowpack and snowfall have been observed, and further decreases are expected, as well as a change in the wintertime ratio of rain to snow precipitation. In the Rio Hondo, streamflow records do not yet indicate a long-term decline in discharge nor a change in timing of snowmelt [Appendix B]. However, due to the factors discussed above, the Rio Hondo basin may be particularly vulnerable to irrigation season shortages caused by smaller snowpacks and earlier snowmelt in the future.

2.5.2 Surface Water Quality

The founding of Taos Ski Valley in the late 1950's encouraged development in the upper reaches of the Rio Hondo watershed, where there had previously only been an abandoned mining camp (TSV, 2012). The expansion of

the village and a sewage treatment plant built in 1967 increased nutrient loading on the Rio Hondo, particularly phosphorus and fecal coliform. That and other human impacts caused an outcry by farmers downstream (Rodriguez, 1987). To address these concerns, the NM Environmental Improvement Division defined a point-source waste-load allocation for the treatment plant discharge of phosphorus, which was considered the limiting nutrient (NMEID, 1981). This prompted the construction of a new sewage treatment plant in 1983 that greatly improved water quality in the river below the ski valley. A comprehensive and insightful history of the battle between TSV and downstream water users over water quality is given by Rodriguez (1987) and so will not be presented here.

Since this period though, the river has been in compliance with the state regulations for phosphorus discharge. To accommodate potential future development upstream, the NM Surface Water Quality Bureau (NMSWQB) recently crafted a new Total Maximum Daily Load (TMDL) requirement for the river, including both phosphorus and nitrogen (NMSWQB, 2005). These regulations focus on the TSV treatment plant as it is the largest known point source in the area. However, there are other possible non-point sources of nutrient loading from surface runoff and septic tanks in both the upstream and downstream sections of the river.

Despite the potential for agricultural runoff and decentralized septic system discharge, high levels of nutrient loading have not been observed in the lower Rio Hondo. However, this section from the mountain front to the Rio Grande is of concern due to high temperatures possibly caused by low flows and depletion of bank shade trees. For this reason, Rio Hondo was included as one of the tributaries targeted by TMDL regulations for temperature in the upper Rio

Grande basin (NMSWQB, 2004a). Beyond the SWQB's concentrated sampling efforts in 2000 (NMSWQB, 2004b), prior to the drafting of the latest TMDL regulations, there have been no consistent water quality monitoring efforts on the Rio Hondo.

2.5.3 Groundwater Resources

Taos Ski Valley resort and the surrounding village are supplied by a high-elevation, high-volume groundwater spring. Below the resort, hotels and private residences rely on groundwater wells. While no official records exist for these private wells, based on their location and anecdotal evidence they seem to be drilled into alluvial sediments deposited in the river valley. Below the mountain front, downstream users are dependent on the aquifer units described in Section 2.4.3. Near the mountain front, homeowners utilize both wells in the shallow alluvial aquifer and deeper wells in fractured bedrock (Rawling, 2005). Shallow wells on the mesa south of Rio Hondo tap the alluvial aquifer until is cut off at the Airport Fault. Beyond this area, wells tap the deep volcanic-alluvial aquifer. In the river valley itself, wells generally draw from the shallow alluvial aquifer at the river valley bottom (Johnson et al., 2009). North of the Rio Hondo, beginning near the Gates of Valdez, wells utilize fracture zones in the Cerro Negro dacite flow (Johnson et al., 2009; Rawling, 2005).

CHAPTER 3

ISOTOPIC AND MAJOR ION CHEMISTRY CHARACTERIZATION OF THE RIO HONDO WATERSHED

Since the Sangre de Cristo Mountains near Rio Hondo consist of crystalline bedrock with low primary permeability, it is typically assumed that recharge contributions from the mountain block to the basin aquifer are negligible. A water budget for Taos County assumes that only 1.3% of the total precipitation in the mountain block becomes mountain front recharge, a figure which includes potential infiltration from streams along the mountain front as well as subsurface flow from the mountain block (Barroll et al., 2006). However, other studies estimate that a greater percentage of precipitation in the Sangre de Cristos becomes mountain front recharge, anywhere from 3 - 6% (Anderholm, 2001) to 16% (McAda and Wasiolek, 1988). Manning (2011) actually estimates that at least 20 - 50% of recharge to the Española basin aquifer can be attributed solely to deep mountain block groundwater flow. These estimates seem more appropriate if the widespread fractures and faults in the region actually make the bedrock in the Sangre de Cristos a significant contributor to basin groundwater as suggested in Ludington et al. (2004).

To begin to quantify the influence of mountain block recharge, we first must determine if mountain block groundwater has a unique geochemical composition. If so, we can potentially trace this signature and determine its influence on other water samples in our study area, such as groundwater in the basin

aquifer. Therefore, the first step is to characterize the isotopic and major ion composition of surface and groundwater samples in the upstream mountain block and the downstream basin. In hydrology, the stable isotope ratios of oxygen ($^{18}O/^{16}O$ or δ^{18}O) and hydrogen (^{2}H/^{1}H or δ^{2}H) in water function as natural tracers. Different water sources, or end members, in a watershed can carry different isotopic signatures, making them easily identifiable (Sklash et al., 1986). Similarly, the major ion composition of water can help identify chemically unique end members (Pinder and Jones, 1969; Bricker and Jones, 1995; Frisbee et al., 2011). If two or more distinct end members exist, mixing models can be used to determine how much each source contributes to a particular water sample of interest (Sklash et al., 1986; Hooper and Shoemaker, 1986). Major ion composition can also provide additional information about groundwater flow paths since major ion concentrations (especially Ca^{2+}, Na^{+}, and K^{+}) can evolve as water flows through different geologic formations and can increase the longer the water is in contact with rock. For instance, Frisbee et al. (2011) found that when a river is influenced by old, deep groundwater flowpaths that have acquired major ions over a longer period of time, major ion concentrations in surface-water show a linear increase with drainage area. We can therefore use our basic isotope and major ion results to make general observations about the degree to which mountain block recharge affects surface and groundwater at the mountain front and into the basin.

3.1 Factors Influencing Isotopic Composition

The groundwater and surface-water in the mountain block and mountain front area is likely derived solely from meteoric input, as previous literature has not suggested connate or hydrothermal water present in this region. There are

some warm springs that discharge from the east wall of the Rio Grande Gorge but these are thought to be associated with the Airport Fault rather than geothermal activity in the mountain block (Johnson et al., 2009). Variations in precipitation can actually produce several isotopically or chemically-unique endmembers. Precipitation can vary isotopically for several reasons. Most atmospheric water vapor originates from evaporation over the ocean and so begins with the same general isotopic composition, with some variation due to latitude. However, as the water vapor moves inland, its isotopic composition changes depending on the fraction of moisture remaining in the cloud or airmass. Heavier isotopes rain out preferentially, so precipitation becomes increasingly lighter with distance inland. This is called the distance or continentality effect (Sharp, 2007). Thus, the source of seasonal precipitation (Gulf of Mexico vs. Pacific Ocean, for instance) determines the degree of isotopic depletion it undergoes before raining out in New Mexico. A study in the San Juan Mountains of southern Colorado even found significant differences between early winter precipitation and late winter precipitation, due to different sources for winter storms (Frisbee, 2010). Orographic effects can influence the isotopic composition of precipitation in much the same way. As elevation increases, more precipitation rains out, preferentially removing heavier isotopes. This makes the precipitation at the top of a mountain lighter than the precipitation at the base. The Rio Hondo watershed covers an elevation range of greater than 2000 m, so orographic effects could feasibly influence isotopic variation.

The isotopic composition of precipitation is also influenced by seasons. Especially in semiarid climates like New Mexico, the air is dry enough in summer that a significant amount of evaporation can occur between the cloud and the

ground. Evaporation causes the precipitation to preferentially lose lighter isotopes, leaving the precipitation that actually reaches the ground heavier. Other factors can have even more pronounced effects. Temperature affects the amount of fractionation between water vapor in an air mass and the resultant precipitation so that warmer climates have less depleted precipitation and colder climates more depleted (Sharp, 2007). Isotopic composition can also change after precipitation hits the ground. As discussed in Nimz (1998), the metamorphosis of snow through sublimation and other processes makes residual snow heavier than fresh snow. This transformation, described as the Snow Evolution Line in Frisbee (2010), is important when considering groundwater recharge since snowmelt from this residual snow can comprise 40 - 60% of groundwater recharge in New Mexico (Earman, 2004). As water recharges through soil and the shallow subsurface, it can change isotopically due to evaporation (Barnes and Allison, 1988). However, once water has moved beyond the shallow subsurface and become deep percolation to deeper portions of the vadose zone, evaporation is minimal so the water should no longer undergo kinetic fractionation.

Other processes in the subsurface, however, may affect isotope ratios further. For instance, water flowing through a geothermal system can be affected by "^{18}O shift" (Craig, 1963). This is caused by high temperature interaction with high ^{18}O rocks that can increase ^{18}O in water dramatically. Since this rock typically contains little to no hydrogen, ^{2}H remains unchanged. In the Sangre de Cristos near Rio Hondo, however, where there is no evidence of geothermal activity in the mountain block, we do not expect to see any ^{18}O shift. Instead, the groundwater should preserve the isotopic signature from its recharge. The only changes expected are from mixing with water from other recharge sources. Thus, measuring stable-isotope ratios is an important tool for determining how much

water the mountain block contributes to the basin. By defining end members that have preserved the isotopic signature of a certain location or season of recharge, we should be able to determine what mixing ratio of which end members controls the isotopic composition of our water samples.

3.2 Factors Influencing Major Ion Composition

Major ion composition generally refers to the concentrations of Ca^{2+}, Mg^{2+}, Na^{+}, K^{+}, HCO_3^{-}, CO_3^{2-}, Cl^{-}, and SO_4^{2-}, the most significant components of salinity in water. The concentrations of these major ions in precipitation tend to be dilute but can be heavily influenced by certain environmental factors. For instance, sea spray produces higher Na^{+} and Cl^{-} concentrations in precipitation near the coast. Aerosol soil and dust particles increase the amounts of Ca^{2+}, Mg^{2+}, and K^{+} further inland (Warneck, 1987). Especially in a semiarid desert environment like New Mexico, calcium carbonate ($CaCO_3$) and gypsum ($CaSO_4$) dust can increase Ca^{2+} and SO_4^{2-}. Another source of SO_4^{2-} is the oxidation of natural dimethyl sulfide and SO_2. This means that sulfate concentrations are higher near volcanoes and also in areas with high fossil fuel combustion such as urban areas or coal-fired power plants. Since prevailing winds in this region travel from west to east, emissions from coal-fired power plants in the Four Corners area of northwestern New Mexico could potentially increase SO_4^{2-} in Rio Hondo precipitation. Concentrations of major ions are often inversely linked to the amount of rain in an area and so can also change seasonally (Warneck, 1987).

Like the isotopic composition, the major ion composition of precipitation can evolve as it travels through the soil and shallow subsurface, due to evaporation, dissolution of soil components, chemical precipitation, ion exchange, or

other processes. However, unlike the isotopic composition, which presumably remains unchanged once it becomes deep percolation, the major ion composition continues to change as it moves deeper (Lasaga, 1984). In fact, anthropogenic and natural processes can both significantly alter the concentrations of major ions in groundwater. The dissolution of rock along groundwater flowpaths often accounts for the largest variations in major ion composition (Drever, 1997; Bricker and Jones, 1995). Different geologic formations contribute ions depending on their mineralogy. Just as flow through halite would likely contribute Na^+ and Cl^-, gypsum ($CaSO_4$) would increase Ca^{2+} and SO_4^{2-} concentrations (Drever, 1997). Even if a geologic formation does contain a particular element, dissolution rates due to mineralogic structure can control how much of the element actually dissolves into the water. Both aragonite and calcite (different forms of $CaCO_3$) have the potential to release Ca^{2+}, but the calcium ion is bonded more weakly in the structure of aragonite, making it more prone to dissolution (Railsback, 2007). The Goldich weathering series (Goldich, 1938) ranks igneous silicate rocks in order of their susceptability to weathering, making it possible to estimate their likelihood of contributing their constituent ions to groundwater. The concentrations of major ions resulting from dissolution of matrix material can be further influenced by chemical reactions and even biological effects. However, the largest control is still generally the type of rock the water flows through and the amount of time it is in contact with that rock (Lasaga, 1984). The other major contributor is anthropogenic input, which can be significant for certain major ions. As an example, salt from road de-icing can greatly increase Na^+ and Cl^- concentrations. Similar trends in these two constitutents can also be caused by the evaporative signature of irrigation recharge.

Because the major ion composition of a water sample is determined by its source and its flowpath, these measurements are potentially more useful than stable isotopes for determining the influence of old, deep groundwater flowpaths. Major ion compositon can determine the mixture of sources for our samples by identifying unique end members (Pinder and Jones, 1969), but also the flowpath along which that water likely traveled. The concentrations of certain major ions, like Na^+ and Cl^-, should also make it easier to spot areas that are subject to anthropogenic inputs.

3.3 Methods

Water samples, including precipitation, surface-water, groundwater and springs in both the upstream mountain block and the downstream basin, were collected on a seasonal basis during the period July 2010 to Nov 2011 [Figure 3.1]. Precipitation samples were collected with bulk collectors placed in the watershed at 6 locations, providing an elevation profile from the lower irrigation valley at Arroyo Hondo to the top of the Taos Ski Valley ridge. Each bulk precipitation collector consisted of a 1.8-m-long, 10.2-cm-diameter PVC pipe, open at the top and sealed at the bottom. This was staked in place perpendicular to the ground surface and mineral oil was added to the bottom of the collector. When snow fell into the collector, it sunk below the mineral oil so that the oil served as a barrier against evaporation and prevented isotopic alteration of the collected precipitation. This design was based on the precipitation collectors used by Earman (2004) and Frisbee (2010).

Grab samples of surface-water were collected seasonally at 6 points along the Rio Hondo, two below the mountain front (SWRHL) and 4 above (SWRHH).

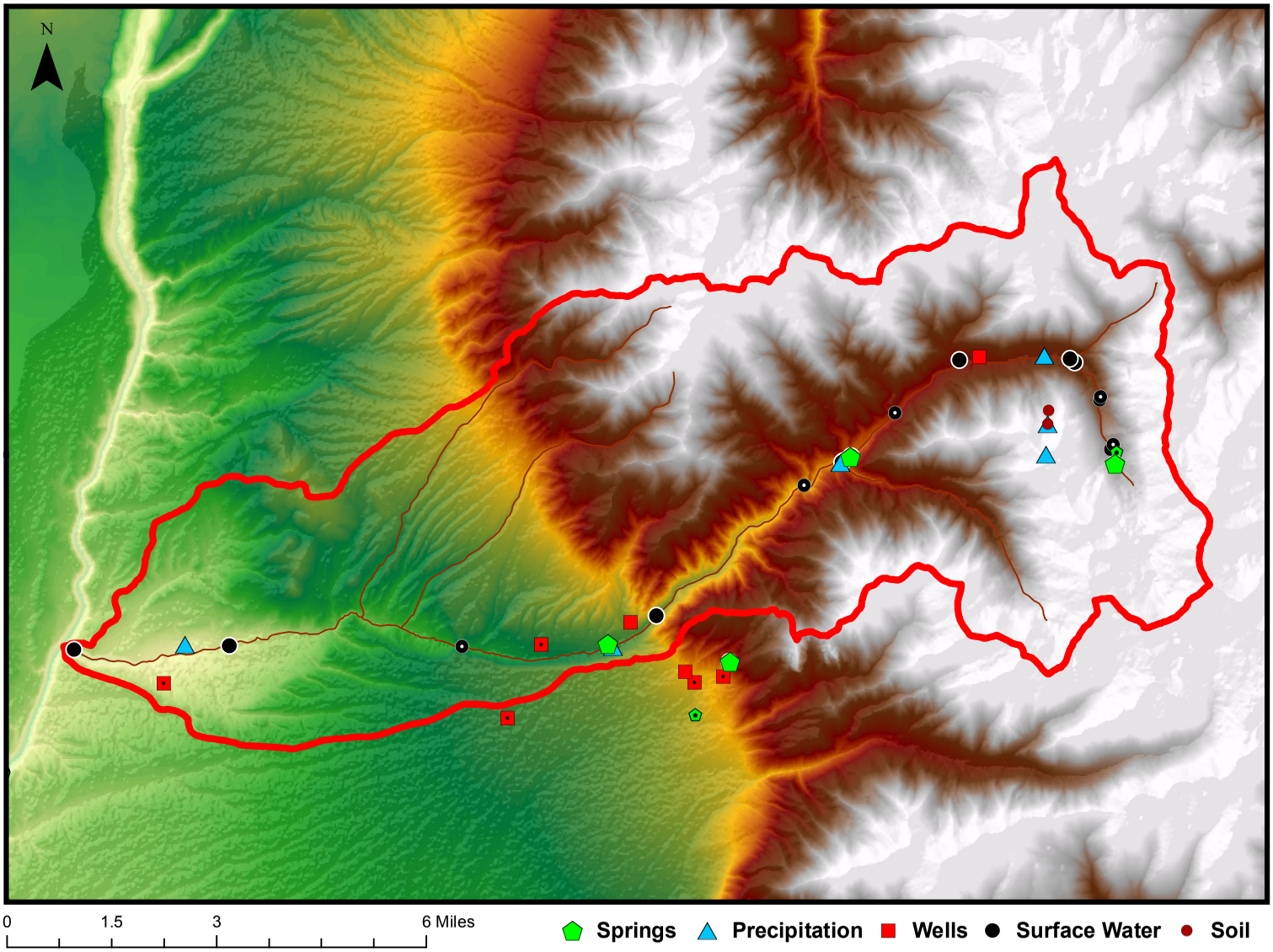

Figure 3.1: Locations of water samples taken in Rio Hondo region. Samples that are marked with a dot were only sampled two times or fewer.

Samples were also collected from the two largest tributaries (SWT), South Fork and East Fork, near their confluence with the Rio Hondo. Other samples along the Rio Hondo and its tributaries were only taken twice or less due to logistical difficulties. While they cannot provide a seasonal signature, the results are presented along with the regular samples to provide further characterization.

Mountain groundwater is defined as groundwater within the mountain block. Acknowledging that spring water often differs greatly from well water, we took samples at both wells and springs for the sake of comparison. Mountain springs (GWMS) are represented by grab samples taken at the high-elevation (3151 m) spring that supplies Taos Ski Valley and a low elevation (2565 m) soil seep further down the mountain. Seasonal grab samples from a domestic well in the river valley just below Taos Ski Valley (2766 m) represented mountain well water (GWMW). Two more samples were taken at domestic wells further down the mountain but could only be sampled once due to access issues. These results were used for comparison and reported in the appropriate season.

Groundwater at the mountain front is represented by grab samples from two deep wells (GWMFW) as well as a perennial spring (GWMFS) and roof seepage in a mountain-front cave (GWMFC). A few additional wells were only sampled once due to logistical difficulties but their results are presented where appropriate. Because the construction details for the wells were unknown, the well bore capacity could not be computed. Therefore, before taking well water samples, the well bore was purged until pH, temperature and conductivity, as measured on a handheld meter, had stabilized, as per Wood (1981).

The infiltration of residual snowmelt through the soil is likely an important contributor to groundwater recharge. To characterize soil water, bulk soil

samples (MS) were collected during snowmelt at 3 sites on the slope of Taos Ski Valley. A clean auger was used to collect an $\sim$ 0.46 m deep core which was then stored in a clean plastic Ziploc bag. Soil samples underwent vacuum distillation to remove soil water for isotope analysis following the procedure described in Araguás-Araguás et al. (1995). Samples of snowmelt runoff (RO) were taken near the soil samples. Grab samples of residual snow (OldS) in Taos Ski Valley were made in March, April, and June to quantify the isotopic evolution of snow.

During field sampling, values for field pH, temperature, conductivity, and total dissolved solids (TDS) were measured with an Oakton pH/CON 300 hand-held meter and recorded for all samples except precipitation, residual snow, and soils. For isotopes and general chemistry analysis, samples were collected in 500 ml polyethylene bottles and stored in a cooler until they could be transported to the laboratory. Samples for cations were filtered through 0.2 μm membrane filters. Nitric acid was added to achieve pH $<$2.0. These bottles were then also stored in a cooler until they could be transported to the laboratory.

3.4 Analytical Methods

All water samples were analyzed for δ^2H and δ^{18}O on a Picarro Cavity Ring Down Spectroscopy (CRDS) unit. Instead of using isotope mass differences as do traditional mass spectrometers, CRDS takes advantage of the unique near-infrared absorption spectra of isotopes. A laser beam reflected around a cavity is diminished or "rings down" at a rate dependent on the mixture of O and H isotopes in a sample of water vapor, allowing characterization of $\delta^2 H$ and $\delta^{18} O$ simultaneously (Picarro, 2012). No sample preparation is required since the unit automatically converts liquid water samples to water vapor for analysis.

Cations, anions, and alkalinity were analyzed by the Geochemistry Laboratory at the University of New Mexico Earth and Planetary Sciences Department. Alkalinity as HCO_3 was determined in the laboratory by titration. Major anion composition of water samples was determined by Ion Chromatography (IC) and cation composition by Inductively Coupled Plasma (ICP) Emission Spectrometry.

Precipitation samples, soil water samples, and residual snow and snowmelt samples were not analyzed for major ion composition. For precipitation, regional averages from the three nearest National Atmospheric Deposition Program (NADP) stations were used to characterize major ion composition [locations in Appendix C]. The USGS Snowpack Chemistry Monitoring project results for a site at Taos Ski Valley also provided major ion composition for bulk winter precipitation.

3.5 Results and Discussion

Isotopic composition can be used to separate Rio Hondo precipitation into three isotopically unique end members by season [Figure 3.2]. The most drastic differences are between the significantly lighter winter precipitation and heavier summer precipitation. Since fractionation between water vapor in an air mass and the resultant precipitation is dependent on temperature, this difference is likely due to seasonal temperature effects, which would lead to depleted precipitation in the colder winter temperatures. Any depletion effects from the removal of water from a winter air mass would also be more pronounced in colder temperatures. Another factor could be the source of seasonal precipitation. If summer precipitation originates from a closer source, this would reduce the level of

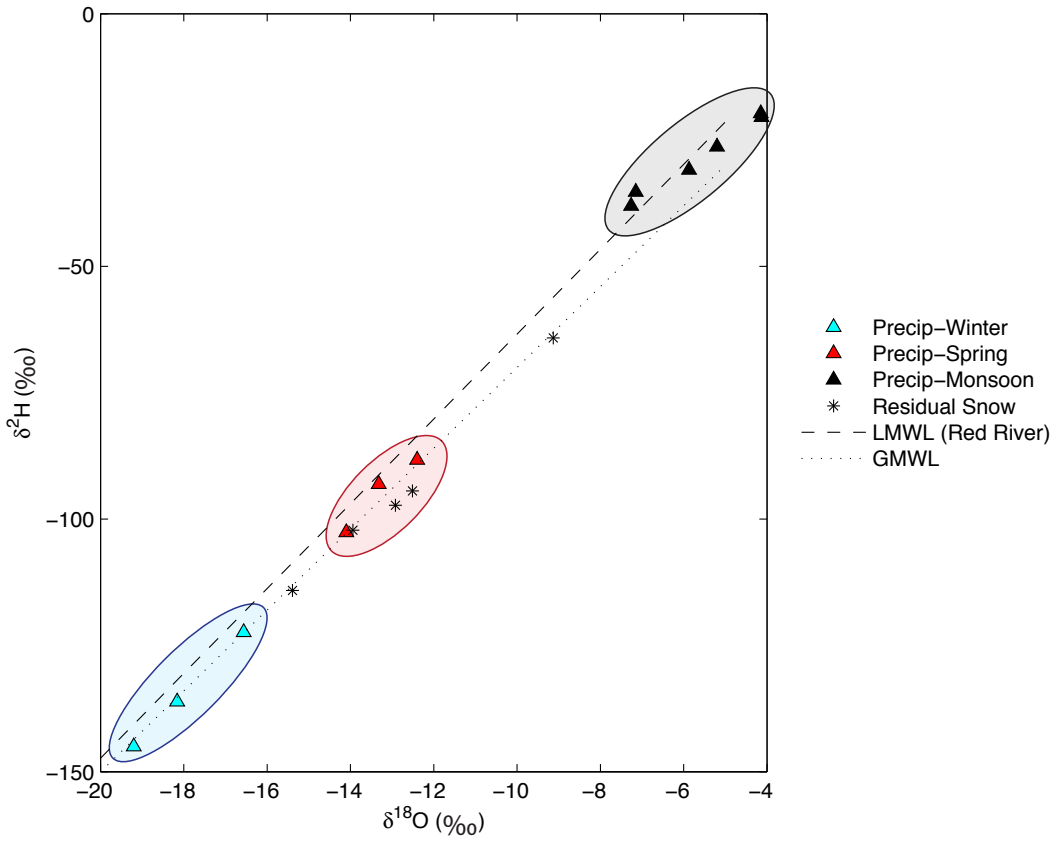

Figure 3.2: Seasonal variation in isotopic composition. The Local Meteoric Water Line (LMWL) is plotted according to data collected in the neighboring Red River watershed (Campbell et al., 2008).

depletion during travel and make it is heavier. Another possibility in a semiarid climate like New Mexico is that summer precipitation could undergo more extensive evaporation than winter snow during precipitation events. This would also result in heavier summer precipitation and lighter winter precipitation, though the effect would likely be small. While monsoon season and winter precipitation provide two very distinct end members, separating a spring precipitation end member is complicated because it overlaps with residual snow. Similar to the results of Earman et al. (2006) and Frisbee (2010) in southern Arizona and southern Colorado respectively, residual snow evolves isotopically towards spring precipitation, making it difficult to separate these two sources using only isotopes.

With such a large range in elevation across the Rio Hondo watershed, an orographic effect should be detectable in precipitation isotopic composition. A typical elevation trend, based on worldwide measurements, is a -0.26 ‰ δ^{18}O decline per 100 m of elevation (Poage and Chamberlain, 2001). However, only the monsoon season seems to show this orographic effect [Figure 3.3]. As compared to winter storms, monsoon storms show stronger convection patterns which could explain this significant orographic trend.

Besides precipitation, it is difficult to identify other water types based solely on isotopic composition [Figure 3.4]. Surface water and groundwater in the mountain block, as well as mountain front springs, are clustered near the center of a local water line and largely indistinguishable from spring precipitation and each other. However, some unique isotopic signatures do appear. Soil water plots to the right of the water line and can be traced along a line of slope 5.5 back to average winter precipitation. This slope falls between the slope of water evaporated at the surface (4 - 6) and water evaporated in the subsurface (2 - 5) (Barnes and

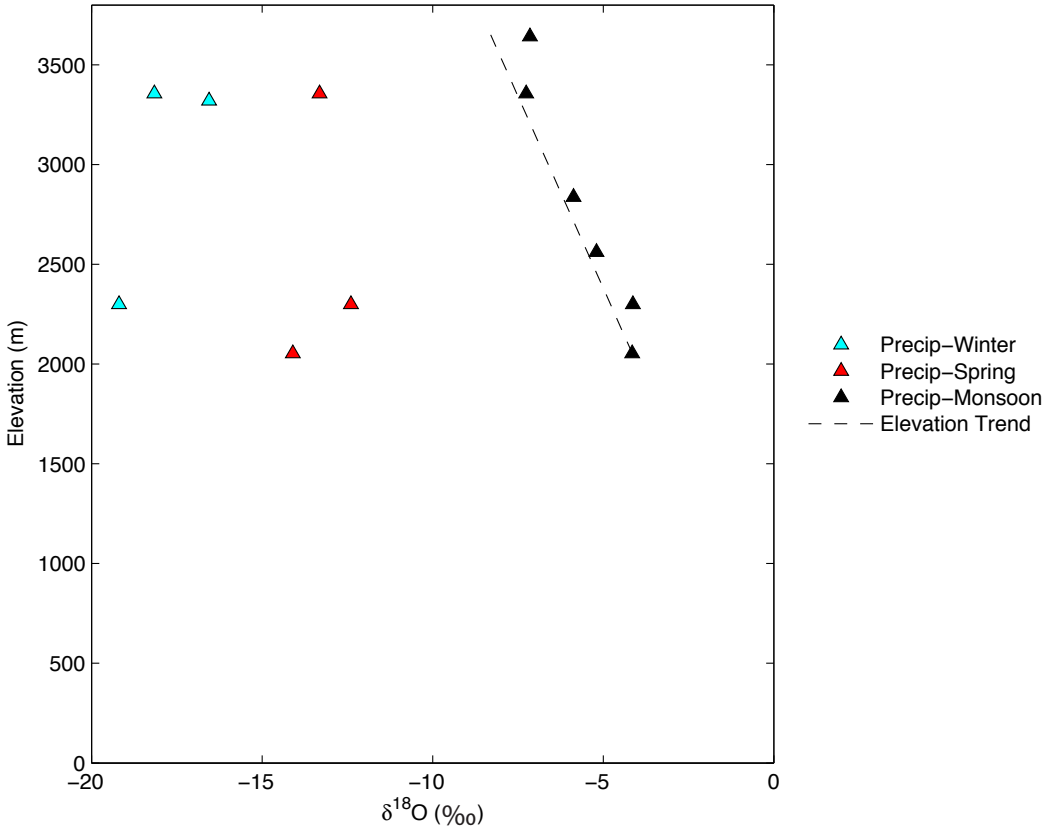

Figure 3.3: Orographic effect on seasonal precipitation. The dashed line indicates the expected orographic effect (-0.26‰/100 m) documented by Poage and Chamberlain (2001).

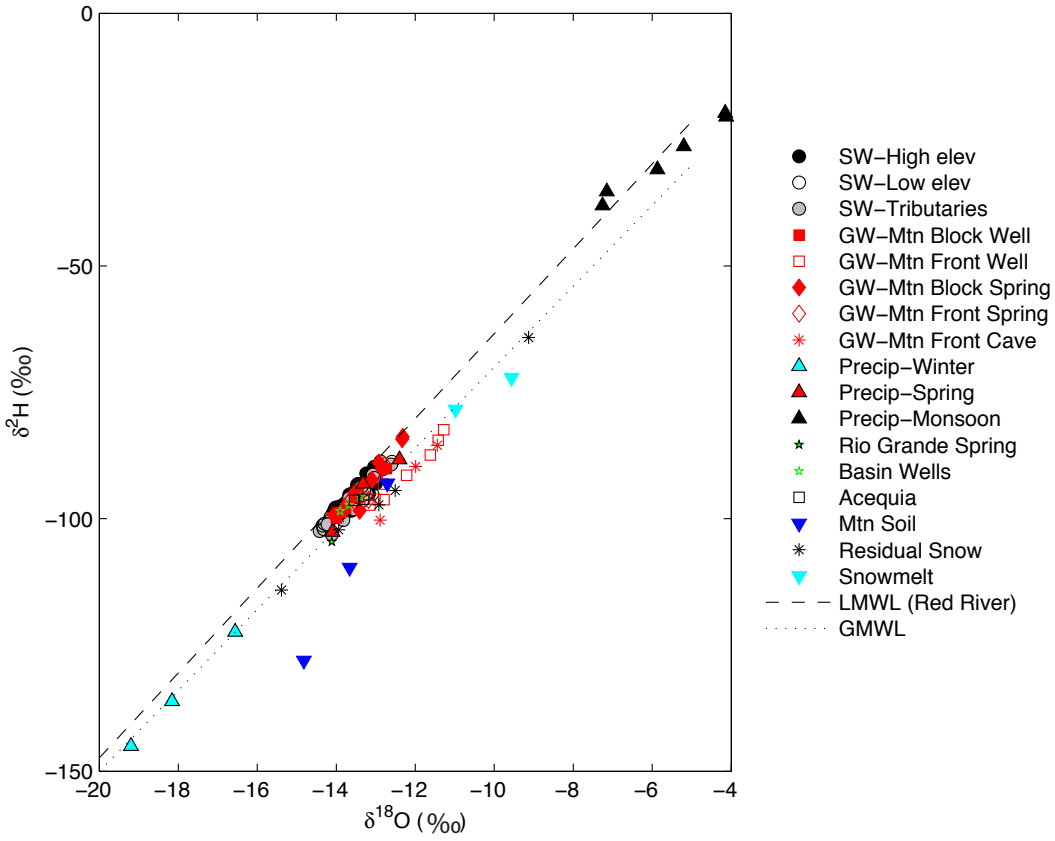

Figure 3.4: Isotopic composition of all water samples. The Local Meteoric Water Line (LMWL) is plotted according to data collected in the neighboring Red River watershed (Campbell et al., 2008).

Allison, 1988). This indicates that the soil water likely originated from infiltrating snowmelt that has already evolved isotopically at the surface. Deep mountain-front groundwater wells are also offset to the right of, and nearly parallel to, the local water line. Given the consistency of the offset and low-to-nonexistent slope from the central cluster of precipitation, surface-water, and groundwater, the water from these deep wells seems unlikely to originate simply from evaporation of these waters. Rather, since these offset samples plot in line with the residual snow and snowmelt runoff samples, these deep mountain-front wells may be supplied by variably metamorphosed high-altitude snow. If so, this does support the idea of deep flowpaths through the mountain block. Another possible explanation is that this water may have undergone an ^{18}O shift as discussed in Section 3.1. However, this is unlikely, as there is no documented geothermal activity in this area and the shift is too small and consistent across seasons and samples.

As with isotopic composition, water types can be further differentiated by their major ion concentrations [Figure 3.5]. Regardless of season, precipitation is largely dominated by Ca^{2+} and SO_4^{2-}, likely sourced from the gypsum and calcite common in atmospheric dust over New Mexico. The water in the watershed follows a straightforward evolution from this calcium-sulfate type precipitation to calcium-bicarbonate type water as it travels downstream. The exceptions to this evolution trend are deep wells along the mountain front that contain calcium-sulfate water similar to precipitation even though they are located at a lower elevation than calcium-bicarbonate type surface and groundwater samples. Proportional enrichment of SO_4^{2-} could appear artificially high due to the removal of Ca^{2+} by chemical precipitation. However, absolute concentrations of Ca^{2+} in the wells do not decrease, indicating that the SO_4^{2-} enrichment is real. One mechanism for SO_4^{2-} enrichment is the oxidation of pyrite assoicated with quartzite

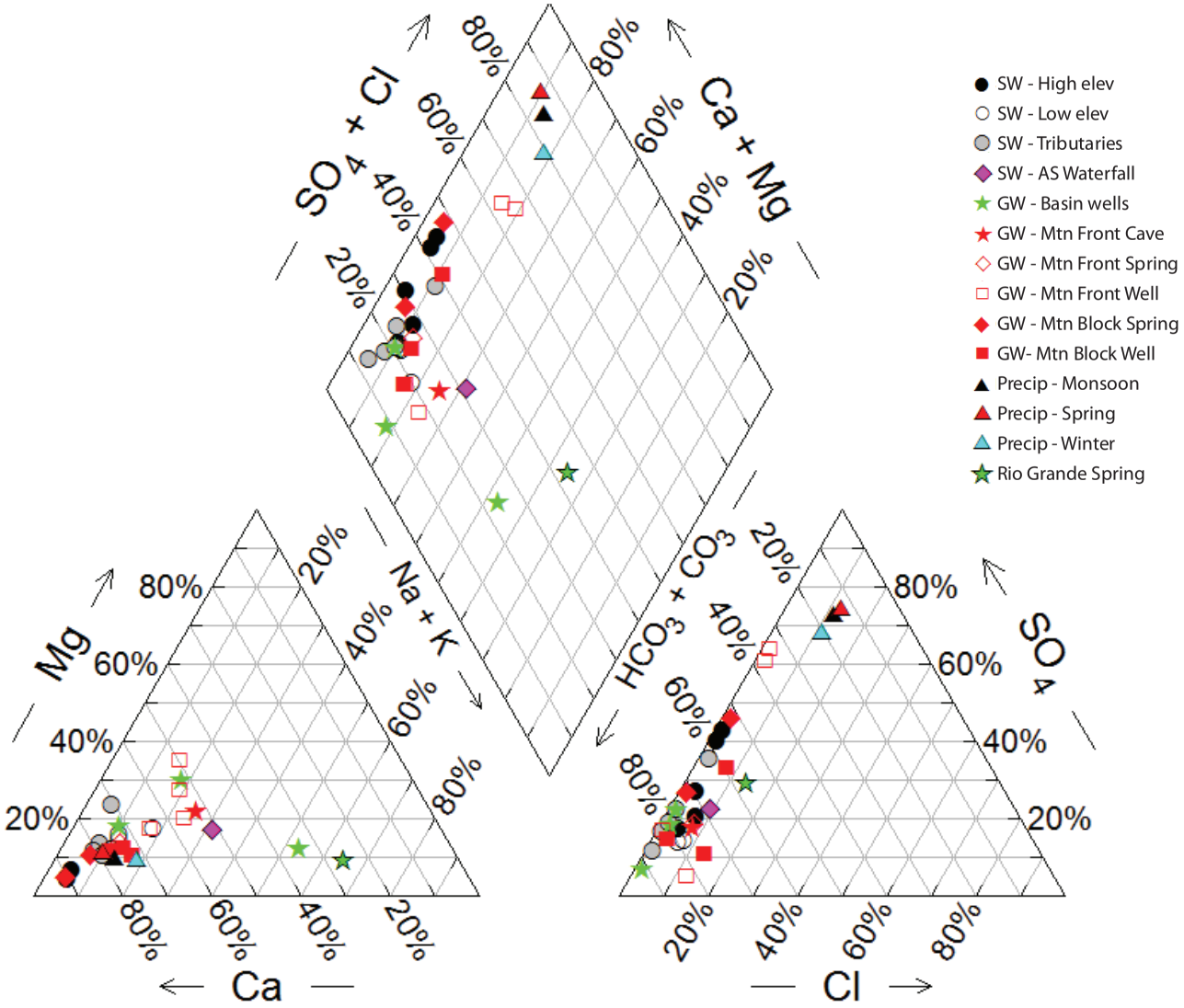

Figure 3.5: Major ion composition of all water samples.

veins, a possibility since quartzite is present in the mountain block (Rawling, 2005). The concentration of Mg^{2+} is also higher in these wells than in other water samples. Mg^{2+} enrichment can be caused by the weathering of mafic rocks, present in the mountain block as well. If the enrichment of both SO_4^{2-} and Mg^{2+} is attributed to bedrock weathering, this implies the existence of deeper flowpaths through the mountain block that discharge to the basin aquifer.

As shown in Figure 3.5, these mountain-front groundwater wells plot between calcium-sulfate meteoric input and a calcium-bicarbonate type water, indicating mixing of these components. Identifying the non-meteoric component, however, is difficult since most of the water samples have a similar composition, including surface-water from the Rio Hondo and its tributaries as well as groundwater in both the mountain and basin. Of the calcium-bicarbonate type waters, the two most like the deep mountain-front wells are mountain springs followed by high elevation (above the mountain front) surface-water. Low elevation (below the mountain front) surface-water and mountain-front spring water plot further from mountain front wells. Since deep mountain-front groundwater wells are most similar to mountain groundwater, this suggests some connectivity between groundwater within the mountain block and groundwater in the basin aquifers.

Another hydrochemical facies, a sodium-bicarbonate type water, was identified in both an Arroyo Hondo well near the confluence with the Rio Grande major and a spring that discharges on the east side of the Rio Grande Gorge. The well is located in an area east of Airport Fault characterized by intermixed Servilleta basalt and gravel. At the fault, water in this formation is thought to be funneled down, providing water to the springs discharging in the gorge to

the west (Johnson et al., 2009). Thus, these results seem consistent with previous hydrogeology work in this area.

Since the concentrations of major ions in water are influenced by the amount of time it is in contact with a contributing rock type, major ion composition can roughly indicate the existence of and degree of influence from long, deep flow paths. In Rio Hondo surface-water samples, major ion concentrations, with the exception of Cl^- and SO_4^{2-}, are directly related to the contributing drainage area [Figure 3.6]. Frisbee (2010) proposes that this kind of geochemical enrichment with increasing scale is caused by rock-water interactions along long residence-time flowpaths and that it should not be evident in streams dominated by surface and shallow subsurface flowpaths. Thus, the trend in our data might indicate the existence of some deeper flowpaths discharging to the Rio Hondo as it moves farther into the basin.

One concern with this inference is that the largest increases in major ion concentrations occur beyond the mountain front (see unshaded areas in Figure 3.6), potentially indicating that this trend is merely an anthropogenic effect. However, when these basin samples are removed, concentrations still increase slightly with drainage area within the mountain block. Na^+ and Cl^- are the most likely to be influenced by anthropogenic effects. Both do show a spike in concentration during irrigation season (July 2010 and Sept 2010 samples), which could indicate some evaporation signature caused by flood irrigation. However, this evaporation is not visible in the stable isotope results for these samples. Also, even during months when irrigation should not be a factor, the concentration increase with area continues, albeit in a diminished fashion. Therefore, the underlying enrichment trend is retained, independent of anthropogenic influence.

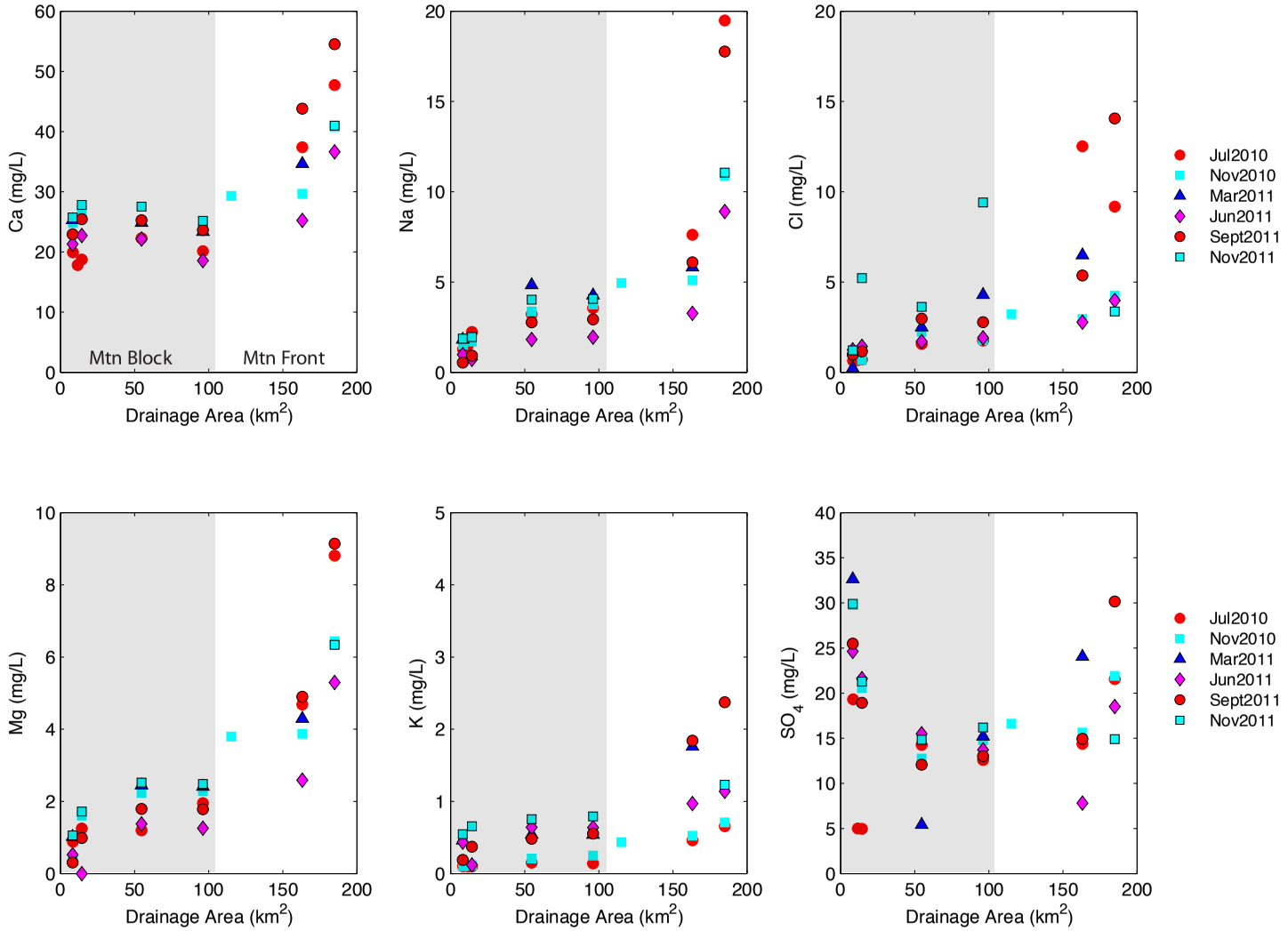

Figure 3.6: Evolution of major ion concentrations as a function of drainage area. Note: Major ions are plotted at different scales appropriate for their concentrations. The gray area indicates samples taken within the mountain block and the white area indicates samples taken beyond the mountain front in the basin.

The behavior of silica (SiO_2) can also indicate the existence of longer flow paths. Concentrations of silica are unlikely to be influenced by anthropogenic factors since they are largely controlled by rock-water interactions (i.e., the type of rock with which water comes in contact) and the residence time of the water in contact with the rock. Silica is less susceptible to change than other major ions in natural water since factors such as salinity, pH, climate, and temperature have little to no measurable effect on silica concentrations (Davis, 1964). Some types of vegetation and especially diatoms, a type of phytoplankton, can remove silica from streamwater. These processes can result in silica sequestration if the recycling of silica from dead organisms does not match the rate of uptake, a situation common in lakes (Street-Perrott and Barker, 2008). This usually results in a temporary net loss or reduction of silica concentration in streamflow. However, since silica shows enrichment, rather than reduction, with increasing drainage area [Figure 3.7], it seems silica behavior in the Rio Hondo is dependent on processes other than this biological influence. As with the major ion behavior, this silica enrichment trend suggests the possible influence of deep flow-paths that undergo more rock-water interaction, leading to a higher silica content. Kennedy (1971) did observe that silica concentrations can increase during periods of high discharge and attributed this to a greater contribution from subsurface soil flow. However, given that our enrichment trend is consistent across seasons and thus a range of discharge levels, our silica results also appear to be independent of a bias from soil contributions.

Chloride/bromide ratios have also been used as a first test for determining anthropogenic influence on groundwater and surface-water since domestic sewage shows a much higher Cl/Br value than meteoric or natural groundwater (Davis et al., 1998). Based on Cl/Br values, the lower reaches of the Rio Hondo

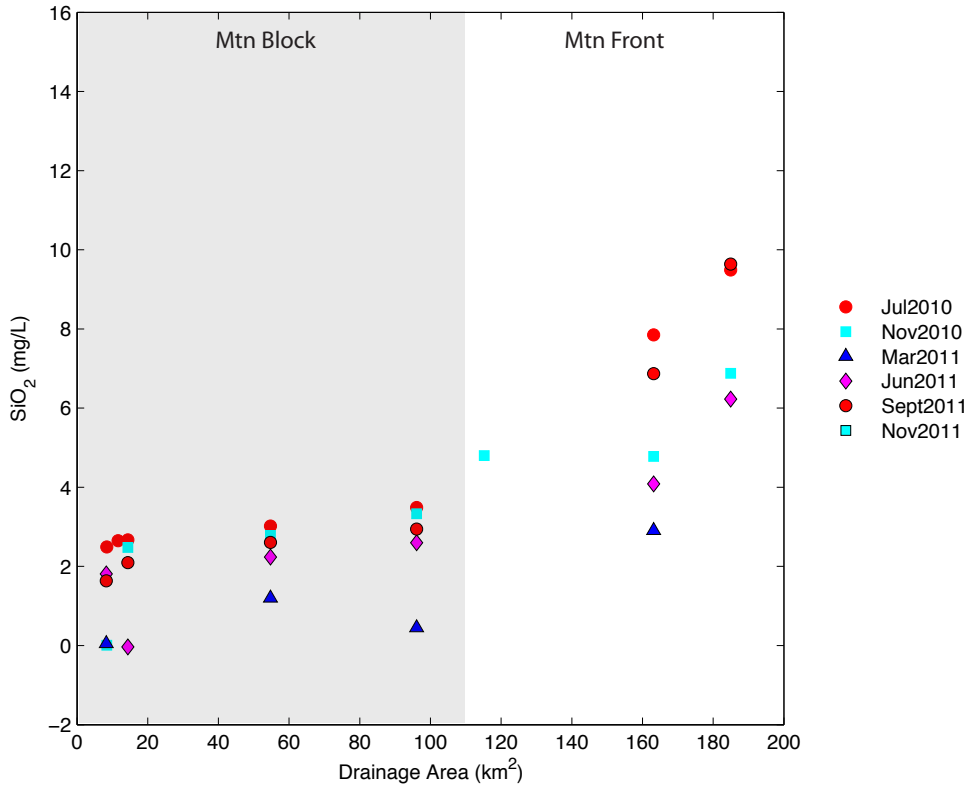

Figure 3.7: Silica concentration evolution as a function of drainage area.

and some domestic wells do potentially show some influence from septic seepage [Figure 3.8]. However, this influence is minimal, with most samples at or below the lowest limit for sewage contamination. Another proxy for anthropogenic influence is nitrate, which can come from agricultural runoff and septic system seepage. Especially for an agriculturally-developed watershed like the Rio Hondo, the nitrate concentrations are very low [Figure 3.9] compared to other heavily-impacted watersheds (e.g., Williams et al. (1998)). This indicates that there is some anthropogenic influence, but it is relatively small considering the amount of domestic and agricultural development in the area. Therefore, we cautiously propose that the observed trends in major ion concentration, and thus our conclusion about the existence of long deep flowpaths, is largely unbiased by human activities.

3.6 Conclusions

This sampling effort has effectively established a baseline for the isotopic and major ion composition of different water types found in this region. This serves as useful starting point for future research and sampling efforts on the Rio Hondo, as well as helping lay a foundation for the proposed hydrogeology model. In particular, the results suggest that a model of the region must be constructed in a manner that accounts for any potential deep mountain block flow. While not able to definitively establish how much influence mountain block recharge exerts on the basin hydrogeology, the results of this sampling effort do suggest that MBR impacts both the basin aquifers and Rio Hondo surface-water. The effect of these deep flow paths appears in deep mountain front wells, which our sampling indicates are a mixture of precipitation and groundwater

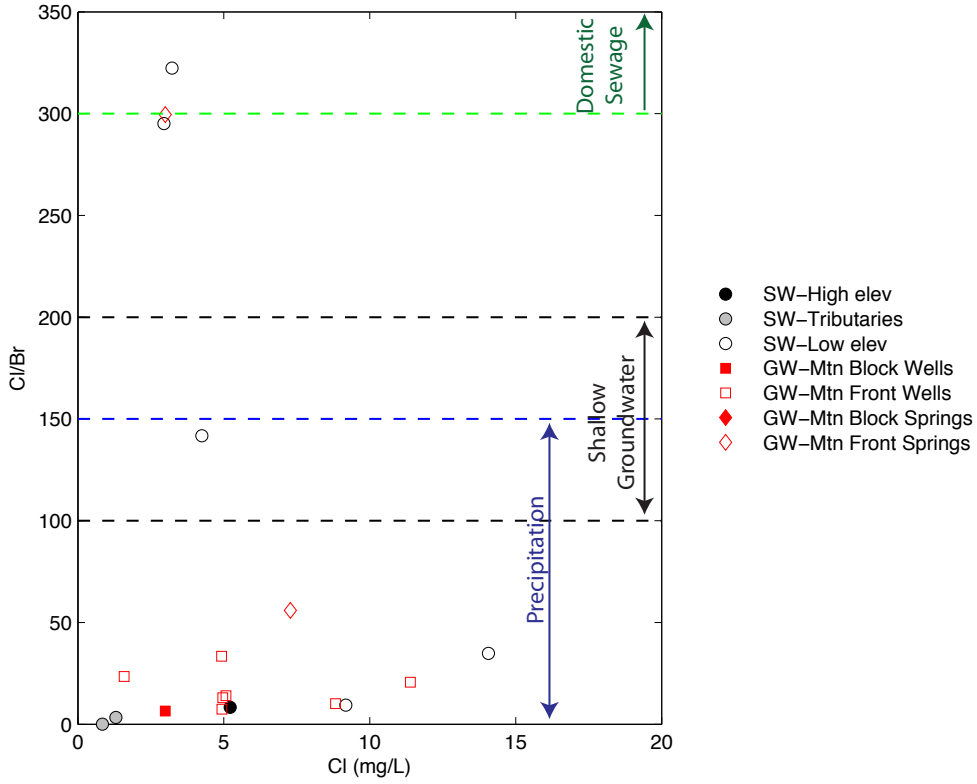

Figure 3.8: Chloride/bromide ratios of water samples. The Cl/Br values shown for precipitation, shallow groundwater, and domestic sewage are from Davis et al. (1998)

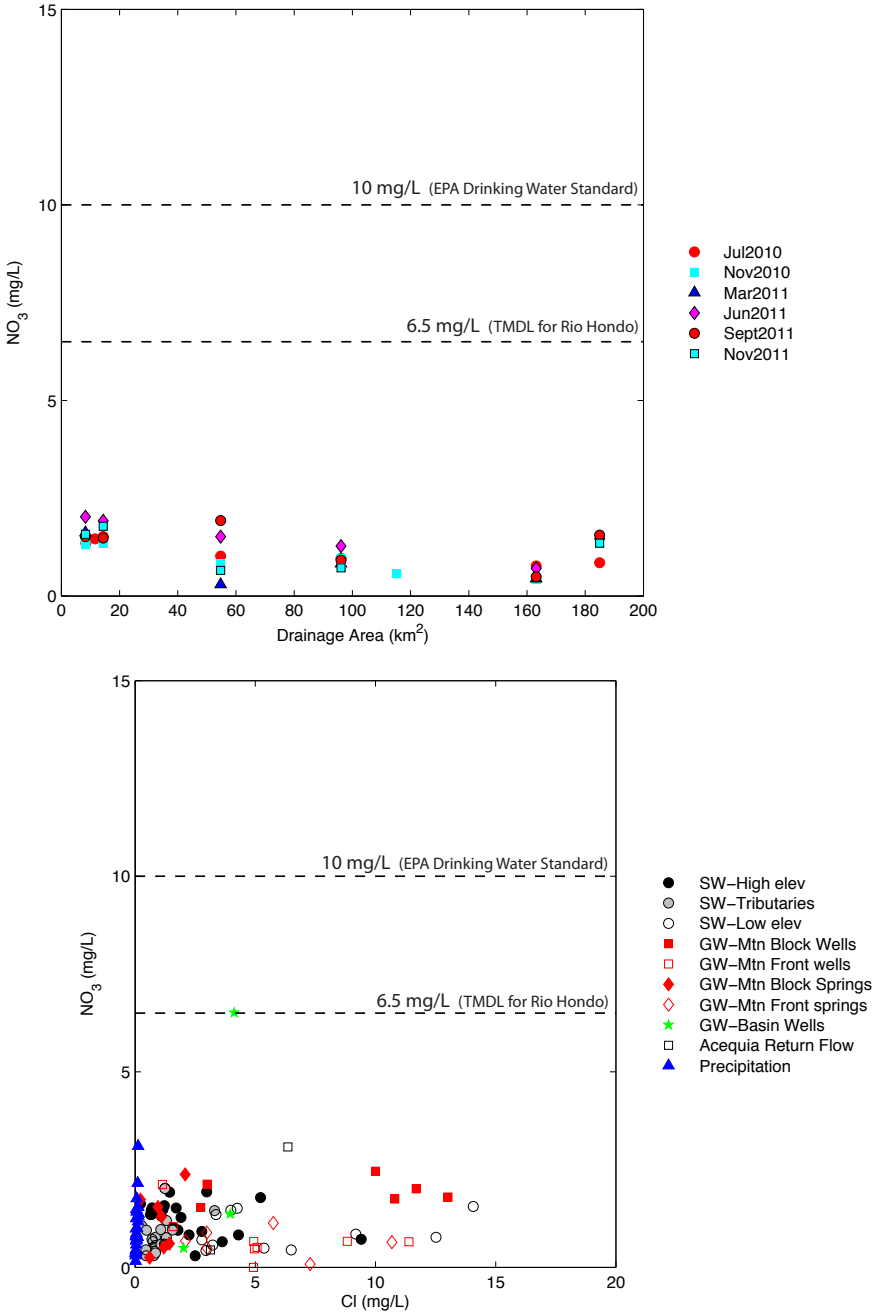

Figure 3.9: Nitrate concentrations as a function of drainage area (top) and of chloride concentration (bottom). The TMDL value is taken from the low-flow regulations. During much of the year, the accepted TMDL value is actually much higher (NMSWQB, 2005).

orginating within the mountain block. The direct relationship between major ion composition in the river and the size of the contributing drainage area also indicates that long, deep flowpaths, like those from deep percolation in the mountain block, may be substantial contributors to the Rio Hondo. The occurence of this enrichment trend in our watershed is actually quite surprising. It is similar, as mentioned earlier, to behavior in the San Juan Mountains documented in Frisbee (2010). However, that study area differs greatly from the Rio Hondo. The San Juans have a largely volcanic geology, making them much more permeable and thus more likely to host deep mountain block flow than the crystalline Sangre de Cristos. In addition, the San Juan enrichment trend was documented in a nearly pristine watershed that covered 1670 km^2 (645 mi^2), whereas the Rio Hondo watershed covers only 194 km^2 (75 mi^2) in an area that is comparatively heavily human-impacted. The trends observed in Frisbee (2010) support a 3D catchment mixing model which incorporates longer regional flow paths, rather than just surface and shallow subsurface flow. If the enrichment in the Rio Hondo is due to the same processes, then this work could provide another case study supporting this conceptual model by showing that deep mountain block groundwater is important not just in permeable volcanics but also in fractured and faulted crystalline geology.

3.7 Future Work

In future work, to better constrain contributions from different water sources, a mixing model could be applied to our samples to determine the relative influence from each of the identified end members. Determining the influence of seasonal precipitation could indicate how climate change would affect Rio Hondo

hydrology if there are changes in snow pack or reduced precipitation. A mixing model could also help determine the degree to which mountain groundwater contributes to the basin aquifer and provide better estimates for future hydrogeology models in this region.

Creating an appropriate mixing model likely requires further sampling efforts since, due to limited sampling, this study may not have identified all the potential end members in the area. The few soil water samples taken do show a distinct isotopic signature but without chemistry data, or consistent seasonal sampling, it is difficult to constrain soil water as an end member. In the future, soil samples could be taken more consistently with the installation of equipment like passive capillary samplers (PCAPs) as in Frisbee (2010). Future sampling efforts could also increase the number of groundwater well samples in the mountain. The mountain spring samples that we were able to take differed greatly from the mountain groundwater wells. This could indicate that springs are not actually an accurate representation of groundwater within the mountain block, but rather form a separate end-member. Conversely, if the groundwater wells are indeed drilled into alluvium, they could be representing riparian groundwater while the springs more accurately represent actual mountain block groundwater. Having more well samples, particularly deeper or better characterized wells, would help better define mountain block groundwater as an end-member. Williams Lake, a high elevation lake (3400 m) at the headwaters of the Rio Hondo, could also be sampled as a possible end member.

More well samples in the basin would also be useful to further explore the influence of MBR as well as anthropogenic activities. In particular, measuring the temperature of basin wells could be used to determine the existence of mountain block recharge. Water that is circulated deeply within the mountain block

is expected to be warmer, a thermal signature that should be detectable in basin wells. And since the temperature will vary with the rate of MBR, its influence on the basin aquifer could also be inferred or at least constrained to a maximum value (Manning, 2002). In our study area, we unfortunately do not have enough basin well samples from this sampling exercise to construct a full thermal contour map in the basin-fill aquifer beyond the mountain front. However, in the future, a concerted temperature survey of more basin wells at varying distances from the mountain front could produce the thermal data necessary for quantifying the influence of MBR. This kind of lateral survey has been helpful for constraining the effects of MBR in similar mountain front environments such as the mountain front of the Wasatch Range in Utah (Manning, 2002) and the Española Basin along the Sangre de Cristo range south of our study area (Johnson et al., 2012). In addition to a lateral survey of water well temperatures, vertical temperature profiles should also be measured, as the shape of vertical temperature profiles can be used to determine the vertical component of groundwater flow (Mansure and Reiter, 1979). This method has been applied across New Mexico including the Albuquerque Basin (Reiter, 2003) and the Española Basin (Manning, 2008). This measurement technique is more difficult to implement as it requires wells that are accessible and unobstructed by pumps. However, new or unused wells and existing monitoring wells could be used for this purpose. The distributed temperature sensing (DTS) technology discussed in Appendix A would be particularly suited for this type of down-well monitoring.

Since we have suggested that long residence-time flowpaths have a significant influence on both groundwater and surface-water in the Rio Hondo area, it could be helpful to date selected water samples to test this theory. Particular attention should be paid to mountain-front wells whose results indicate they

draw their water from a mixture of sources. Dissolved noble gas measurements, as in Manning and Solomon (2003), would help distinguish contributions from recharge at different elevations. Measurements of $^{87}Sr/^{86}Sr$ could also help constrain flow paths and the geologic formations through which groundwater is flowing. Analyses for PO_4, another agricultural input, could further identify anthropogenic influences on water in the Rio Hondo area.

CHAPTER 4

DETERMINING APPROPRIATE BOUNDARIES FOR A MOUNTAINOUS WATERSHED MODEL

Groundwater flow through bedrock is typically assumed to be negligible in a crystalline geologic environment like the Sangre de Cristos (Hearne and Dewey, 1988; Barroll et al., 2006). However, recharge (MBR) through the "impermeable" mountain block can actually be a significant contributor to the area's hydrogeology. Finding a way to model deep MBR while still accounting for important surface and vadose zone processes is challenging. Traditional watershed models either model surface-water and groundwater as completely separate systems, often neglecting the groundwater system completely, or simplify the groundwater portion too much to be useful for MBR research.

For instance, the lumped parameter Sacramento Model (Burnash et al., 1973) focuses on surface and soil water but ignores groundwater beyond listing groundwater recharge as a loss term. Other rainfall/runoff methods, such as the SCS curve number method and KINEROS2 (Woolhiser et al., 1990) address soil wetting, but not groundwater specifically. Distributed parameter models like TOPMODEL (Beven and Kirkby, 1979) and tRIBS (Ivanov et al., 2004) make some basic assumptions about groundwater behavior based on topography and surface and soil water flow. However, neither of these deal with anything beyond shallow subsurface flow and so are not particularly useful for modeling MBR. To

model deeper subsurface flow, traditional groundwater models like MODFLOW (McDonald and Harbaugh, 1988) can be used. However, these have a similar shortcoming - surface and vadose zone flow are very weakly handled, not even addressing important factors like evapotranspiration. Newer surface-water models like the USGS's PRMS (Leavesley et al., 1983) and those developed for Yucca Mountain, including INFIL (Flint et al., 2000) and MASSIF (Levitt, 2004) focus on surface and vadose zone processes but also, importantly, provide the amount of water reaching below the root zone. Since this is effectively a groundwater recharge value, it can be used to improve groundwater models by providing a more accurate top boundary input. This, in fact, is what the new generation of integrated distributed parameter models, including GSFLOW (Markstrom et al., 2008) and PIHM (Qu, 2004), attempts to do. These are coupled surface (vadose zone)/groundwater models that can be run over different time periods, making them essentially 4-D models. This temporal component is essential for planning and management under changing environmental conditions, like that predicted due to climate and land use change. The coupled surface and groundwater approach is ideal for modeling a system that incorporates both deep groundwater flow and surface drainage, like the Rio Hondo. In addition, this approach is recommended because it allows the integrated hydrologic system to be modeled with atmospheric forcing while groundwater-only models can only use recharge, for which field measurements are much less common. This is particularly relevant in our field area since the Rio Hondo is predicted to suffer varying degrees of precipitation change under different climate change scenarios (NMOSE, 2006b).

Four-dimensional models, like those descibed above, present a problem, however, when assigning both lateral and vertical model boundaries. With a surface/vadose zone-only model, the lateral boundary is simply the topographic

surface-water divide. The lateral boundaries for a groundwater-only model are typically more case-specific. There may be an obvious lithologic feature that restricts flow or a water body that provides a convenient prescribed head boundary. If the groundwater divide is known, then the boundary is easily assigned. But usually, while surface watersheds are easily delineated using topographic divides, the delineation of groundwater catchments is not nearly as straightforward. This is due to a fundamental difference between surface and groundwater flow. Determining a surface-water divide is straightforward because surface-water can be assumed to flow over the surface and through shallow soils (interflow), and to be controlled strictly by gravity and topography. However, the same assumptions cannot be made with groundwater because it is not flowing at the surface or through shallow soils, but rather, flowing as part of a larger connected aquifer system. Therefore, the overall flow patterns of the aquifer can be influenced by regional flow paths, so geology and topography must be taken into account. The aquifer material itself creates resistance to flow, another fundamental difference with surface-water flow. In short, a groundwater catchment is not completely controlled by its surface watershed, but rather can be influenced by neighboring surface watersheds (Winter et al., 2003). In addition, groundwater flow-system divides, unlike surface-water divides, can change over short periods of time, even seasonally, for both natural and anthropogenic reasons (Keen, 1992; Winter and Rosenberry, 1995; Holzbecher, 2001). Even low permeability areas with high topographic relief which may seem unlikely to support cross-basin flow, can still have subsurface transfer between surface basins (Tiedeman et al., 1997; Thyne et al., 1999; Genereux et al., 2002). Nevertheless, when groundwater data is scarce, as is the case in most mountainous areas, the groundwater divide is often assumed to be co-located with the surface-water divide. For these reasons,

an objective method of choosing model boundaries is needed in order to avoid choices based on poorly-supported assumptions. This is particularly important in a coupled surface and groundwater model since any error in groundwater flow can then propagate to the surface-water system.

Depending on the metric being evaluated, or the environmental and physical characteristics of a watershed, defining the groundwater divide based on surface topographic divides may be an appropriate choice with no detrimental effect on the overall model results. The issue is that this assumption is often made in watersheds that are poorly characterized and so, the justification for making these simplifying assumptions is unclear. For instance, the Rio Hondo watershed has few wells in the mountain block with which to characterize groundwater behavior. To simplify a groundwater model of this area, we could just assume that groundwater follows topography, but this is probably inaccurate. In a fractured crystalline hydrogeologic setting like the Sangre de Cristos, the primary permeability of the underlying bedrock is low and thus groundwater flow is dominated by secondary permeability caused by faults and fractures. Preferential flow paths along these fractures make it less likely that the water-table will follow topography and also increases the possiblity of cross-basin flow. Making the common modeling assumption that groundwater divides are the same as surface-water divides, one could therefore ignore important groundwater processes within the mountain block. This becomes especially important when trying to characterize mountain block recharge or groundwater/surface-water interactions. In a coupled groundwater/surface-water model, inaccuracies in the groundwater system will propagate to the surface-water results and vice versa, making the entire model suspect. Therefore, before developing a model, it is important to develop objective criteria to determine if the lateral model boundaries need to be

extended beyond surface-water divides in order to better incorporate deep regional groundwater flow and if so, by how much?

A related issue concerns how deep a model should extend below the surface. In a surface and vadose zone model, this bottom boundary can simply be defined at a point below the root zone or where the unconsolidated regolith transitions to solid rock. Choosing the bottom boundary for a groundwater-only model is more challenging. Typically it is based roughly on geology, in that the bottom boundary of the model is defined at the top of a geologic layer that is deemed too low in permeability to contribute significant amounts of water to the flow system. Anything below this boundary is assumed to be essentially "impermeable" bedrock. In areas where the bedrock truly does not contribute significant amounts of water to the flow system, the position of this "impermeable" boundary might have little to no effect on the calculated discharge. However, the problem arises when this boundary is placed at a stratigraphic layer that might actually host significant hydrologic flow or storage. Choosing an appropriate bottom boundary is crucial when modeling mountain-block groundwater flow. A model boundary that is too shallow can cut off deeper flowpaths, leading to misrepresentation of the flow system and errors in calculated discharge and particularly groundwater age. Water flowing deep within mountain block has a longer residence time which manifests as older measured ages in water samples. Since the age of water can be used to calibrate groundwater flow models, it is important not to ignore the potential influence of older and deeper flow. However, due to computing limitations, the model boundary cannot be extended indefinitely either. As with the lateral boundaries, it is thus important to develop an objective method for choosing the vertical boundaries of coupled groundwater and surface-water models.

4.1 Tóth Model

This issue of choosing boundary locations can be explored in the context of the Tóth model for regional groundwater flow (Tóth, 1963). This classic model, though far from a recent development, remains a common choice, even today, for basic groundwater modeling problems due to its simplicity (Haitjema and Mitchell-Bruker, 2005; Gleeson and Manning, 2008). Tóth's model represented a paradigm shift in the understanding of groundwater flow and remains one of the most influential and cited papers in hydrology (Schwartz et al., 2005; Anderson and McDonnell, 2008). The main contribution of the original paper is that it demonstrates the generation of nested groundwater flow paths on the local, intermediate, and regional scale in hummocky terrain [Figure 4.1]. This contrasts with previous work that assumed that flow was constrained to simple local flow paths (Hubbert, 1940). This makes the original Tóth model a good choice for the investigation presented here, which aims to understand the effect of inter-basin regional groundwater flow.

The Tóth model assumes a rectangular domain of incompressible steady flow in a non-deformable, isotropic, homogeneous porous media. Steady-state hydraulic head is calculated for all points using the Laplace equation $\nabla^2 h = 0$, which can be used to produce an equipotential map and flow net for groundwater flow. Using this modeling concept, we can explore how the longer intermediate and regional flow paths can affect local flow in a watershed or stream of interest such as the Rio Hondo. We vary topographic and geologic parameters to examine how these physical characteristics can change the amount and age of groundwater discharge to the valley of interest and the position of groundwater divides.

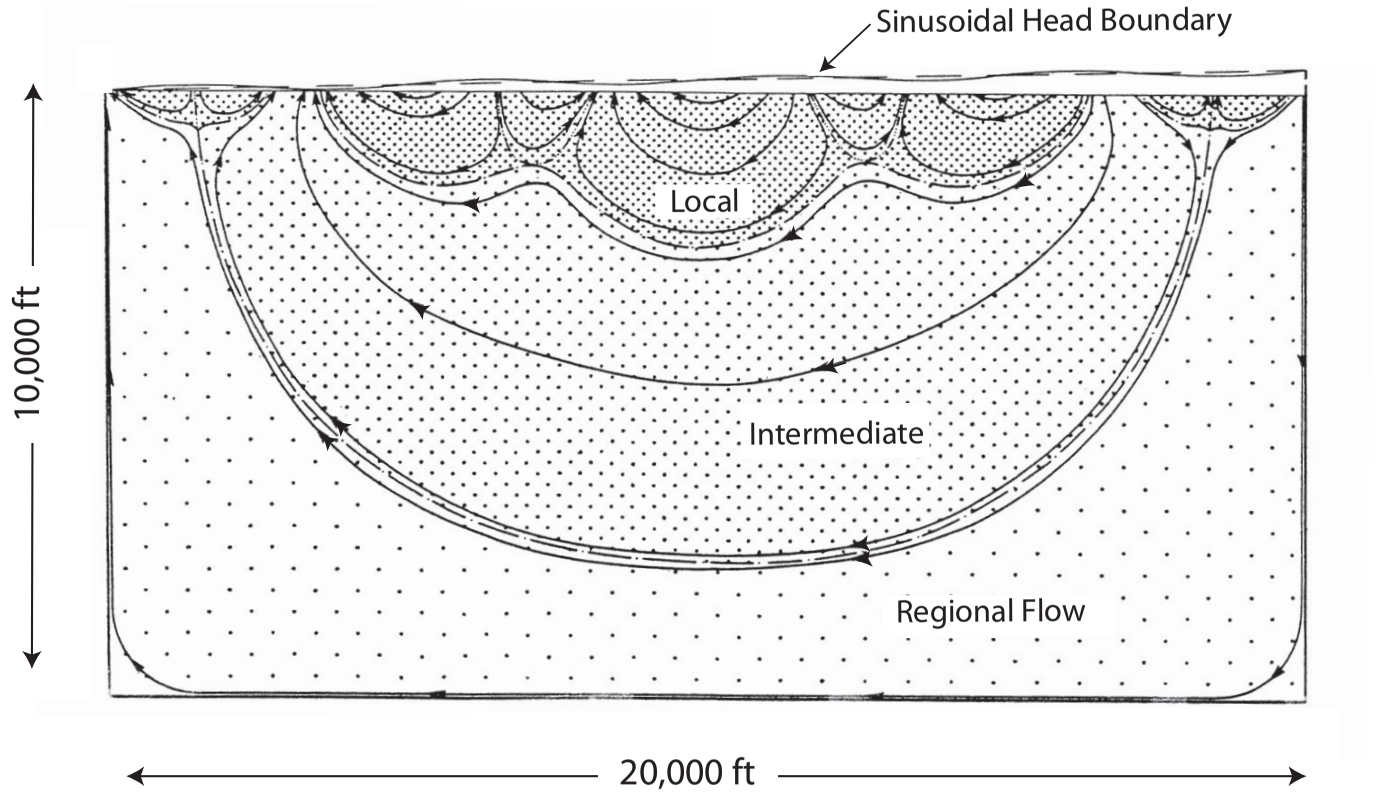

Figure 4.1: Tóth (1963) regional groundwater flow model. The regional groundwater flow model demonstrates the development of nested flow paths (on a regional, intermediate, and local scale) in hummocky terrain .

There are a few drawbacks to using this particular conceptual model. Since the Tóth model assumes that the water-table is known, we cannot use this model to determine how groundwater divides might migrate under different precipitation or recharge conditions, as may occur with climate or land use change. Therefore, future work will incorporate prediction of the water-table as a function of groundwater flow under a prescribed recharge pattern with topographically controlled discharge. The sinusoidal topography of a Tóth model is highly simplistic and unlikely to accurately describe a real-life drainage basin. Applying a realistic surface topography will therefore also be a topic of future research. Since this model uses steady flow, we are unable to evaluate storage. Long-term transients could tap basal storage in areas of very low permeability which has implications for choosing an appropriate model depth. Because it assumes a rectangular domain, the Tóth model uses a prescribed head boundary to represent topography. This limits the hummock amplitude and regional slope that can be tested. If either the amplitude or the regional slope is too large, the rectangular domain shape will no longer be a reasonable approximation fo the flow geometry. For those conditions, the results presented later will be only qualitative.

4.2 Methods

4.2.1 Model Design

The original Tóth conceptual model from Tóth (1963) was recreated using COMSOL Multiphysics 4.2a Earth Science Module [Figure 4.2]. The groundwater model consists of a rectangular domain with a sinusoidal top head boundary. Using a rectangular domain, of course, constrains this study to 2D flow, which makes it difficult to approximate real groundwater flow, which occurs in a truly

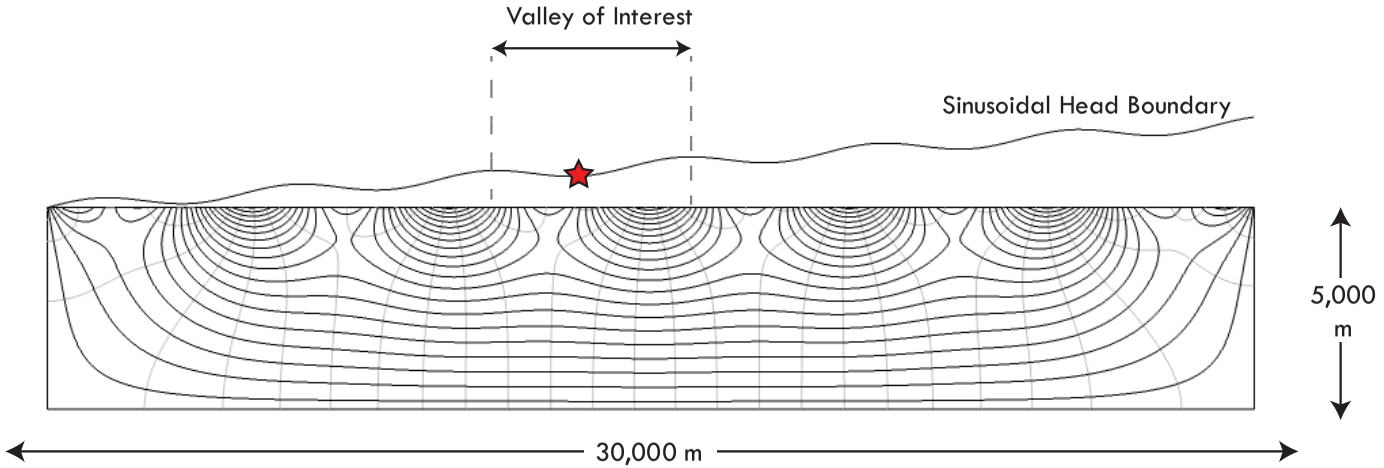

Figure 4.2: The Tóth-like model for regional groundwater flow as constructed in COMSOL Multiphysics. The sinusoidal top head boundary, representing the topographically-controlled water-table, has a slope of 0.07 (4°) and amplitude of 150 m. The rectangular domain consists of a homogeneous, isotropic porous media of K =10^{-7} m/s. The black lines represent the flow field and gray lines are equipotential lines. The valley of interest is marked with a red star.

Hydraulic conductivity (K)	10^{-7} m/s
Porosity (n)	0.10
Longitudinal dispersivity (α_L)	100 m
Transverse dispersivity (α_T)	10 m
Liquid phase diffusion coefficient (D)	10^{-9} m^2/s

Table 4.1: Base-case porous media parameter values. The chosen K and n are mid-to-high range values for fractured crystalline rock. For this analysis, the ratio of transverse (α_T) to longitudinal dispersivity (α_L) is assumed to be 1:10.

3D system. To relate this model to the real world, then, we must assume that our domain represents a 2D cross-section of a 3D watershed model. While not ideal, this simple model still provides a valuable tool for testing general concepts about the effects of model boundaries. Our base-case is a rectangle with an (x,z) origin at (0,0), a regional width (W) of 30,000 m and a thickness (B) of 5,000 m. It is composed of an isotropic, homogeneous porous media. The assumptions made for the physical characteristics of this porous media are given in Table 4.1. The water-table elevation head (H), represented by the top sinusoidal head boundary, is described by the equation:

$$H(x, z_o) = z_o + x \tan m + a \frac{\sin bx / \cos m}{\cos m} \tag{4.1}$$

where z_o is the lowest elevation of the water-table above the origin and the depth of the flow domain; a is the amplitude of the sine wave, representing the local hummock amplitude; b is the frequency of the sine wave; and m is the slope of the sine wave, representing the regional incline angle of the topography. The variable values assumed for the base-case head boundary are given in Table 4.2. The wavelength (λ) is the distance between water-table highs (or water-table lows) representing the distance across a "valley" if the water-table mimics topography. This head boundary symbolizes a water-table that is a subdued expression of the

Slope (m)	0.07
Amplitude of sine wave (a)	150 m
Wavelength (λ)	5000 m
Frequency of sine wave (b)	$2\pi/\lambda$
Base elevation (z_0)	5000 m
Regional model width (W)	30000 m
Regional model thickness (B)	5000 m

Table 4.2: Base-case top head boundary parameter values. The m and a values are those given for low relief areas in Gleeson and Manning (2008). The λ and b values were chosen so that the valley of interest is surrounded by at least 2 mountain/valley pairs on either side, reducing lateral boundary effects. The z_o (model thickness) value is deliberately large to reduce vertical boundary effects.

surface topography in hummocky terrain.

In the flow model, the bottom and sides of the model are no-flow boundaries ($\frac{\partial h}{\partial z} = 0$ and $\frac{\partial h}{\partial x} = 0$ respectively, where h is head). The top boundary is the sinusoidal head boundary defined by Equation 4.1. The initial head value in the numerical solution is set to z_o. In the groundwater age transport model, the bottom and sides are no-flux boundaries ($\frac{\partial A}{\partial z} = 0$ and $\frac{\partial A}{\partial x} = 0$, respectively where A is mean age along a streamline). The top boundary is an open boundary where A = 0 yrs in recharge areas and $\frac{\partial A}{\partial z} = 0$ in discharge areas. The entire rectangular domain serves as an initial uniform age source ($\dot{A}$) where $\dot{A} = n(year)^{-1}$.

A coupled Darcy flow and groundwater age transport model is applied to the domain. Darcy's law for flow in an anisotropic, heterogeneous porous medium is defined as $\vec{q_h} = -\bar{\bar{K}}\nabla h$ where $\vec{q_h}$ is Darcy velocity and $\bar{\bar{K}}$ is the hydraulic conductivity tensor. By using Darcy's law to define specific discharge in the steady-state conservation equation $\nabla \cdot \vec{q_h} = 0$, we get the Darcy-based steady state groundwater flow equation used for the flow model :

$$\nabla \cdot \bar{\bar{K}}\nabla h = 0 \tag{4.2}$$

The transport equation for age is based on Goode (1996):

$$\vec{v} \cdot \nabla A - \nabla \cdot \bar{\bar{D}} \nabla A - n = 0 \tag{4.3}$$

where $\vec{v} = \vec{q_h}/n$ is seepage velocity, n is porosity, and $\bar{\bar{D}} = D_{ij}$ is the diffusion-dispersion tensor defined in Bear (1972):

$$D_{ij} = \alpha |\vec{v}| \delta_{ij} + (\alpha_L - \alpha_T) v_i v_j / |\vec{v}| + D_m^* \tag{4.4}$$

where α_L and α_T are the longitudinal and transverse dispersivities, D_m^* is the effective molecular self-diffusion coefficient, and δ_{ij} is the Kronecker delta function. This sequentially coupled model is solved at steady state.

The base-case provides six wavelengths of the sinusoidal signal over the width of the domain, with each valley symbolizing a river or tributary. Unlike Tóth (1963), we are not interested in the overall regional groundwater system, but rather the effect the regional groundwater system has on a local drainage of interest, such as the Rio Hondo. Thus, a valley of interest is chosen from the mountain/valley pairs for further analysis [Figure 4.2]. This valley of interest is the focus for our analysis and is located in the middle of the larger model to minimize regional boundary effects.

4.2.2 Metrics

The following metrics were used to quantify the sensitivity of a watershed model to changes in boundary locations and physical and environmental parameters:

1) Groundwater discharge to the Valley of Interest

2) Mean age of all discharge to the Valley of Interest

3) Location of the groundwater divides bounding the Valley of Interest

Discharge and mean age were chosen because they are typically simulated in hydrogeologic models and used to calibrate models to field measurements. The location of the groundwater divides is an important metric since it can identify scenarios when groundwater divides either differ from or are essentially the same as surface-water divides. It can be used to decide how wide the model needs to be in order to adequately capture cross-basin flow.

In our COMSOL model, the total discharge to the valley of interest is calculated by integrating the upward (positive) vertical advective flux along the top boundary in the valley of interest:

$$Q = \int_{x1}^{x2} q_z^+ \, dx \tag{4.5}$$

where Q is the discharge to the valley of interest, $x1$ is the x-coordinate for the peak downhill of the valley of interest, $x2$ for the uphill peak, and q_z^+ is the positive vertical Darcy convective flux (m/s). While the limits of integration in Equation 4.5 may include areas of groundwater recharge (downward flux), this recharge is ignored by choosing only discharge (upward flux) for the intergrand. Therefore, it effectively integrates between hinge points, where the water transitions from recharge to discharge.

The "flux concentration" of groundwater age (Aq_z) along the top boundary represents the flux-weighted age of the local groundwater discharge. The mean age of all the groundwater discharging to the valley of interest is calculated by dividing the flux-weighted age of the discharge by the total discharge:

$$\bar{A} = \frac{\int_{x1}^{x2} A q_z^+ \, dx}{\int_{x1}^{x2} q_z^+ \, dx} \tag{4.6}$$

where $\bar{A}$ is the mean age of all the groundwater discharge to the valley of interest and $x1$ and $x2$ are the same as in Equation 4.5.

Although the model we are using assumes that the water-table is a subdued replica of the surface topography, the groundwater divide, as discussed earlier, is not necessarily the same as the surface-water divide. We have defined the groundwater divide as the point above which any recharged water discharges to the uphill watershed and below which any recharged water discharges to the downhill watershed [Figure 4.3]. This point is identified using visual inspection of point-controlled streamlines in COMSOL, which are streamlines originating at specified points along the top boundary of the domain, representing recharge flowpaths. The figure illustrates how flow tubes that originate outside the topographically defined boundaries of the valley of interest, can still contribute groundwater flow to the valley of interest.

4.2.3 Sensitivity Permutations

Using the metrics above, we quantified the sensitivity of the watershed model to changes in the lateral or the vertical boundary locations. We also ran sensitivity analyses for changes in topography, hydraulic conductivity, depth-dependent permeability decay rate, anisotropy, and heterogeneity. Table 4.3 provides a summary of all the sensitivity permutations conducted. The following sections provide the motivation behind and explanation of these model runs.

Model Width The tendency to simply use the surface-water divide as a proxy for the groundwater divide is driven not just by lack of field data, but also by

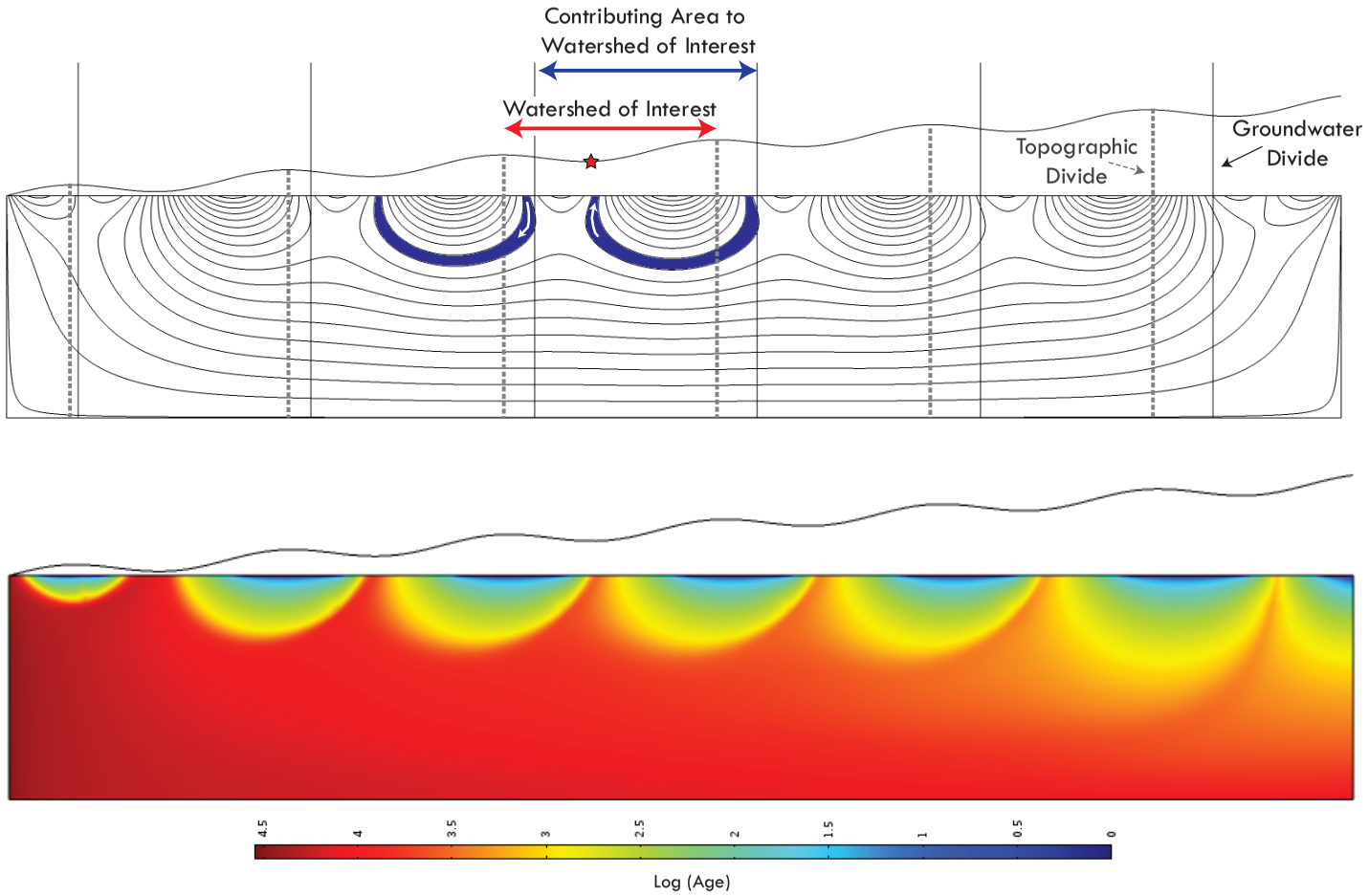

Figure 4.3: Differences between groundwater divides and topographic divides plotted on a regional flow model. Topographic divides are represented by the vertical dashed lines and the groundwater divides are represented by vertical solid lines. The color scale in the bottom figure represents age in years on a logarithmic scale.

Parameter	Range
Truncated model width	6 model widths described in Figures 4.4 & 4.5
Truncated model thickness	25 - 5000 m
Regional Slope (m)	3° - 10°
Hummock Amplitude (a)	50 - 250 m
Hydraulic Conductivity (K)	10^{-13} - 10^{-3} m/s
Depth decay constant (β)	0.001 - 0.1 m^{-1}
Anisotropy (K_h/K_v)	1 - 100
Heterogeneity	3 dip angles (15°, 30°, 45°)

Table 4.3: Summary of all Sensitivity Permutations

limitations in computing power. After all, the larger the model, the more computationally challenging, particularly for a full 4D coupled surface/groundwater model. The issue is that choosing this smaller boundary potentially ignores any longer flowpaths originating in neighboring basins. To determine the extent to which important regional flowpaths are excluded, we chose six narrower model domains cut out of the original regional model shown in Figure 4.3, using topographic highs and/or lows to define the lateral boundaries of each model. Three symmetric nested models were constructed [Figure 4.4], including the traditional peak-to-peak topographically-defined surface watershed (Trad), an extension of the traditional watershed to the surrounding valleys (Ext1), and an extension to the next peaks (Ext2). We also simulated 3 nested scales that are asymmetric with regards to the valley of interest [Figure 4.5]. The largest incorporates the entire mountain/valley pair (MtValley). The next represents a mountain-centered approach and includes only the uphill mountain block (MtCenter). The last is simply a hillslope model, incorporating only the uphill side of a valley (Hillslope). For each of these models, the discharge and the mean age of groundwater discharge were calculated according to Equations 4.5 and 4.6. The models are constructed of isotropic, homogeneous porous media according to the parameter

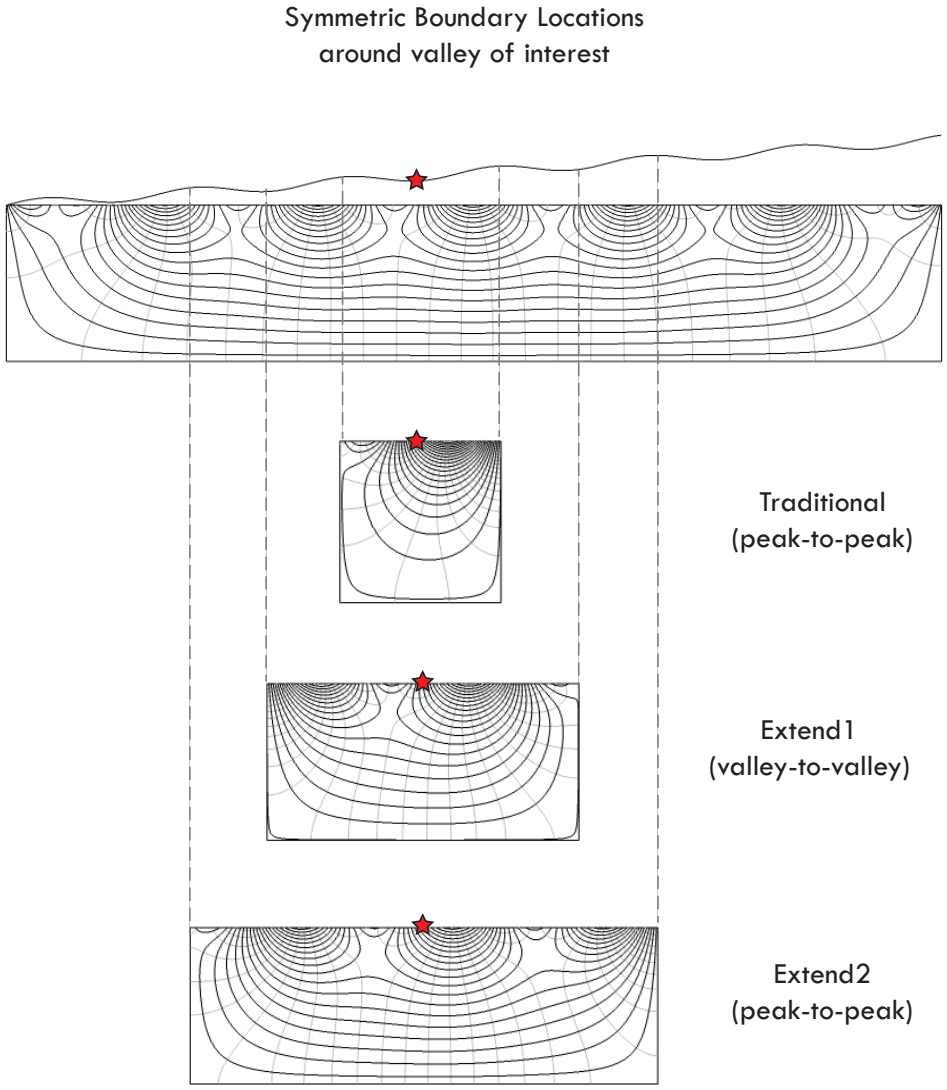

Figure 4.4: The three symmetric model boundary locations used for sensitivity analysis. The valley of interest is marked with a red star. The black lines represent the flow field and gray lines are equipotential lines. The dashed lines indicate how far the sinusoidal top head boundary of each nested model extends.

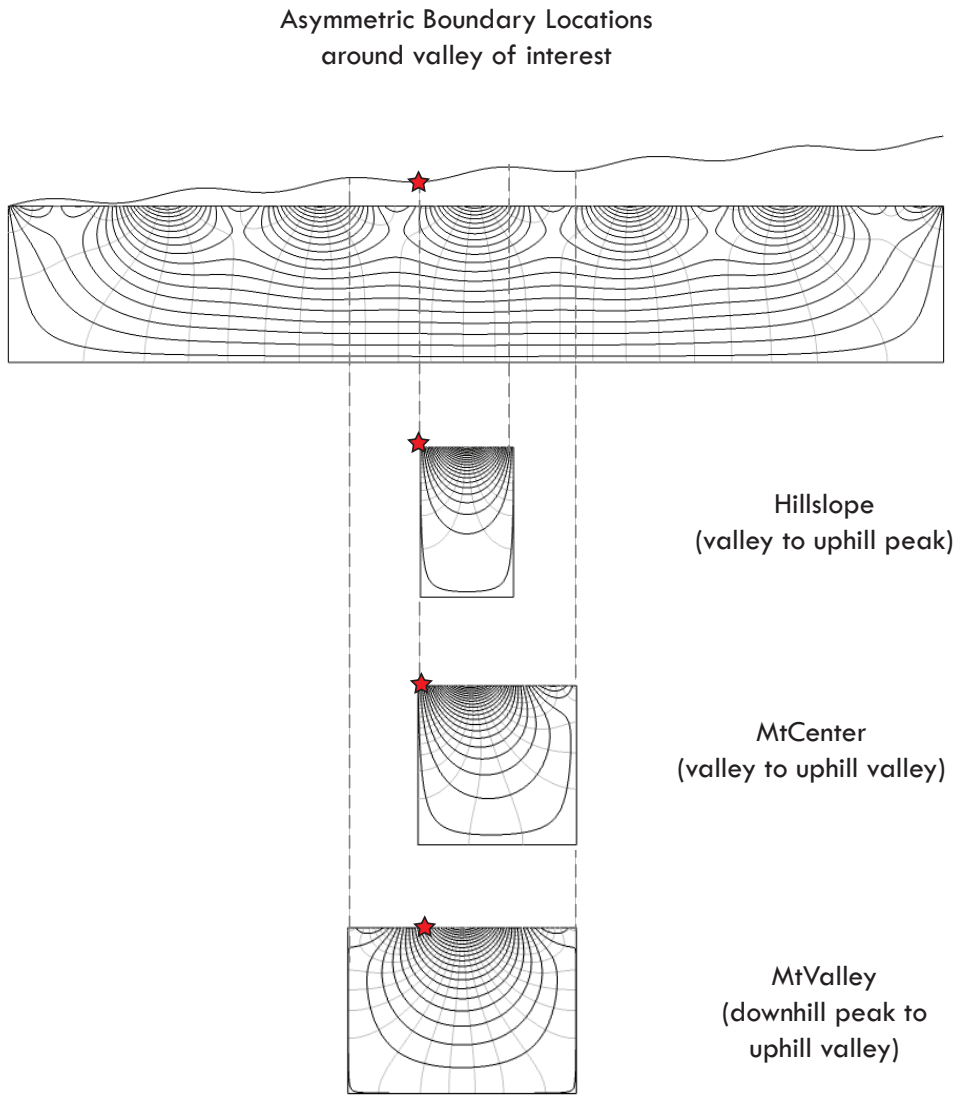

Figure 4.5: The three asymmetric model boundary locations used for sensitivity analysis. The valley of interest is marked with a red star. The black lines represent the flow field and gray lines are equipotential lines. The dashed lines indicate how far the sinusoidal top head boundary of each nested model extends.

values given in Tables 4.1 and 4.2.

Since the results of the original regional 30,000 x 5,000 m model should be free of local boundary effects, we use it as the "correct" value against which we can compare the results from other simulations. In this way, we can use error in discharge and error in age as two more metrics in our analysis. The discharge error is calculated by comparing the simulated values for discharge and age against these "correct" values:

$$\text{Discharge Error} = 100 * (Q - Q_o)/(Q_o) \tag{4.7}$$

$$\text{Age Error} = 100 * (\bar{A} - \bar{A}_o)/(\bar{A}_o) \tag{4.8}$$

where Q_o and $\bar{A}_o$ are the calculated discharge and mean age to the valley of interest in the original regional model and Q and $\bar{A}$ are from the nested model in question. This allows an objective measure for determining which choice of model width produces the least altered results.

Model Thickness If geology is well known, the bottom model boundary is typically set at an "aquitard," or a stratigraphic layer that excludes significant hydrologic flow. The issue is that even when geology and thus hyraulic properties are not well characterized, the bottom model boundary is placed arbitrarily at a "bedrock" depth which may or may not actually be impermeable. We test the appropriateness of this assumption using two methods. First, even if the flow field is independent of stratigraphy, there is likely a cut-off below which extending the model boundary does not significantly improve the model. Zijl (1999) proposed an "effectively impervious base" that was defined through a Fourier analysis in terms of the decay of groundwater specific discharge with depth. This decay or

penetration depth can be calculated in terms of the wavelength of the sinusoidal top head boundary:

$$\delta = \lambda \sqrt{\frac{K_v}{K_h}} \tag{4.9}$$

where δ is the penetration depth, λ is the wavelength of the sinusoidal water-table, K_v is the vertical hydraulic conductivity and K_h is the horizontal hydraulic conductivity. This argument posits that, based on the limited forcing from the top sinusoidal head boundary, the flow velocity will decrease with depth to a point where it becomes insignificant. Zijl (1999) assumed this depth to be where magnitude of specific discharge is 0.002 of the value near the surface. Therefore, a Tóth-like model could be cut off at this depth with little-to-no effect on the overall flow field. To test this, we consider the vertical trend in specific discharge in our base-case groundwater model and an anisotropic model. The base-case is isotropic, so $\frac{K_v}{K_h}$ = 1 and λ = 5000 m, so that according to Equation 4.9, δ = 5000 m. The anisotropic variation on our base-case has $K_v = 0.10K_h$. In this case, δ = 1581 m. To determine whether a cut-off exists, the specific discharge is calculated along 3 vertical cross-sections uphill, downhill and in the center of our valley of interest. The depth at which the specific discharge has stopped changing in these "wells" is then compared to the values generated from Equation 4.9. These results are shown later in Section 4.3.1.

This method is a good validation exercise for our model, but it focuses mainly on the overall regional flow system, while we are mainly concerned with only a small portion of this system, our valley of interest. In particular, how deep does the model need to extend in order to provide an accurate estimate for discharge and age to our valley of interest? To examine the effect of model thickness on only this valley, each nested model width is simulated with model thicknesses

ranging from the 5000 m of the original regional model down to 25 m. This thin model thickness could represent a shallow zone of enhanced permeability capping an impermeable bedrock. All nested models are isotropic, homogeneous, and use base-case parameter values [Tables 4.1 and 4.2]. Only the model thickness is varied; z_o is constant. Discharge and average age are calculated using Equations 4.5 and 4.6 and the errors are measured using Equations 4.7 and 4.8. The values calculated for the original regional model are used for Q_o and $\bar{A}_o$.

Topography Since our model assumes that the water-table follows the topography, any topographic variations are likely to significantly influence the deep groundwater flow system. As mentioned before, the sinusoidal head boundary is unlikely to be similar to real topography, and in any case, does not account for 3D variations in topography. However, for the purposes of this sensitivity analysis, we approximate changes in topography for each nested model width by varying the regional slopes and then the hummock amplitudes of the sinusoidal top head boundary. One of the major limitations of the Tóth model is that this top head boundary is applied to the flat top boundary of a finite rectangular domain. This restricts the values of regional slope and local hummock amplitude that can be used before the model becomes completely unrealistic. Therefore, we do not attempt to model unreasonably steep models but constrain our range to the low (Appalachains) to intermediate (Rockies) values given in Gleeson and Manning (2008). A range in slope from 0.05 (3°) - 0.18 (10°) and a range in amplitude from 50 - 250 m is used represent the variation between different mountainous areas [Figure 4.6]. All nested models are isotropic, homogeneous, and use base-case parameter values [Tables 4.1 and 4.2]. Only m is varied in the case of the regional

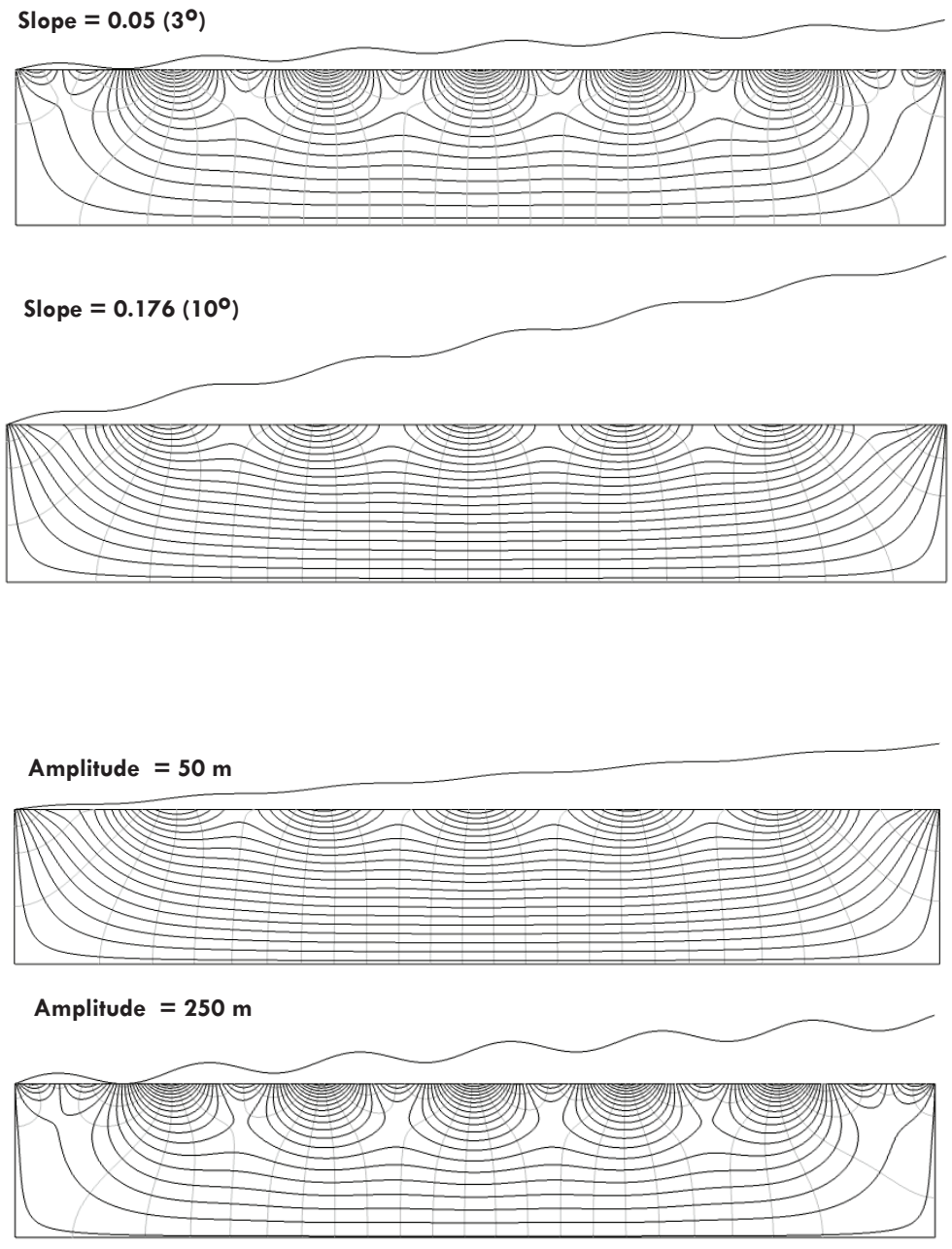

Figure 4.6: Topographic variations used in simulations. Note the amplitude of the head boundary is not to scale with the domain, but is exaggerated approximately 4x to emphasize the shape.

slope sensitivity analysis, and a in the amplitude analysis. Discharge and average age are calculated using Equations 4.5 and 4.6 and the errors by solving Equation 4.7 and 4.8. Q_o and $\bar{A}_o$ are the values calculated for the original regional model with the same m (or a) value as the nested model in question.

Permeability Hydrologic studies are conducted in areas with vastly different geology. The greatest effect geology has on hydrologic flow is on groundwater movement, which is controlled by the hydraulic conductivity of the rock. Therefore, changes in geology are, for this exercise, represented simply by variations in hydraulic conductivity (K). Each nested model width was simulated using a range of natural consolidated rock K values from 10^{-3}m/s (permeable basalt) to 10^{-13}m/s (unfractured crystalline rocks), as given in Freeze and Cherry (1979). It should be reiterated that we do assume the model is isotropic and isothermal. Therefore, we ignore the possibility of natural convection. In addition, we are not accounting for the natural increase in temperature with depth nor the accompanying decrease in fluid density and viscosity that leads to greater net hydraulic conductivity at depth. Rather, this simple model is designed to just test for the general sensitivity to a change in overall hydraulic conductivity. All nested models are isotropic, homogeneous, and use base-case parameter values [Tables 4.1 and 4.2]. Only K is varied. Discharge and average age are calculated using Equations 4.5 and 4.6 and the errors by solving Equation 4.7 and 4.8. Q_o and $\bar{A}_o$ are the values calculated for the original regional model with the same K value as the nested model in question.

Permeability Decay with Depth The extent of active flow is difficult to define, but an extremely important factor when considering deep groundwater flow.

One method is to define an effective stress-dependent permeability depth curve, representing pore and fracture closure under pressure with depth, based on geology. For instance, the permeability depth curve in a sandstone environment has been defined as $log(log(K/K_o)) \propto depth$ where K_o is the near surface permeability and K the permeability at depth (Belitz and Bredehoeft, 1988). The depth of "active flow" can also be measured with age or temperature tracing and aquifer tests. Studies in fractured crystalline rock environments have indicated that this active flow zone extends from 100 m below the surface (Boutt et al., 2010) to 200 m (Manning and Caine, 2007). However, others have found that permeability has little to no depth dependence in some crystalline rock (Brace, 1984). Clarke and Burbank (2011) discovered that even when some areas do have geomorphically-caused depth-dependent permeability gradients, these gradients are only applicable to a shallow depth, below which point the bedrock is uniformly fractured with depth due to tectonic forces. In fact, surprisingly high conductivity values ($4.07x10^{-8}$ m/s) have been observed even in a 4 km deep crystalline aquifer (Stober and Bucher, 2005). Similarly deep circulation depths have been observed in New Mexico as well, with a hydraulic conductivity around 10^{-8} m/s estimated at 2 km depth in Socorro, NM (Mailloux et al., 1999). The depth of active flow can be extremely site-specific and there is little consensus in the literature defining a common permeability depth curve. Therefore, to represent the possibility of some depth dependence on confining pressure (Ingebritsen and Sanford, 1998; Manning and Ingebritsen, 1999) for this sensitivity analysis, we simply assume that K decays exponentially with depth:

$$K = K_o e^{-d\beta} \tag{4.10}$$

where K is the hydraulic conductivity at a point, K_o is the hydraulic conductivity at the top boundary, d is the depth (H-z), and β is the depth decay constant.

Magnitude-controlled streamlines generated in COMSOL can be used to create stream-tubes containing equal amounts of flow. Given a particular β value, the depth of the lowest streamline can therefore give an approximation for the corresponding depth of active flow to the level of precision set by the number of streamlines drawn [Figure 4.7]. In this case, we chose 99 streamlines so that the bottom-most streamline indicates the point above which 99% of the flow is captured. From this point on, this depth is referred to as the decay depth (d_D). In these simulations, this point generally falls where the K value is $10^{-3}K_o$. If this is used as the cutoff for determining d_D then, according to Equation 4.10:

$$d_D = 6.9/\beta \tag{4.11}$$

Each nested model width is simulated with a range of β from 0.001 - 0.1 m^{-1}. According to Equation 4.11, this corresponds to a range of d_D from 70 m - 5000 m. Note that in this context, our original isotropic model [Figure 4.3] represents a case where the d_D is essentially infinite. All nested models are isotropic but heterogeneous due to the change in K with depth. Each is constructed using base-case parameter values [Tables 4.1 and 4.2] and the depth decay constant (β) is the only parameter varied. Discharge and average age are calculated using Equations 4.5 and 4.6 and the errors by solving Equation 4.7 and 4.8. Q_o and $\bar{A}_o$ are the values calculated for the original regional model with the same β value as the nested model in question.

Anisotropy An important constraint on the development of deep groundwater flow paths is the difference between horizontal (K_h) and vertical (K_v) hydraulic conductivity. Often, K_h far exceeds K_v, particularly in sedimentary and volcanic

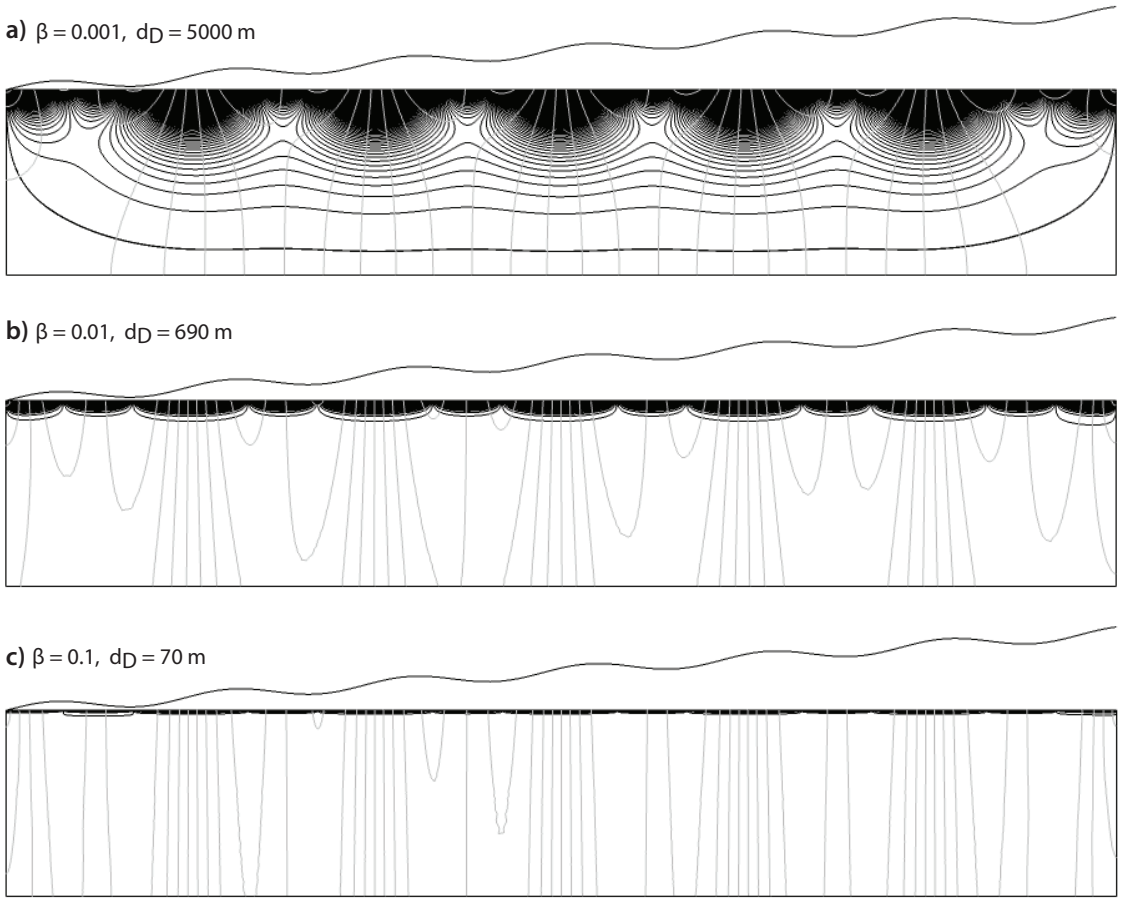

Figure 4.7: How to determine decay depth. The decay depth (d_D) is defined as the depth at which K=$10^{-3}K_o$, which is approximately equal to K at the bottom-most streamline in the figures above. This indicates the point above which 99% of the flow is captured.

rocks, restricting groundwater to shallow local flow paths. To determine sensitivity to this directional difference in K, each nested model width is simulated at anisotropy ratios (K_h/K_v) ranging from 1 to 100, with K_h remaining constant [Figure 4.8]. All nested models are therefore anisotropic but homogeneous. Each model is constructed using base-case parameter values [Tables 4.1 and 4.2] and only K_h/K_v is varied. Discharge and average age are calculated using Equations 4.5 and 4.6 and the errors by solving Equation 4.7 and 4.8. Q_o and $\bar{A}_o$ are the values calculated for the original regional model with the same K_h/K_v as the nested model in question.

Heterogeneity There are many areas that cannot be described by a simple homogeneous model. In areas of complicated geology , the different hydraulic conductivities of statigraphic layers can accelerate, retard, or refract flow, severely altering the flow field. The positioning of different layers, including the dip angles of layers, can determine these flow patterns. Freeze and Witherspoon (1967) attempted to address this issue by creating Tóth-like models with layers of different hydraulic conductivity values to show how heterogeneous geology alters flow paths. We re-create similar models in COMSOL but with a focus on the local valley of interest, rather than on the regional flow system. The heterogeneous model was constructed with areas of high K (10^{-5} m/s) corresponding to valleys and low K (10^{-7} m/s) to the more resistant peaks [Figure 4.9]. It should be noted that while we assume these layers extend the full thickness of the model (about 5 km), this is unrealistic for a system like the Rio Hondo watershed in the Sangre de Cristos. While it is potentially applicable to other real systems, such as some in the Basin and Range province, it is meant more as a first-cut approximation of the

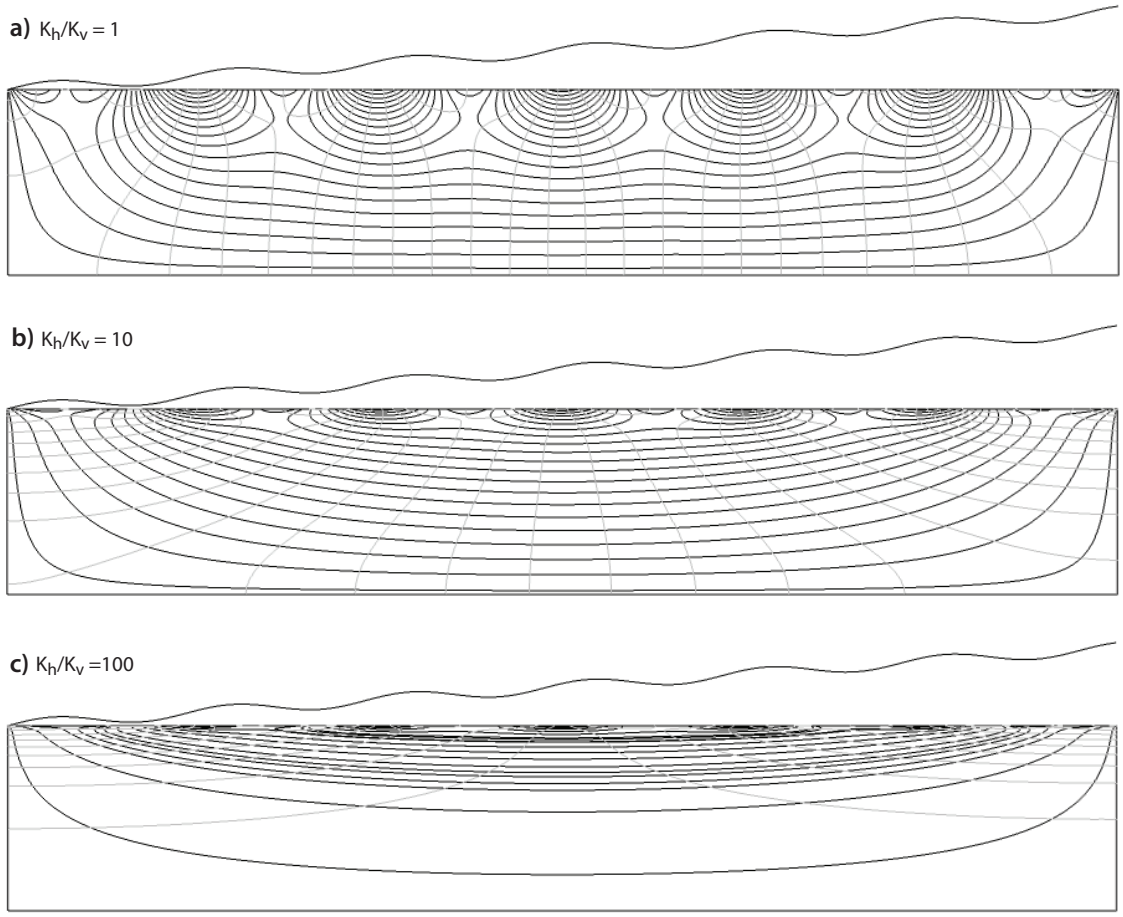

Figure 4.8: Anisotropic models with varying K_h/K_v ratios.

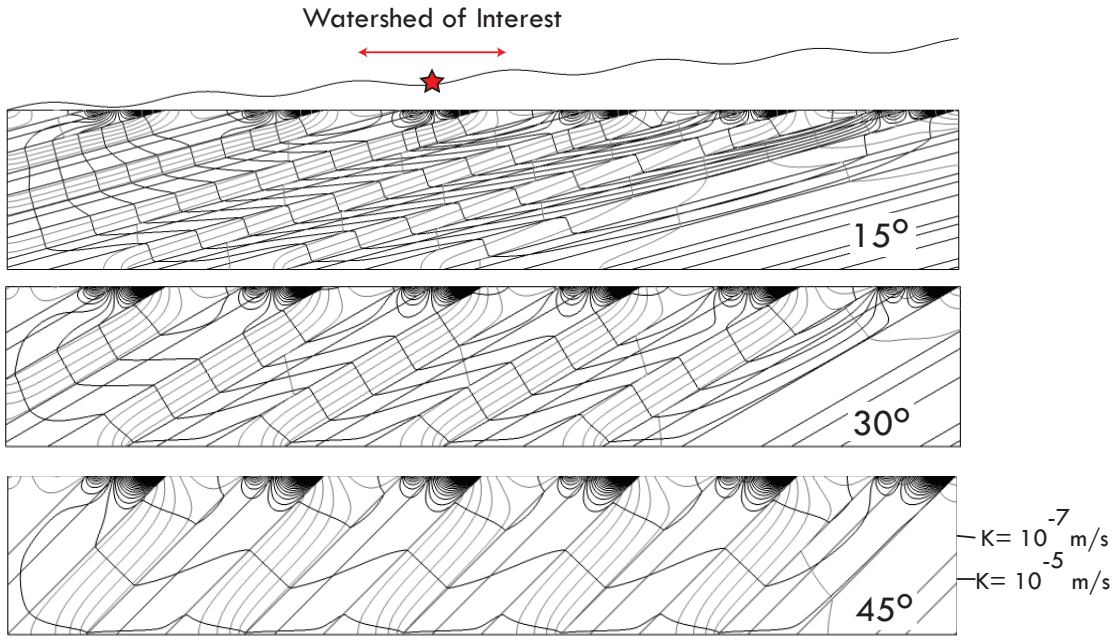

Figure 4.9: Heterogeneous models with dipping beds. The beds underlying valleys (defined by the topography of the head boundary) is assigned a high K (10^{-5} m/s) and the beds underlying peaks, which are assumed to be more resistant, are assigned a low K (10^{-7} m/s). Note the width of the beds changes when the dip angle changes in order to keep the beds aligned with the surface features.

effects heterogeneous layers have on the groundwater flow system. Each nested model width was run with dip angles of 15°, 30°, and 45°. All nested models use base-case parameter values [Tables 4.1 and 4.2] and the K of the stratigraphic layers is the only parameter varied. Discharge and average age are calculated using Equations 4.5 and 4.6 and the errors by solving Equation 4.7 and 4.8. Q_o and $\bar{A}_o$ are the values calculated for the original regional model with the same dip angle as the nested model in question.

4.3 Results and Discussion

4.3.1 How Thick Should a Model Be?

The results of this modeling exercise indicate that there is a cutoff depth, as proposed by Zijl (1999), below which there is little significant flow and the model can be truncated [Figure 4.10]. The penetration depth δ, as calculated in Equation 4.9, should be 5000 m for the isotropic base-case where $K_v = K_h$, and 1581 m for the anisotropic case where $K_v = 0.10K_h$. These values match the depth at which Darcy velocity in our simulations becomes essentially constant with depth, indicating that truncation at this point would have no effect on the valley of interest.

The results also indicate that increasing model thickness will increase discharge (Q) and mean age ($\bar{A}$) in our valley but there is a point below which increasing the model thickness causes no change to these metrics [Figure 4.11a,b]. The model thickness at this point also corresponds with the model thickness at which the location of the groundwater divide stops changing [Figure 4.11c]. These effects are likely caused by truncation of flow lines. When the bottom boundary is shallow, then deeper intermediate and regional flow paths do not

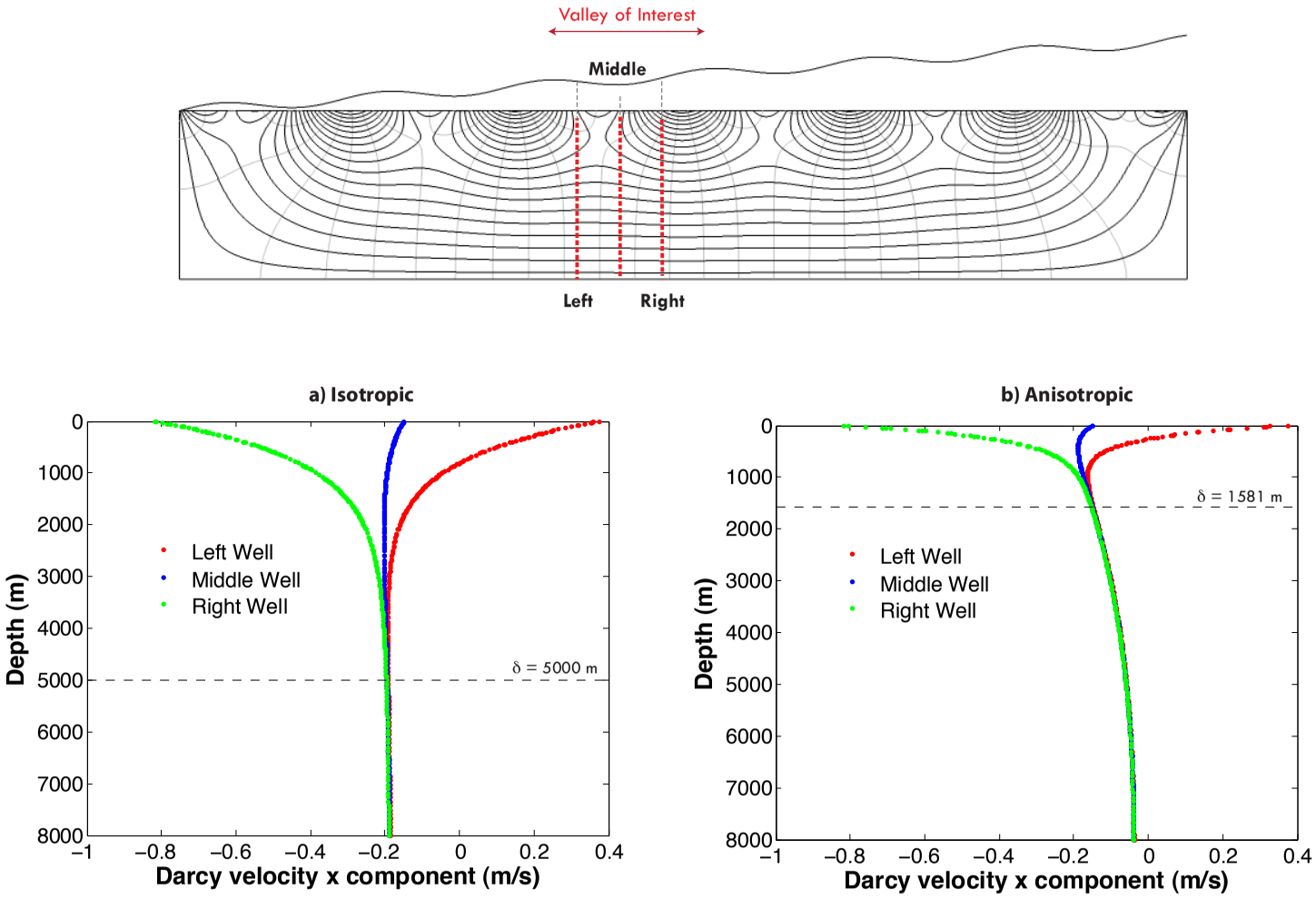

Figure 4.10: Ideal model thickness determined by Darcy velocity. The dashed lines indicate the value calculated using the equation from Zijl (1999) [Equation 4.9]. In the isotropic case, $K_v = K_h$ and in the anisotropic case, $K_v = 0.10K_h$

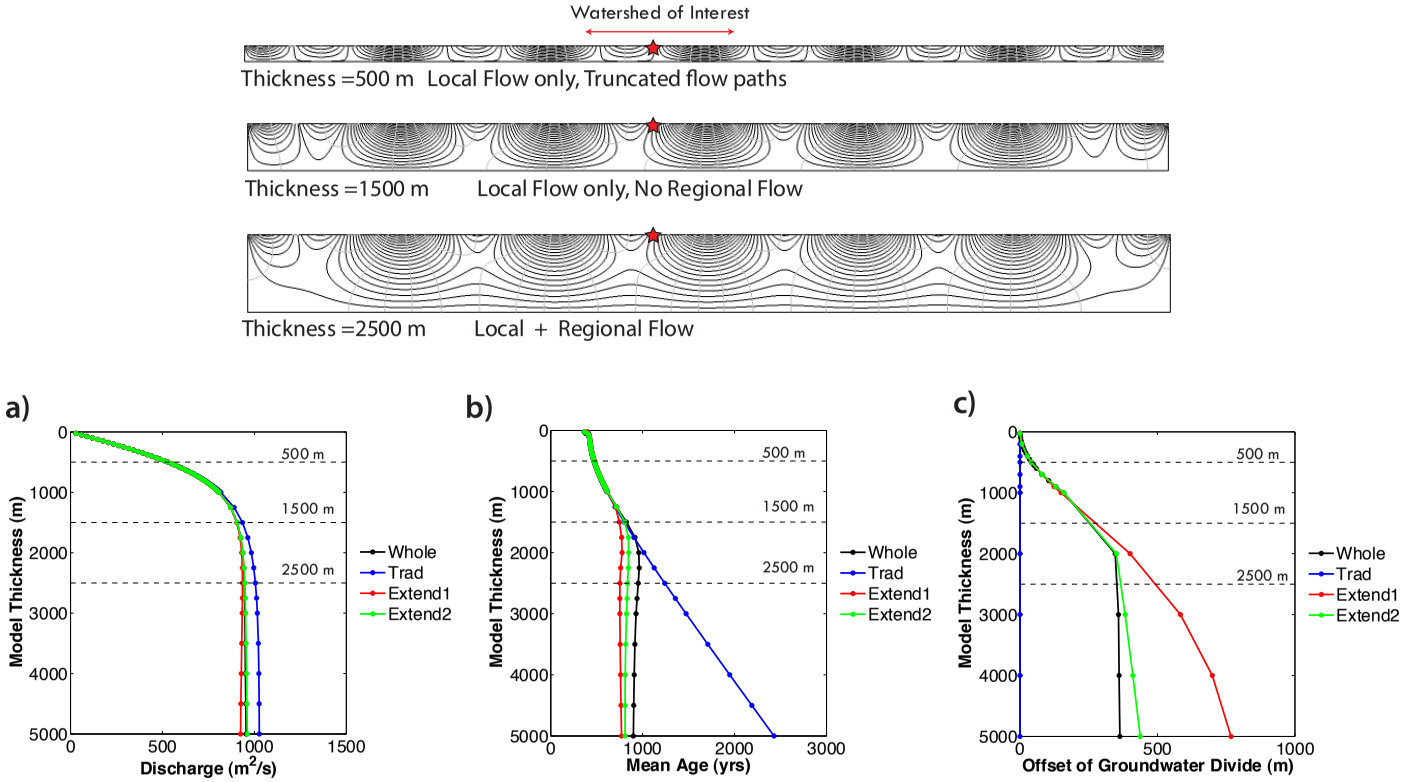

Figure 4.11: Determining ideal model thickness using Q and $\bar{A}$. The top figure shows the flow field at different model thicknesses. The bottom figures show the Q and $\bar{A}$ values and groundwater divide location calculated at different model thicknesses. The dashed lines in the bottom figures indicate the three model thicknesses shown in the top figure.

form. But as the bottom boundary gets deeper, more of these intermediate or regional flow paths form in the model. These flow paths contribute discharge to the valley of interest, so Q increases as more flowpaths are captured. Since these deeper flow paths have traveled farther, they are older and so, increase the mean age of the valley of interest. At a certain thickness, however, the model also begins to include regional and intermediate flow paths that do not discharge to the valley of interest. This explains the plateau in Q, $\bar{A}$, and groundwater divide location after a certain increase in model thickness.

It should be noted that this plateau occurs in all the model widths except for the traditional (Trad) model width in which $\bar{A}$ instead keeps increasing with model thickness [Figure 4.11b]. As the model thickness increases, water can penetrate deeper and become older. In the wider model widths (Ext1, Ext2) some of these long deep flow paths are able to discharge beyond the valley of interest. However, the model boundaries of the Trad model width "trap" these long flowpaths that would otherwise leave the watershed and instead force them to discharge to the valley of interest [Figure 4.12]. This "trapping effect" biases the $\bar{A}$ towards much older ages as the model thickness, and therefore maximum age, increases.

For all other model widths, this plateau in Q and $\bar{A}$, indicates an "optimal model thickness" beyond which extending a model becomes more resource - intensive while not actually improving the model. For our base-case, this optimal model thickness falls somewhere between 2000 - 3000m, similar to the thickness used in the original Tóth (1963) model (3048 m) and actually shallower than the optimal model thickness we estimated using Equation 4.9 from Zijl (1999). This optimal thickness will likely change in scenarios with different geology or topography, but could easily be re-calculated using the same method as this base-case.

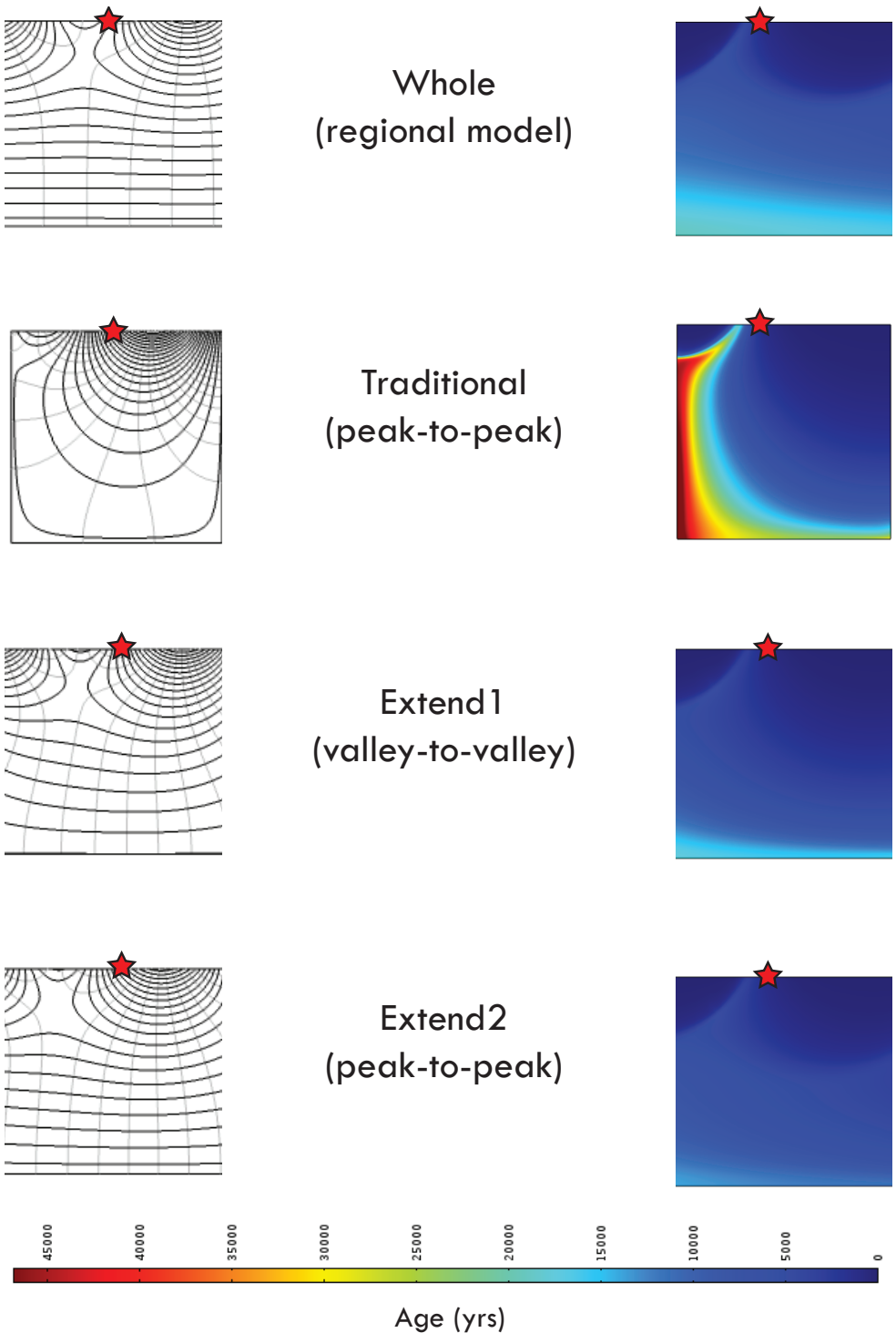

Figure 4.12: Demonstration of the trapping effect. The left column shows the flow field in the valley of interest at each model width, where black lines are flow lines and gray lines are equipotential lines. In the right column, color represents age in years. The red star marks the valley of interest.

This optimal model thickness does not, of course, apply to those scenarios when the natural flow system, in actuality, only encompasses a smaller thickness. In this case, the truncated simulations are likely representative of what is actually happening in that system. However, the actual thickness of a flow system is usually not well known. Therefore, these simulations point out the importance of picking an appropriately deep model thickness since even small changes in this parameter can have a large effect on calculated values for Q and $\bar{A}$.

4.3.2 How Wide Should a Model Be?

The results are less clear about defining an optimal model width. Even when the only parameter varied is the model width, it is clear that discharge (Q) and mean age ($\bar{A}$) in our valley of interest are affected very differently [Figure 4.13]. For discharge, the Ext2 model width provides the discharge value most similar to our desired result, the value calculated in the original regional model. Ext1 also provides a very similar discharge, but slightly lower. Trad and MtValley both overestimate discharge while MtCenter and Hillslope underestimate discharge, likely due to their smaller surface area.

The mean age results further emphasize differences between model widths. Again, Ext1 and Ext2 provide good estimates, but the remaining model widths all severely overestimate $\bar{A}$. This is due to the "trapping effect" discussed earlier. Therefore in this case, wider model widths (Ext1, Ext2) are recommended over the traditional (Trad) model width. Asymmetric model widths do not seem to provide any advantage over the Trad model for discharge or mean age calculations, and indeed, should probably be ruled out based on their unrealistic results.

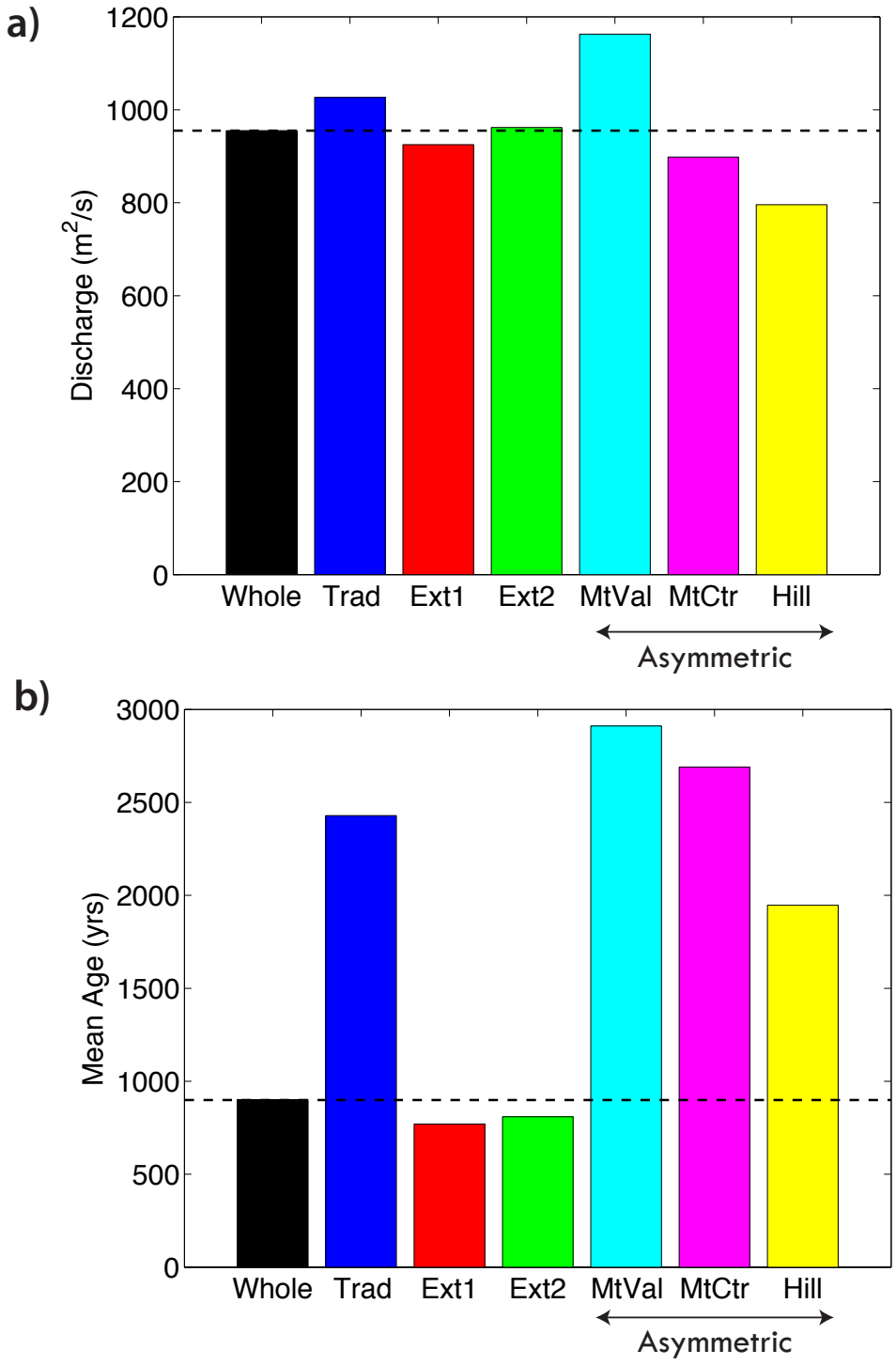

Figure 4.13: Sensitivity of metrics to model width. The black dashed line represents the Q (or $\bar{A}$) value produced by the original regional model.

Sensitivity to Hydraulic Conductivity Discharge to the valley of interest (Q) is largely controlled by the hydraulic conductivity (K) and as expected for a Darcy flow model, Q increases linearly with increasing K for all model widths [Figure 4.14a]. For discharge calculations, the effect of model width has the same results as the previous section: the wider model widths (Ext1, Ext2) provide the best discharge calculation, Trad and MtValley overestimate discharge, and MtCenter and Hillslope underestimate discharge. It should be noted that for any particular model width, the overall pattern of flow is not sensitive to K and only the amount of discharge travelling through the flow system changes. Consequently, the sensitivity of Q to model width is the same at all K values.

Mean age of discharge to the valley of interest ($\bar{A}$) is also controlled largely by K and increases linearly with $1/K$ [Figure 4.14b]. The value of K does influence how long the water takes to move through the system, causing this trend in mean age. But, as above, the value of K does not actually change the flow pattern at any particular model width. Therefore, the sensitivity of $\bar{A}$ to model width is the same over the range of K values. While $\bar{A}$ is essentially linear with $1/K$, it should be noted that linearity can be affected by portions of the domain where diffusion dominates, especially deep in the aquifer and near stagnation zones. As long as K is greater than 10^{-10} m/s, however, this influence is negligible (see right side of Figure 4.14b). Overall, the age results indicate the same effect of model width as the previous section: the wider models (Ext1, Ext2) provide the best estimate whereas Trad and the asymmetric model widths overestimate age, due to the "trapping" of older, longer flow paths.

Since the value of K does not influence the overall flow pattern, the location of the groundwater divides does not change with variations in K [Figure

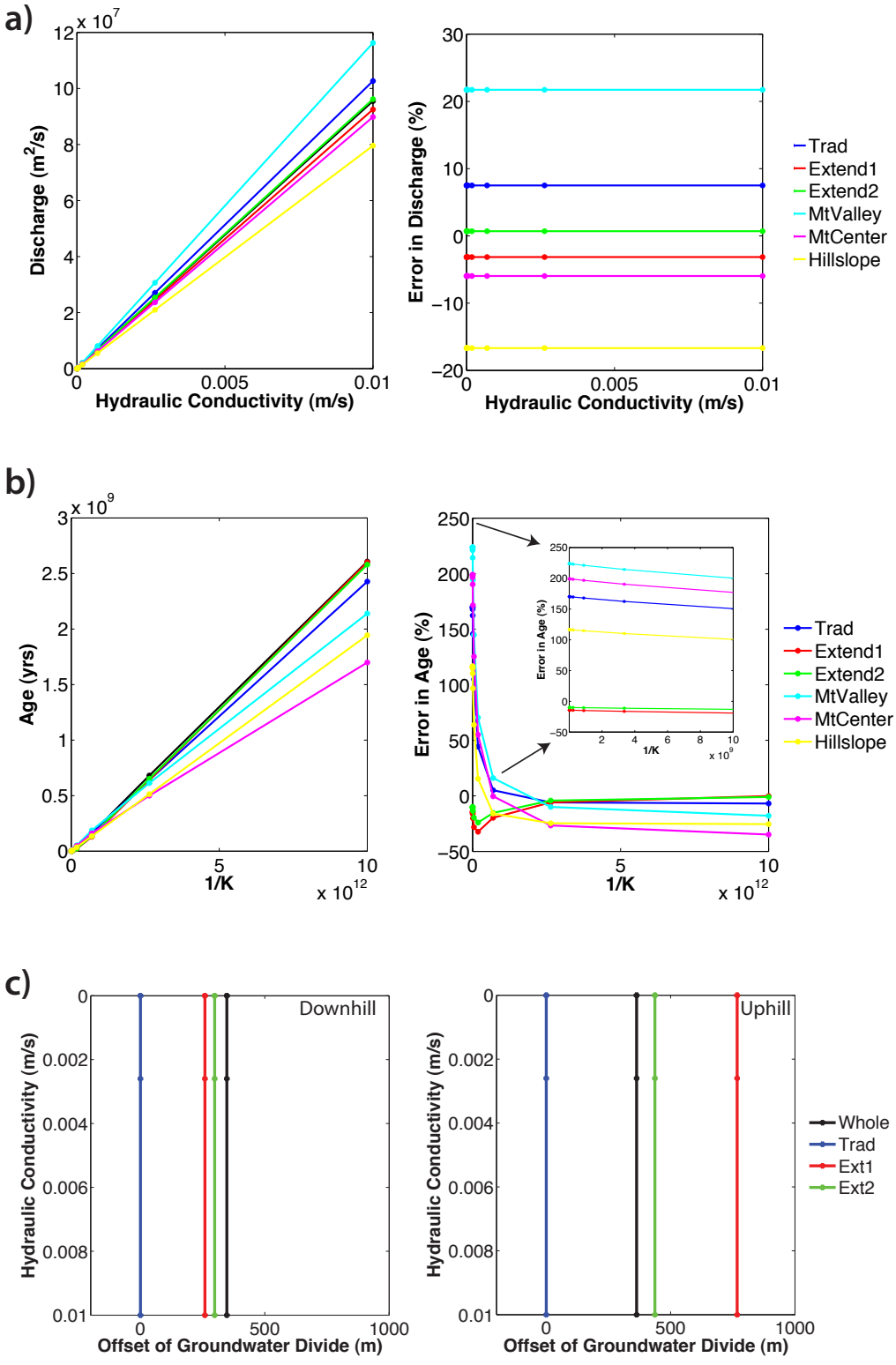

Figure 4.14: Sensitivity of metrics to hydraulic conductivity.

4.14c]. However, the choice of model width does greatly affect the position of the groundwater divides. Ideally, the groundwater divides of a model should fall close to the groundwater divide of the regional model as this would indicate that it is representing the regional flow system accurately even though it is smaller and truncated. According to this reasoning, both of the wider models (Ext1, Ext2) more closely approximate the actual groundwater divide than the Trad model does. However, Ext2 performs better at the uphill groundwater divide.

Sensitivity to Permeability Decay with Depth The choice of model width is less important when K decays with depth, since discharge is more sensitive to changes in the decay depth (d_D) [Figure 4.15a]. Note that the d_D values shown were calculated from a range of depth decay constants (β) according to Equation 4.11. All model widths except the smaller asymmetric ones (MtCenter, Hillslope) produce similar discharge results until d_D approaches 2000 m. At this point, the traditional (Trad) and MtValley model widths slightly overestimate discharge. However, this error is very small, indicating that any of the model widths, excluding MtCenter and Hillslope, are appropriate in scenarios with exponentially decaying permeability. Though not shown here, it should be noted that even in simulations with different permeability depth curves, Q is still directly related to the value of K. That is, the order of magnitude of Q for all simulated d_D values varies directly with the order of magnitude of K_o, the initial near-surface hydraulic conductivity. Similarly, $\bar{A}$ varies directly with $1/K_o$ (also not shown).

Mean age ($\bar{A}$) responds differently than discharge in that it decreases, rather than increases with a deeper d_D [Figure 4.15b]. Although the hydraulic conductivity does decay exponentially with depth in these cases, it never reaches zero.

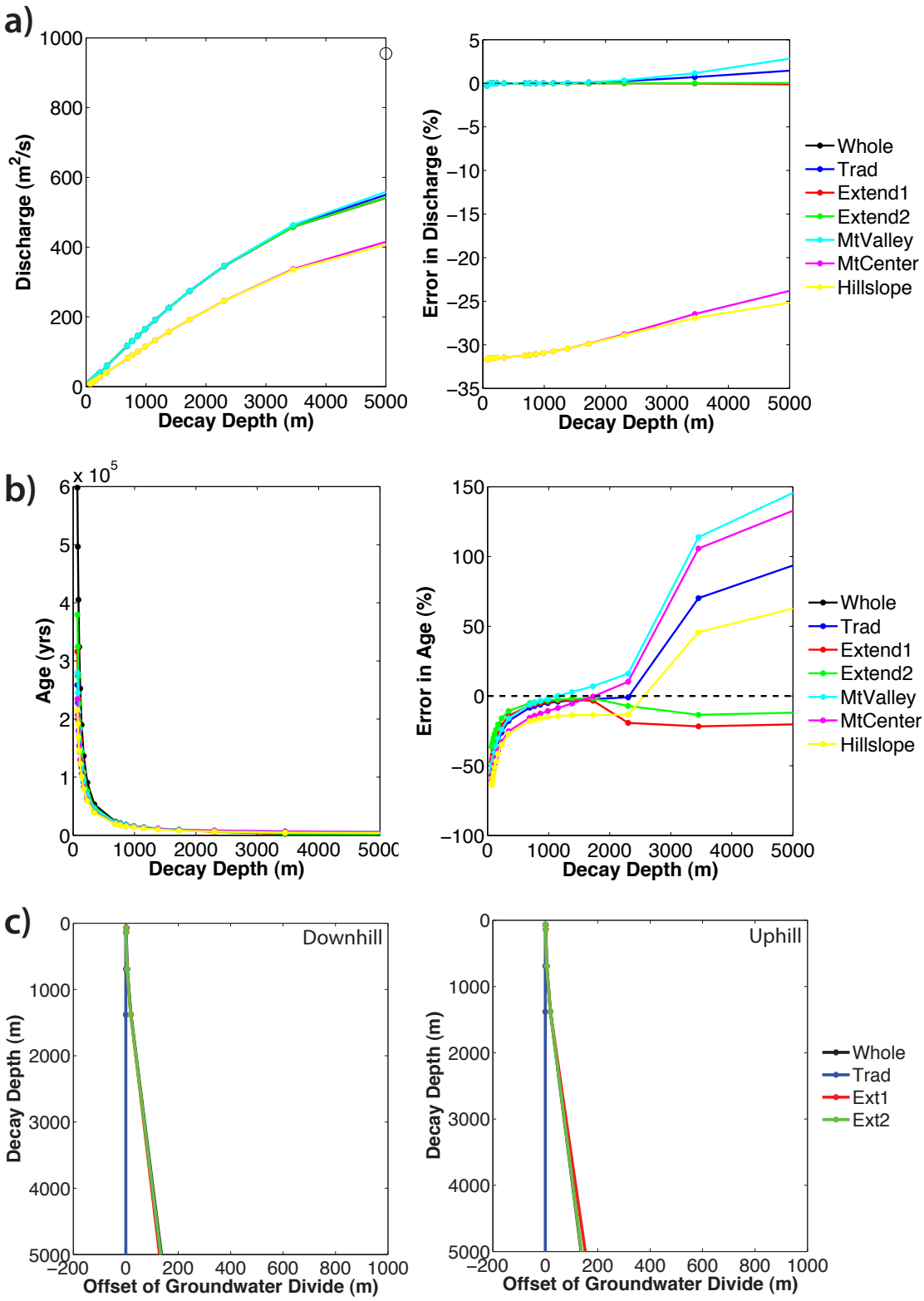

Figure 4.15: Sensitivity of metrics to decay depth (d_D).

Therefore, there is still some flow at all depths. It simply gets slower and slower as the hydraulic conductivity decreases. At deeper d_D values, then, more of the domain has as higher hydraulic conductivity, which leads to faster flow and a younger $\bar{A}$ value [Figure 4.16]. As d_D becomes shallower, more of the domain has a very low hydraulic conductivity which slows the flow, leading to much higher ages. All model widths underestimated age until the same threshold point as discharge: where d_D approaches 2000 m. Here, the smaller widths (Trad, MtValley, MtCenter, Hillslope) overestimate age. This is due to the "trapping" of the much older, deeper flowpaths that are forced to discharge in the valley of interest, biasing discharge towards older ages. The wider models (Ext1, Ext2) provide a better estimate at all decay depths, although only slightly at shallow ones.

At shallow d_D values, the location of the groundwater divide is not sensitive to changes in d_D nor choice of model width, but rather, remains at approximately the same position as the surface-water divide [Figure 4.15c]. This represents the compartmentalization of flow mentioned earlier, indicating that the system is dominated by local flow only. However, once d_D reaches approximately 500 m, the divide begins to move upslope. In this case, the wider models (Ext1, Ext2) are better at representing the actual groundwater divide than the Trad model width.

It should be noted that in many natural systems, the rate of permeability decay with depth is likely to be high, producing the shallow d_D values where the groundwater divide can be approximated by the surface-water divide. In this situation, the influence of regional topography would likely decrease as the flow becomes compartmentalized and the location of the groundwater divide would rely on the local topography only. The Trad model width would be sufficient,

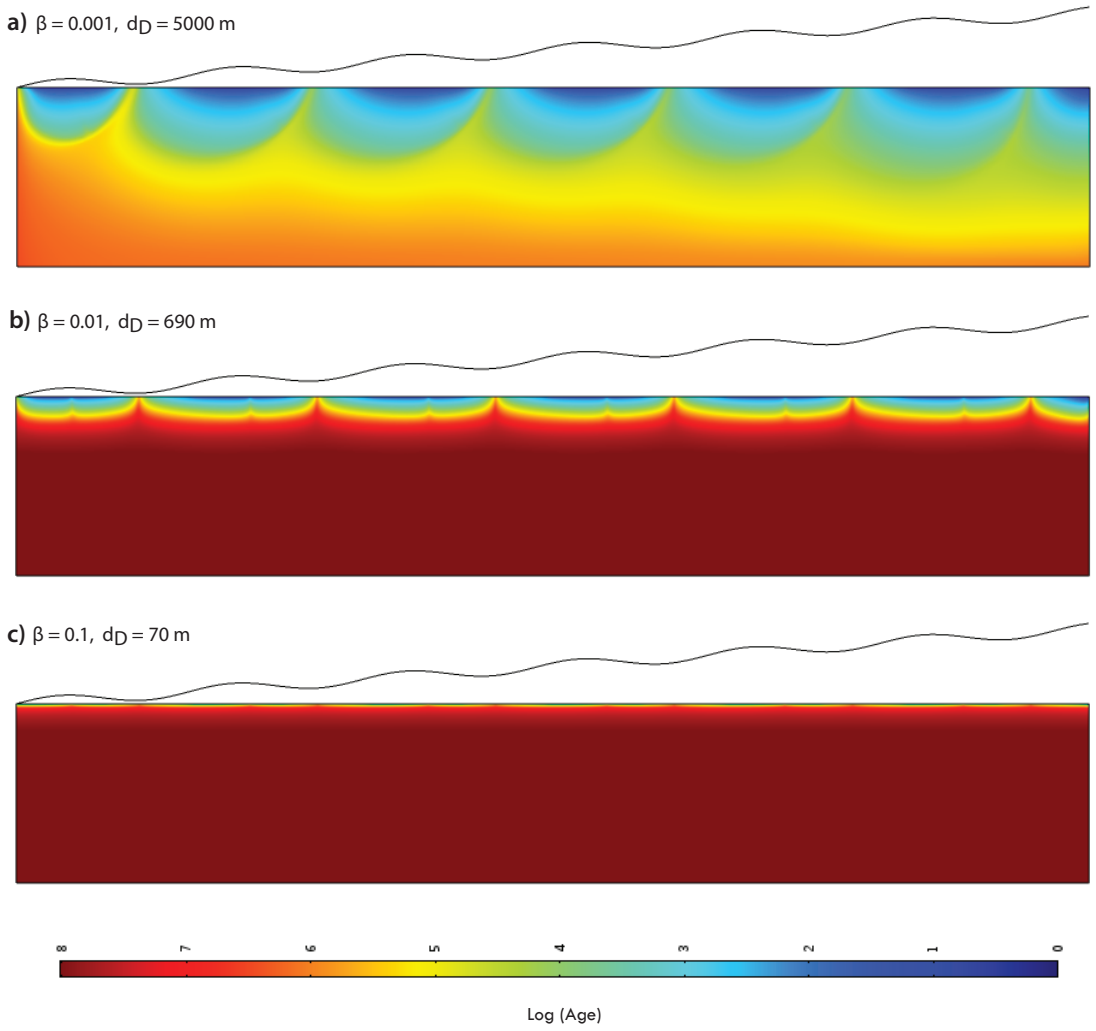

Figure 4.16: Effect of decay depth on age. The color scale represents age in years on a logarithmic scale.

and even recommended, because it uses less computational resources. However, in many other cases, the rate of decay is not actually well known. In that case, if there is a possibility that the d_D of the system is deeper than 500 m, then the wider model widths (Ext1, Ext2) would be more appropriate. The asymmetric models were not even evaluated for groundwater divide location as the smallest ones (MtCenter, Hillslope) provided such poor Q estimates, and MtValley did not appear to offer any advantage over traditional model width.

Sensitivity to Topography Discharge is sensitive to changes in topography, as it increases linearly with local hummock amplitude [Figure 4.17a] and slightly, though not linearly with slope [Figure 4.18a]. In both cases, the choice of model width does matter. At low hummock amplitudes ($<$ 150 m), the smaller model widths (Trad, MtValley, MtCenter, Hillslope) overestimate discharge, but with higher hummock amplitudes, the Trad model does not perform badly. MtValley also improves at higher amplitudes but doesn't offer any advantage over Trad. As amplitude increases, flow becomes more compartmentalized. In these scenarios, few flow paths that originate beyond the local watershed will discharge to the valley of interest and few flow paths will leave the watershed. This results in most model widths providing the same Q value. At amplitudes above 150 m, only the asymmetric MtCenter and Hillslope differ and they underestimate discharge. Since flow is compartmentalized, this underestimate is caused simply by the lower surface area and thus recharge, available to the valley of interest in these asymmetric cases. As slope increases, it is more likely that flow paths originating in our watershed will discharge downslope and thus outside of the valley of interest. The larger models (Ext1, Ext2, Whole) account for this loss and give

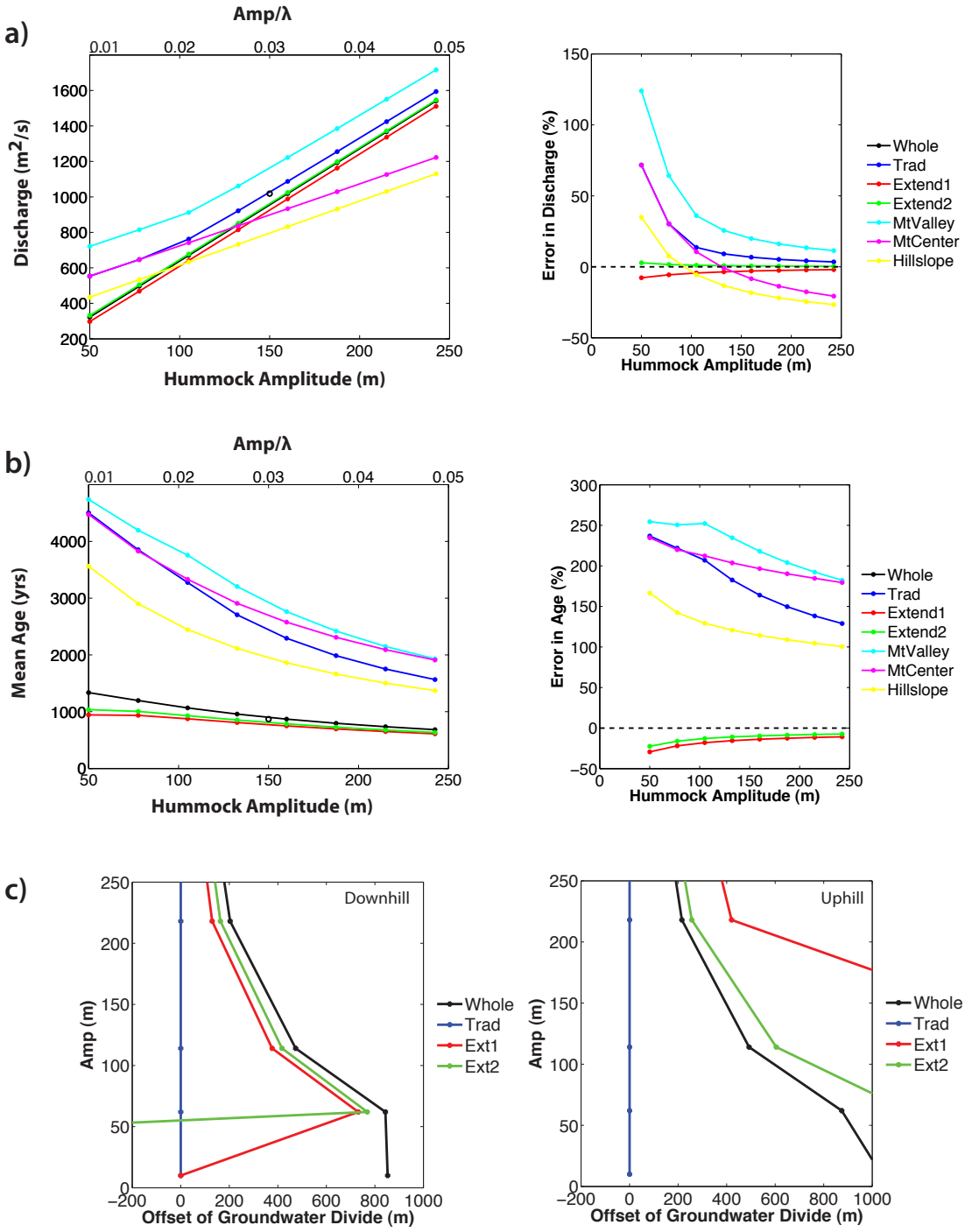

Figure 4.17: Sensitivity of metrics to hummock amplitude.

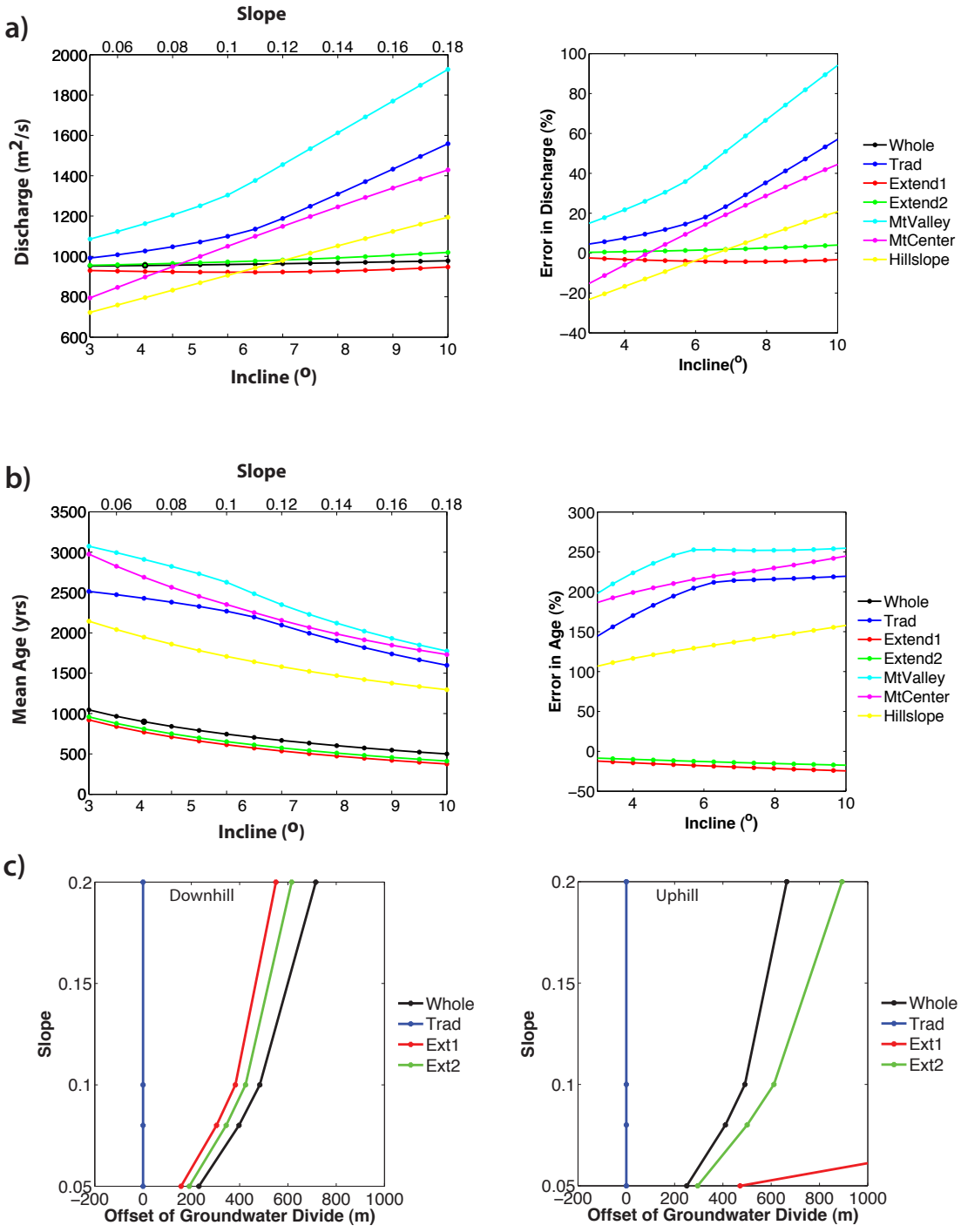

Figure 4.18: Sensitivity of metrics to regional slope.

similar Q values at all slope values. The smaller model widths (Trad, MtValley, MtCenter, Hillslope) do not account for this loss and instead "trap" this flow and force it to discharge to the valley of interest. This leads to an overestimate of Q. In these cases, extending the model width beyond the traditional watershed (Trad) is recommended.

In general, the mean age ($\bar{A}$) results are influenced by the same factors influencing the discharge results. At higher amplitudes, the flow becomes compartmentalized and few longer, older flow paths originating outside the watershed actually discharge to our valley of interest. This leads to a decline in mean age. At higher slopes, the long residence flowpaths are lost downslope or bypass our watershed altogether, also causing mean age to decrease. In all topographically-varying scenarios, the smaller model widths (Trad, MtCenter, MtValley, Hillslope) overestimate $\bar{A}$ significantly [Figures 4.17b and 4.18b]. This is caused by the same "trapping" effect discussed earlier. The wider models (Ext1, Ext2) are clearly better choices for calculating $\bar{A}$. Therefore, in all topographically-varying conditions, the model widths larger than the traditional model (Ext1, Ext2) are recommended.

When slope is increased, the groundwater divide moves uphill [Figure 4.18c]. At very low slopes, where flow is amplitude-dominated and compartmentalized, the groundwater divide occurs closer to the surface-water divide. At high slopes, the system becomes more regionally dominated, so the local flow cell is less well-defined and the groundwater divide moves uphill away from the surface-water divide. As amplitude increases, the flow system becomes more compartmentalized, moving the groundwater divide closer to the surface-water divide [Figure 4.17c]. However, even at very high amplitudes, where the flow is

compartmentalized and dominated by local flow, the groundwater divide is not necessarily co-located with the surface-water divide. At all amplitude and slope values, the wider model widths (Ext1, Ext2) are better at reproducing the actual groundwater divide than the Trad model. Ext2 generally performs better than Ext1, especially with variations in slope.

Sensitivity to Heterogeneity Discharge to the valley of interest increases as the dip angle of geologic layers increases, with little variation between model widths at each dip angle [Figure 4.19a]. That is, Q is more sensitive to the dip angle than to the model width in these simulations. This is likely because steeply dipping layers encourage compartmentalization, thus determining when the system is dominated by local flow and less likely to lose flow downhill to the regional system. $\bar{A}$ on the other hand, is more sensitive to the width of the model than to the dip angle. All dip angles produce approximately the same mean age value, but the smaller model widths (Trad, Ext1) overestimate the age [Figure 4.19b]. This is due to the "trapping" effect that was seen in the small model widths earlier. Here, the problem is exacerbated since flow is restricted by the dipping layers of low permeability material as well as the lateral boundaries of the model. The largest model width (Ext2) is therefore recommended for both Q and $\bar{A}$ calculations. The groundwater divide location follows completely different patterns for the uphill and downhill divide [Figure 4.19c]. For the downhill section, the dip angle and model width greatly change the groundwater divide location. However, at the uphill end, where the watershed is bounded by a low-permeability layer, the dip angle and the model width does not change the location of the groundwater divide. This indicates that the groundwater divide is not determined solely by the dip angle. Rather, the strike direction and the location of each layer need to be taken into consideration as well.

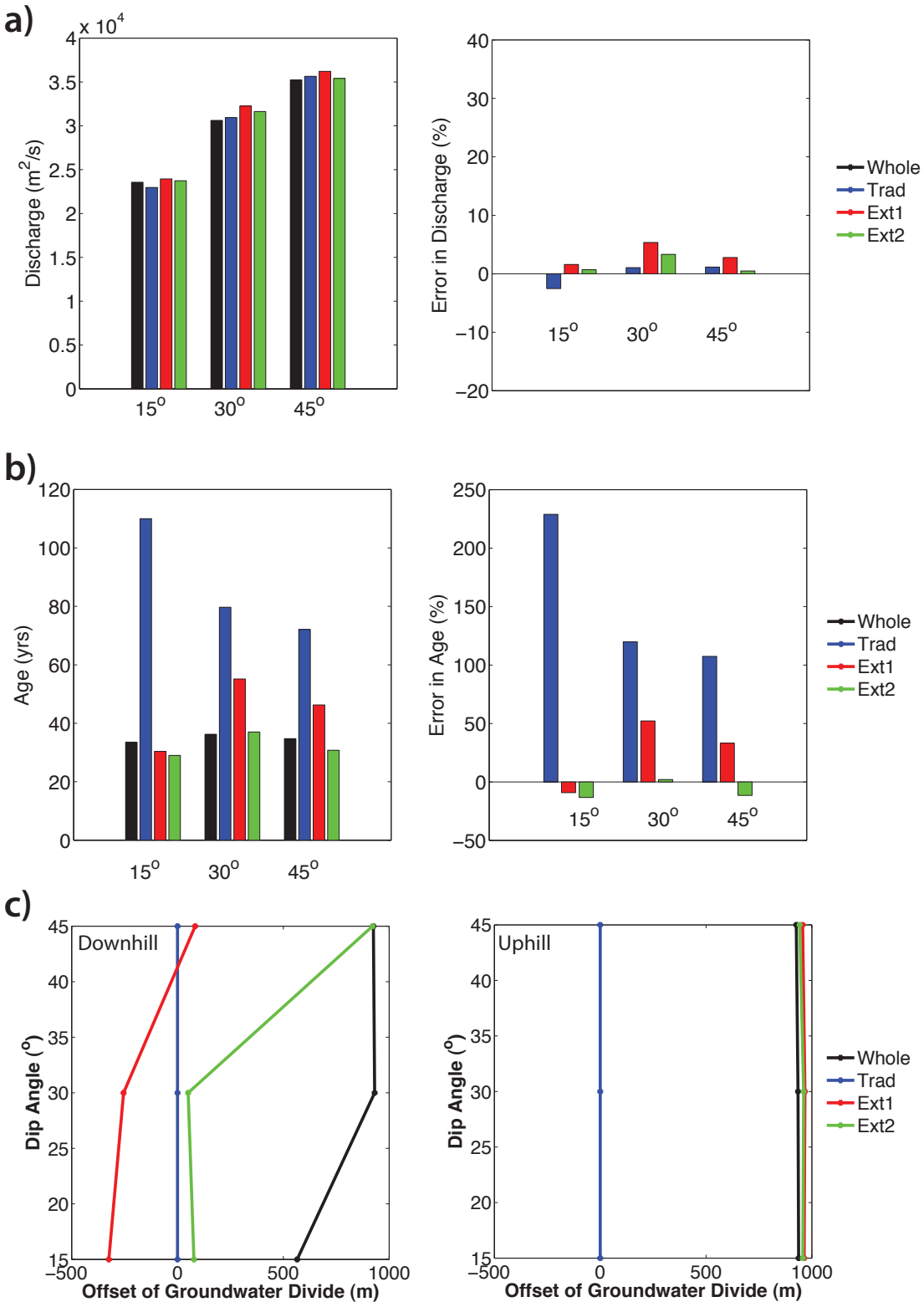

Figure 4.19: Sensitivity of metrics to heterogeneous layers at different dip angles.

Sensitivity to Anisotropy Changing the anisotropy ratio can have an effect similar to implementing a permeability depth-decay curve, since increasing K_h/K_v, while keeping K_h constant, effectively decreases the decay depth. In both cases, discharge decreases as the model stifles deeper flow at higher K_h/K_v values (comparable to shallow decay depths) [Figure 4.20a]. When $K_h/K_v = 1$, this simulation produces a similar Q value as the isotropic, homogeneous case in Figure 4.14a. Since the conditions at high K_h/K_v values and shallow decay depths discourage deeper flow, there is greater compartmentalization and so, local flow-dominated conditions. The wider models (Ext1, Ext2) provide the best estimates for discharge, followed by MtCenter and Trad. MtValley overestimates discharge and Hillslope underestimates discharge.

The mean age ($\bar{A}$), as usual, is most affected by the model width. At smaller model widths, $\bar{A}$ increases sharply with increasing K_h/K_v, while at larger model widths, $\bar{A}$ responds only slightly to changes in K_h/K_v [Figure 4.20b]. All model widths do, however, show at least some increase in the calculated $\bar{A}$ as K_h/K_v increases. This increase in $\bar{A}$ is similar to the increase with shallower decay depths seen earlier in Figure 4.15. In that system, very low permeability at depth slowed down flow, leading to older $\bar{A}$ values. In this system, flow is slowed down by low K_v (high K_h/K_v) values. Since flow to the bottom of the system and back up to the discharge point slows when K_h/K_v is high, the calculated $\bar{A}$ gets biased towards older ages [Figure 4.21]. The "trapping" effect, as before, exaggerates this age bias in the smaller model widths so that the wider models (Ext1,Ext2) again provide the best estimates for both Q and $\bar{A}$.

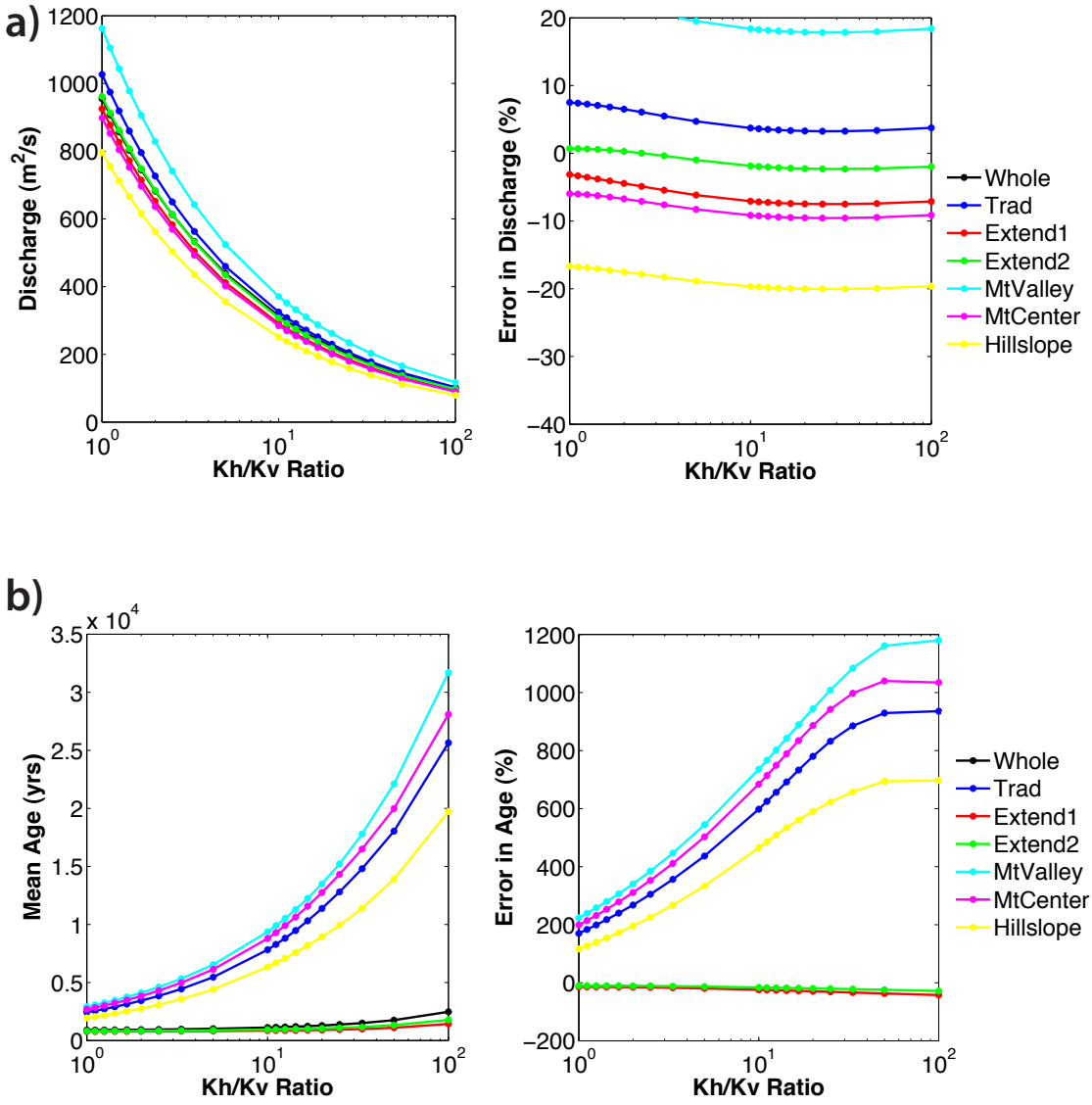

Figure 4.20: Sensitivity of metrics to anisotropy.

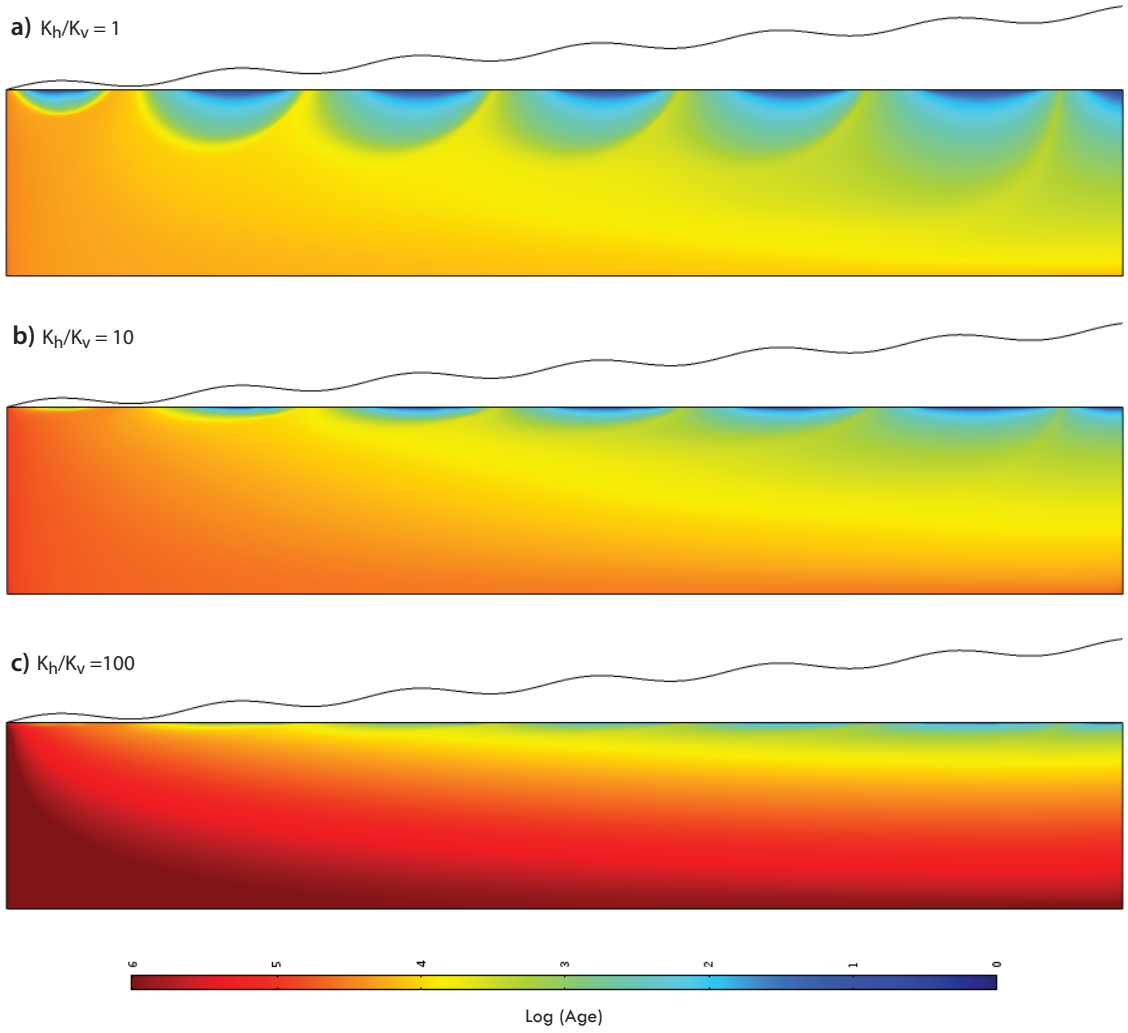

Figure 4.21: Effect of anisotropy on Age. The color scale represents the age in years on a logarithmic scale.

4.4 Conclusions

This modeling exercise has provided some objective guidelines for assigning model boundaries. Using model widths (Ext1, Ext2 for example) that are wider than the surface-water divide (Trad) is recommended in almost all scenarios. There are a few situtations when the Trad model width is acceptable, such as when hydraulic conductivity is expected to undergo significant exponential decay with depth. The Trad model width may also be acceptable in certain scenarios when discharge is the only metric of interest. At high amplitude values or very low regional slope values, for instance, the Trad model provides an acceptable Q value even though it severely overestimates $\bar{A}$. But in general, larger model widths consistently produce Q and $\bar{A}$ values as well as groundwater divide locations that are more representative of the regional flow system across a natural spectrum of environmental and physical parameter values. Choosing asymmetric model widths is not recommended as they do not appear to offer any advantage over using a traditional (Trad) model width. In fact, picking a smaller asymmetric model width (MtCenter, Hillslope for instance) can lead to significant errors in Q and $\bar{A}$.

If the actual thickness of the model is unknown, there are some objective methods for picking an appropriate model thickness. Our results indicate the existence of a threshold model thickness at which the calculated values for Q and A as well as the groundwater divide locations stop changing. This indicates that the model could be truncated to this thickness without compromising the validity of the Q and $\bar{A}$ values calculated for our valley of interest. In our base-case, this optimal model thickness is between 2000-3000 m, but could easily be calculated for other environmental conditions. If a permeability decay depth curve or

anisotropy ratio has been defined in an area of interest, these can also be used to choose an appropriate model thickness. In this scenario, magnitude-controlled streamlines can define the ideal thickness at which the model will capture the desired percentage of flow in the entire system.

The results of this modeling exercise challenge the following assumptions commonly made in hydrologic modeling:

1) The groundwater divide can be defined as the surface-water divide. As shown in Figure 4.3 and throughout this work, the groundwater divide is not always co-located with the surface-water divide, even in a model, like this one, where the groundwater is assumed to be a subdued replica of the surface topography.

2) The highest point of the water-table is the groundwater divide. Because of the fundamental difference between idealized surface-water flow (flows by gravity down a surface) and groundwater flow (flows by gravity and aquifer forcings through a permeable media as part of a larger connected groundwater system), the highest point of the groundwater table is not necessarily the groundwater divide. Though highly non-intuitive, this observation is demonstrated in Figure 4.3.

3) Setting model boundaries at estimated natural boundaries is appropriate. All model boundaries are somewhat arbitrary, so it may seem more objective to pick model boundaries at natural features like the groundwater high or a geologic layer of lower permeability. However, as mentioned in the previous point, something that seems like a reasonable natural boundary, such as the groundwater high, may not necessarily be an appropriate lateral boundary. In addition, placing

no-flow lateral boundaries too close to the valley of interest, as tends to happen when using so-called natural boundaries, can cause an unnatural increase in mean age estimates due to the "trapping" effect. This is a particuar problem when the model is solved to steady state and model thickness is deep.

4) If a model simulates discharge correctly, it also simulates age correctly. As shown in Figures 4.17, 4.18, 4.20, and 4.19, changing physical parameters like permeability, topography, anisotropy, and heterogeneity will affect discharge and mean age results very differently. Therefore, in many scenarios, it is feasible that a model calibrated correctly to field discharge measurements will not correctly reproduce field age measurements. However, the opposite does appear to be true. That is, if a model simulates groundwater age correctly, it also simulates discharge correctly. This has significant implications for choosing which metric to use for the calibration and testing of watershed models.

4.5 Future Work

The Tóth model is a convenient conceptual model to use, as it is widely accepted and easy to manipulate. However, there are several drawbacks to using a Tóth-like model, as we did in this modeling exercise. It is 2D, making it difficult to properly determine behavior of a fully 3D system as necessary for a coupled surface/groundwater watershed model. To better represent this type of system, the same modeling exercise could be carried out on a 3D representation of the Tóth model, as in Gleeson and Manning (2008). A known head boundary at the top is also not necessarily appropriate for representing real watersheds since,

especially in mountainous areas, the water-table is not usually well-known. A known recharge boundary might be a better choice, as recharge relies on precipitation, an input that is usually available for most field areas. In addition, many surface/shallow-subsurface models like PRMS produce recharge as an output. Being able to vary recharge allows testing of climate change scenarios in which precipitation and thus recharge would change over time. It would also provide the opportunity to address spatially varying recharge due to elevation, aspect, soil cover, and vegetation. Another shortcoming of this model is that the topography of the top sinusoidal head boundary is extremely simplistic and unlikely to represent realistic topography. Subdued replicas of actual elevation profiles from a watershed of interest could therefore be applied as the known head or known recharge boundary.

Even without changing the conceptual model at all, there still may be more information to be gained from this model. For instance, mean age may not have been the most appropriate metric for evaluating these models. Gomez and Wilson (2012) suggests that mean age ($\bar{A}$) is a poor metric for accurately assessing groundwater age since it is weighted towards the "heavy tail" of much older groundwater. This would explain the very high mean age values we calculated, particularly in the small model-width scenarios. Instead, the mode of an age distribution is likely closer to the mix of ages represented by the results of a tracer dating technique. In this case, we could analyze the same Tóth-like model for the metric of age distribution in our valley of interest. This could give a better representation of groundwater flow and residence time in our area, as well as provide a metric that is more readily comparable to field measurements.

CHAPTER 5

CONCLUSIONS AND RECOMMENDATIONS

While not able to quantitatively establish how much influence mountain block recharge exerts on the basin hydrogeology, the results of our isotopic and major ion characterization effort do indicate that mountain block recharge does contribute to the basin aquifer and to surface flows. The effect of these deep flow paths appears in deep mountain front wells, which our sampling indicates are a mixture of precipitation and groundwater orginating within the mountain block. There is also a direct relationship between major ion composition in the river and the size of the contributing drainage area which could indicate that long, deep flowpaths, like those from deep percolation in the mountain block, discharge to the Rio Hondo as it flows through the mountain-front basin. A similar enrichment trend was observed in a watershed in the San Juan Mountains of southern Colorado (Frisbee, 2010). There the trend was thought to support a 3D catchment-mixing conceptual model which incorporates longer regional flow paths, rather than just surface and shallow subsurface flow. If the enrichment in the Rio Hondo is due to the same processes, then this work could provide another case study supporting this conceptual model. In addition, it shows that deep mountain block groundwater is important not only in a large, pristine watershed of permeable volcanics but also in a smaller, developed watershed of crystalline geology.

Since geochemical sampling results suggest that long residence-time flowpaths have a significant influence on both groundwater and surface-water in the Rio Hondo area, the proposed 4D coupled groundwater/surface-water model of the Rio Hondo should be made thick enough to incorporate potential deep flowpaths in the mountain block. There are no field measurements available to establish a permeability depth-decay curve for the area, so we cannot pick an appropriate model thickness by simply determining, based on magnitude-controlled streamlines, the model thickness that would capture the majority of flow. Rather, we suggest extending the model as close as is computationally feasible to an "optimal model thickness' ' value calculated with the same method discussed in Section 4.3.1.

Since the permeability of geologic formations in the Rio Hondo mountain block are dominated by secondary fracturing, there is potential for cross-basin flow. Therefore, the proposed model also needs to be wide enough to accurately represent any potential subsurface flow between surface watersheds. Our modeling exercise tried to find an ideal model width by testing the six different model widths described in Figure 4.4 and 4.5. The results indicated that wider models (like Ext1, Ext2) are preferable to the traditional model width, especially for correctly representing mean age in a valley of interest. One of the main reasons for constructing the hydrogeologic model of the Rio Hondo is to study the potential impacts of climate change. Therefore, mean age is a very important model output since knowing age can help indicate the source, deep or shallow, of water in the basin and indicate the resilience of the system to climate change. Ideally, then, the model width would be similar to Ext2 that produces the most reliable mean age ($\bar{A}$) values in most scenarios. This model width would stretch to the peaks on the

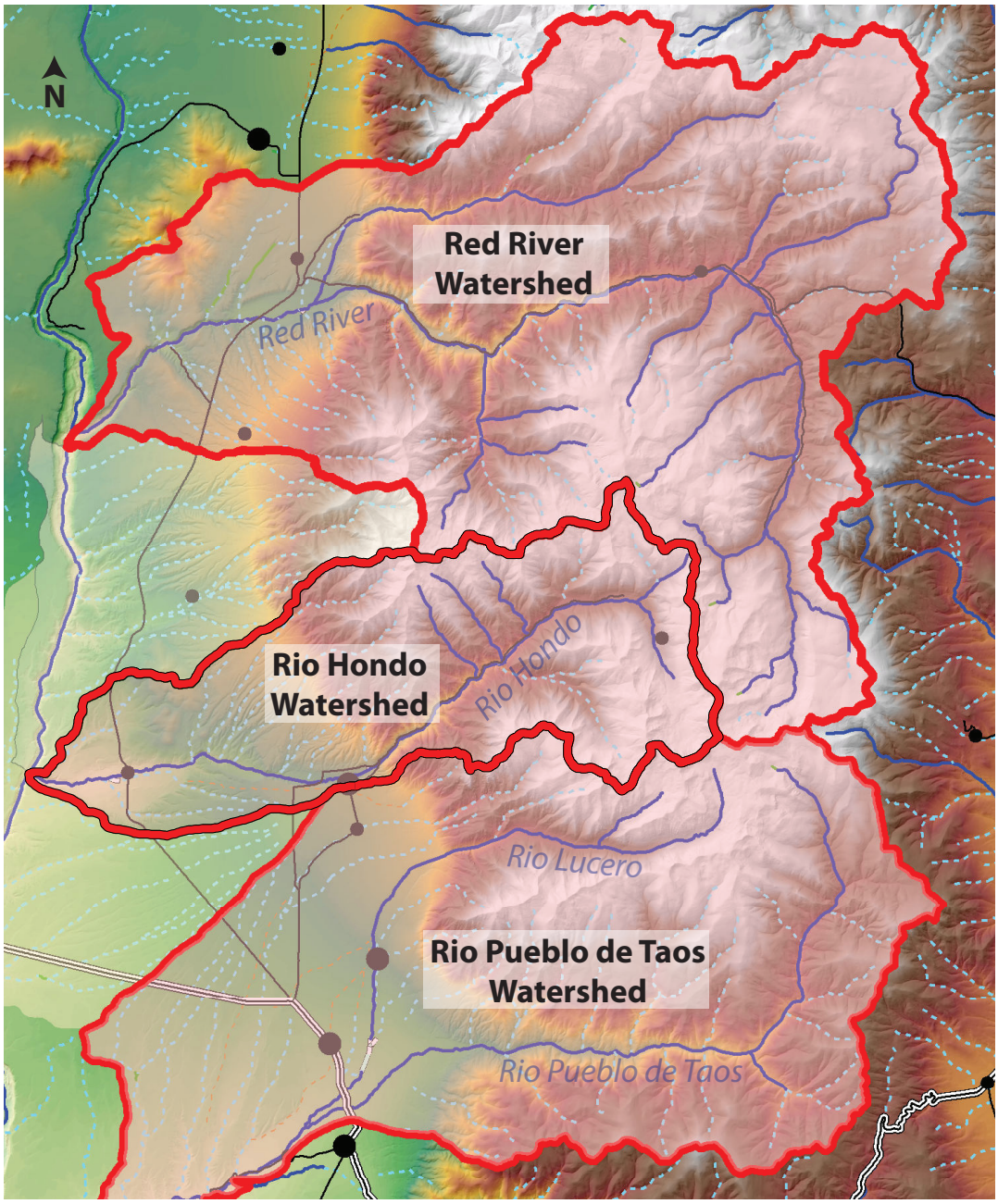

Figure 5.1: Potential extended model boundary for the Rio Hondo watershed.

far side of Red River watershed to the north and the Rio Pueblo de Taos watershed to the south [Figure 5.1]. However, extending the model boundaries this far may be computationally infeasible, especially for a 3D model. In addition, while the area to the south of the Rio Hondo watershed has similar geology, the geologic setting of the Red River watershed is very different and complicated, including a fractured caldera wall as well as extensive mining operations. Therefore, it is more appropriate to recommend a compromise and choose a model width more similar to Ext1. This would extend the boundaries from the river valley of Red River to the river valley of Rio Lucero, sandwiching the Rio Hondo watershed in between. The computational resources required for this would be much less, but would still, according to our modeling exercise, produce reliable discharge (Q) and $\bar{A}$ values. The width of the model would also still be sufficiently large to account for cross-basin flow, should any be occuring in this area.

REFERENCES

Anderholm, S. (2001). Mountain-front recharge along the eastern side of the Middle Rio Grande Basin, Central New Mexico. Water-Resources Investigation Report 00-4010, US Geological Survey.

Anderson, M. and McDonnell, J., editors (2008). *Groudwater: Benchmark Papers in Hydrology*, volume 3 of *IAHS Benchmark Papers in Hydrology*. International Association of Hydrological Sciences, Oxfordshire, UK.

Araguás-Araguás, L., Rozanski, K., Gonfiantini, R., and Louvat, D. (1995). Isotope effects accompanying vacuum extraction of soil water for stable istope analyses. *Journal of Hydrology*, 168:159–171.

Barnes, C. and Allison, G. (1988). Tracing of water movement in the unsaturated zone using stable isotopes of hydrogen and oxygen. *Journal of Hydrology*, 100:143–176.

Barroll, P., Burck, P., Drakos, P., Lazarus, J., Chudnoff, M., et al. (2006). Documentation of OSE Taos area calibrated groundwater flow model T17. 0. *Santa Fe, NM, New Mexico Office of the State Engineer*.

Bauer, P., Johnson, P., and Kelson, K. (1999). Geology and hydrogeology of the southern Taos Valley, Taos County. Technical report, New Mexico: Final Technical Report, Office of the State Engineer.

Bear, J. (1972). *Dynamics of Fluids in Porous Media.* American Elsevier Publishing Company.

Belitz, K. and Bredehoeft, J. (1988). Hydrodynamics of the Denver Basin: Explanation of subnormal fluid pressure. *American Association of Petroleum Geologists' Bulletin*, 72:1334–1359.

Beven, K. and Kirkby, M. (1979). A physically based variable contributing area model of catchment hydrology. *Hydrological Sciences Bulletin*, 24:43–69.

Boutt, D., Diggins, P., and Mabee, S. (2010). A field study (Massachusetts, USA) of the factors controlling the depth of groundwater flow systems in crystalline fractured-rock terrain. *Hydrogeology Journal*, 18:1839–1854.

Brace, W. (1984). Permeability of crystalline rocks: New in situ measurements. *Journal of Geophysical Research*, 89:4327–4330.

Bricker, O. and Jones, B. (1995). Main factors affecting the composition of natural waters. In Salbu, B. and Steinnes, E., editors, *Trace Elements in Natural Waters*. CRC Press, Boca Raton, FL.

Burnash, R., Ferral, R., and McGuire, R. (1973). A generalized streamflow simulation system: Conceptual modeling for digital computers. Technical report, US Department of Commerce, National Weather Service in cooperation with California Department of Water Resources, Sacramento, CA.

Campbell, A., Hendrickx, J., and Lynn, R. (2008). Rock pile weathering stability : Final report on the stable isotopic composition of precipitation and soil samples at the Questa Mine. Technical report, Molycorp Project Managers and Weathering Stability Team, Questa, NM.

Cayan, D., Kammerdiener, S., Dettinger, M., Caprio, J., and Peterson, D. (2001). Changes in the onset of spring in the western United States. *bulletin of the American Meteorological Society*, 82(3):399–415.

Clarke, B. and Burbank, D. (2011). Quantifying bedrock-fracture patterns within the shallow subsurface: Implications for rock mass strength, bedrock landslides, and erodibility. *Journal of Geophysical Research*, 116.

Craig, H. (1963). The isotopic geochemistry of water and carbon in geothermal areas. In Tongiorgi, E., editor, *Nuclear geology in geothermal areas*, pages 17–53. Consiglio Nazionale della Ricerche, Laboratorio de Geologia Nucleare, Pisa, Italy.

Daniel B. Stephens & Associates, I. (2008). Taos regional water plan. Technical report, Taos Regional Water Planning Steering Committee.

Davis, S. (1964). Silica in streams and ground water. *American Journal of Science*, 262:870–891.

Davis, S., Whittemore, D., and Fabryka-Martin, J. (1998). Use of chloride/bromide ratios in studies of potable water. *Ground water*, 36(2):338–350.

Drakos, P., Jay, L., Bill, W., Banet, C., Jim, R., and Sandoval, J. (2004). Hydrologic characteristics of basin-fill aquifers in the southern San Luis Basin, New Mexico. In *Geology of the Taos Region: New Mexico Geological Society, Fifty-fifth Annual Field Conference, September 22-25, 2004*, volume 55, page 391. New Mexico Geological Society.

Drever, J. (1997). *The Geochemistry of Natural Waters:*. Prentice-Hall, Inc., Upper Saddle River, NJ, 3rd edition.

Earman, S. (2004). *Groundwater recharge and movement through mountain-basin systems of the Southwest: A case study in the Chiricahua Mountains-San Bernadino Valley System Arizona and Sonora*. PhD thesis, New Mexico Institute of Mining and Technology, Socorro, NM.

Earman, S., Campbell, A., Phillips, F., and Newman, B. (2006). Isotopic exchange between snow and atmospheric water vapor: Estimation of the snowmelt component of groundwater recharge in the southwestern United States. *Journal of geophysical research*, 111(D9):D09302.

Flint, A., Flint, L., Hevesi, J., D'Agnese, F., and Faunt, C. (2000). Estimation of regional recharge and travel time through the unsaturated zone in arid climates. In Faybishenko, B., Witherspoon, P., and Benson, S., editors, *Dynamics of fluids in fractured rock*, number 122 in Monograph Series, pages 115–128. American Geophysical Union.

Freeze, R. and Cherry, J. (1979). *Groundwater*. Prentice-Hall, Inc., Englewood Cliffs, NJ.

Freeze, R. and Witherspoon, P. (1967). Theoretical analysis of of regional groundwater flow: 2. Effect of water-table configuration and subsurface permeability variation. *Water Resources Research*, 3:623–634.

Frisbee, M. (2010). *Streamflow Generation Processes and Residence Times in a Large, Mountainous Watershed in the Southern Rocky Mountains of Colorado, USA*. PhD thesis, New Mexico Institute of Mining and Technology, Socorro, NM.

Frisbee, M., Phillips, F., Campbell, A., Liu, F., and Sanchez, S. (2011). Streamflow generation in a large, alpine watershed in the southern Rocky Mountains of Colorado: Is streamflow generation simply the aggregation of hillslope runoff processes? *Water Resources Research*, 47.

Garrabrant, L. (1993). Water resources of Taos County. *New Mexico: US Geological Survey Water-Resources Investigations Report*, pages 93–4107.

Genereux, D., Wood, S., and Pringle, C. (2002). Chemical tracing of interbasin grondwater transfer in the lowland rainforest of Costa Rica. *Journal of Hydrology*, 258:163–178.

Gleeson, T. and Manning, A. (2008). Regional groundwater flow in mountainous terrain: Three-dimensional simulations of topographic and hydrogeologic controls. *Water Resources Research*, 44.

G.N. Green, G. J. (1997). The digital geologic map of New Mexico 1:500,000 scale in ArcINFO format. Technical Report OF-97-0052, USGS, Denver, CO.

Golder Associates, I. (2009). Final consultancy report for the El Salto Mutual Domestic Water Consumers Association re: Submittal of findings and recommendations for public water supply well locations and completions. Technical report, Golder Associates, Inc.

Goldich, S. (1938). A study in rock-weathering. *Journal of Geology*, 46:17–58.

Gomez, J. and Wilson, J. (2012). Age distributions and dynamically changing hydrologic systems: Exploring topography-driven flow. In Review.

Goode, D. (1996). Direct simulation of groundwater age. *Water Resources Research*, 32(2):289–296.

Grauch, V., Bauer, P., and Kelson, K. (2004). Preliminary interpretation of high resolution aeromagnetic data collected near Taos, New Mexico. In Brister, B., Bauer, P. W., Read, A. S., and Lueth, V., editors, *New Mexico Geological Society Guidebook, 55th Fall Field Conference*, volume 55, pages 244–256. NMBGMR.

Guan, H. (2005). *Water above the mountain front: Assessing mountain-block recharge in semiarid mountainous regions*. PhD thesis, New Mexico Institute of Mining and Technology, Socorro, NM.

Haitjema, H. and Mitchell-Bruker, S. (2005). Are water tables a subdued replica of the topography? *Ground water*, 43(6):781–786.

Hearne, G. and Dewey, J. (1988). Hydrologic analysis of the Rio Grande Basin north of Embudo, New Mexico; Colorado, and New Mexico. Water-Resources Investigation Report 86-4113, USGS, Denver, CO.

Holzbecher, E. (2001). The dynamics of subsurface water divides: Watersheds of Lake Stechlin and neighboring lakes. *Hydrological Processes*, 15:2297–2304.

Hooper, R. and Shoemaker, C. (1986). A comparison of chemical and isotopic hydrograph separation. *Water Resources Research*, 22:1444–1454.

Hubbert, M. (1940). The theory of groundwater motion. *Journal of Geology*, 48(8):785–944.

Huntley, D. (1979). Ground-water recharge to the aquifers of northern San Luis Valley, Colorado. *Geological Society of America Bulletin, Part I*, 90:707–709.

Ingebritsen, S. and Sanford, W. (1998). *Groundwater in Geologic Processes*. Cambridge University Press, New York, NY.

Ivanov, V., Vivoni, E., Bras, R., and Entekhabi, D. (2004). Catchment hydrologic response with a fully-distributed triangulated irregular network model. *Water Resources Research*, 40(11).

Johnson, P. (1999). Availability and variability of surface-water resources in Taos County, New Mexico—an assessment for regional planning. *New Mexico Geology*, 21(1):1–9.

Johnson, P., Bauer, P., and Felix, B. (2009). Hydrogeologic investigation of the Arroyo Hondo Area, Taos County, New Mexico. Open-File Report 505, New Mexico Bureau of Geology and Mineral Resources.

Johnson, P., Koning, D., and Partey, F. (2012). Shallow groundwater geochemistry in the Española Basin, Rio Grande Rift, New Mexico: Evidence for structural control of a deep thermal source. In *GSA special publication on Rio Grande Rift (pending)*. Geological Society of America.

Keen, K. (1992). *Geomorphology, recharge, and water-table fluctuations in stabilized sand dunes: The Nebraska Sand Hills USA*. PhD thesis, University of Minnesota.

Kelson, K., Bauer, P., Love, D., Connell, S., Mansell, M., and Rawling, G. (2004). Initial paleoseismic and hydrologic assessment of the southern Sangre de Cristo Fault at the Taos Pueblo site, Taos, New Mexico. Open-File Report 476, New Mexico Bureau of Geology and Mineral Resources, Socorro, NM.

Kennedy, V. (1971). Silica variation in stream water with time and discharge. In Hem, J., editor, *Nonequilibrium Systems in Natural Water Chemistry*, volume 106, chapter 4, pages 94–130. American Chemical Society.

Lasaga, A. (1984). Chemical kinetics of water-rock interactions. *Journal of Geophysical Research*, 89(B6):4009–4025.

Leavesley, G., Lichty, R., Troutman, B., and Saindon, L. (1983). Precipitation-runoff modeling system: User's manual. Water-Resources Investigation Report 83-4238, US Geological Survey.

Levitt, D. (2004). Simulation of net infiltration for present-day and potential future climates. Technical Report MDL-NBS-HS-000023, REV 00, Yucca Mountain Project, Las Vegas, NV.

Ludington, S., Plumlee, G., Caine, J., Bove, D., Holloway, J., and Livo, K. (2004). Questa baseline and pre-mining ground-water quality investigation, 10. *Geologic influences on ground and surface waters in the lower Red River watershed, New Mexico: US Geological Survey, Scientific Investigations Report*, 5245:46.

Mailloux, B., Person, M., Kelley, S., Dunbar, N., Cather, S., Strayer, L., and Hudleston, P. (1999). Tectonic controls on the hydrogeology of the Rio Grande Rift, New Mexico. *Water Resources Research*, 35(9):2641–2659.

Manning, A. (2002). *Using noble gas tracers to investigate mountain-block recharge to an intermountain basin*. PhD thesis, University of Utah, Salt Lake City, UT.

Manning, A. (2008). Ground-water temperature, noble gas, and carbon isotope data from the Española Basin, New Mexico. Scientific Investigations Report 2008-5200, USGS.

Manning, A. and Caine, J. (2007). Groundwater noble gas, age, and temperature signatures in an alpine watershed: Valuable tools in conceptual model development. *Water resources research*, 43(4):W04404.

Manning, A. and Solomon, D. (2003). Using noble gases to investigate mountain-front recharge. *Journal of Hydrology*, 275:194–207.

Manning, A. H. (2011). Mountain-block recharge, present and past, in the eastern Española Basin, New Mexico, USA. *Hydrogeology Journal*, 19:379–397.

Manning, C. and Ingebritsen, S. (1999). Permeability of the continental crust: the implications of geothermal and metamorphic systems. *Reviews of Geophysics*, 37:127–150.

Mansure, A. and Reiter, M. (1979). A vertical ground-water movement correction for heat flow. *Journal of Geophysical Research*, 84:3490–3496.

Markstrom, S., Niswonger, R., Regan, R., Prudic, D., and Barlow, P. (2008). Gsflow-coupled ground-water and surface-water flow model based on the integration of the Precipitation-Runoff Modeling System (PRMS) and the Modular Ground-water Flow Model (MODFLOW-2005). Techniques and Methods 6-D1, US Geological Survey.

McAda, D. and Wasiolek, M. (1988). Simulation of the regional geohydrology of the Tesuque aquifer system near Santa Fe, New Mexico. Water-Resources Investigation Report 87-4056, US Geological Survey.

McDonald, M. G. and Harbaugh, A. W. (1988). A modular three-dimensional finite-difference ground-water flow model. Techniques of Water-Resource Investigation 06-A1, US Geological Survey.

NADP (2012). National trends network. Available at `http://nadp.sws.uiuc.edu/ntn/` by the National Atmospheric Deposition Program (NADP).

Nimz, G. (1998). Lithogenic and cosmosgenic tracers in catchment hydrology. In Kendall, C. and McDonnell, J., editors, *Isotope Tracers in Catchment Hydrology*. Elsevier, Oxford, UK.

NMBGMR (2003). Geologic map of New Mexico. Available at `http://geoinfo.nmt.edu/publications/maps/geologic/state/home.cfm` by the New Mexico Bureau of Geology & Mineral Resources.

NMEID (1981). Point source waste load allocation for the Twining Water and Sanitation District, Taos County, NM. Technical report, NM Environmenal Improvement Division(NMEID), Santa Fe, NM.

NMOSE (2006a). Abeyta water rights adjudication: Taos Pueblo draft settlement agreement among the United States of America, Taos Pueblo, the State of New Mexico, the Taos Valley Acequia Association and its 55 member acequias, the Town of Taos, El Prado Water and Sanitation District, and the 12 Taos Area Mutual Domestic Water Consumers' Associations. Available at `http://www.ose.state.nm.us/PDF/Settlements/Taos/AbeytaSettlementAgreement-2006-03-31.pdf`.

NMOSE (2006b). The impact of climate change on New Mexico's water supply and ability to manage water resources. Technical report, New Mexico Office of the State Engineer/Interstate Stream Commission, Santa Fe, NM.

NMSWQB (2004a). Total maximum daily load (TMDL) for the Upper Rio Grande watershed (Pilar, NM to Colorado border). Technical report, NM Environment Department Surface Water Quality Bureau, Santa Fe, NM.

NMSWQB (2004b). Water quality survey summary for the Upper Rio Grande watershed, part I 2000. Technical report, NM Environment Department Surface Water Quality Bureau, Santa Fe, NM.

NMSWQB (2005). Total maximum daily load (TMDL) for the Rio Hondo (South Fork of Rio Hondo to Lake Fork Creek). Technical report, NM Environment Department Surface Water Quality Bureau, Santa Fe, NM.

OSU (2001). New Mexico average monthly and average annual precipitation (1971-2000). Available at `http://datagateway.nrcs.usda.gov/GDGOrder.aspx` by the Oregon Climate Service at Oregon State University.

Picarro (2012). What is CRDS? Available at:`http://www.picarro.com/technology/what_is_crds`.

Pinder, G. and Jones, J. (1969). Determination of the ground-water component of peak discharge from the chemisty of total runoff. *Water Resources Research*, 5(2):438–445.

Poage, M. and Chamberlain, C. (2001). Empirical relationships between elevation and the stable isotope composition of precipitation: Considerations for studies of paleoelevation change. *American Journal of Science*, 301(1):1–15.

Qu, Y. (2004). *An integrated hydrologic model for multi-process simulation using semi-discrete finite volume approach*. PhD thesis, Pennsylvania State University, State College, PA.

Railsback, L. (2007). Some fundamentals of mineralogy and geochemistry. Available at `http://www.gly.uga.edu/railsback/FundamentalsIndex.html`.

Rawling, G. (2005). Geology and hydrogeology of the Arroyo Seco area, Taos County, New Mexico. Open File Report 492, New Mexico Bureau of Geology and Mineral Resources, Socorro, NM.

Reiter, M. (2003). Hydrogeothermal studies in the Albuquerque Basin - a geophysical investigation of groundwater flow characteristics. Circular 211, NMBGMR, Socorro, NM.

Rodriguez, S. (1987). Impact of the ski industry on the Rio Hondo watershed. *Annals of tourism research*, 14(1):88–103.

Rodriguez, S. (2010). Taos Valley Acequia Association full color map. Available at `http://taosacequias.org/`.

Ruleman, C. and Machette, M. (2007). An overview of the Sangre de Cristo Fault system and new insights to interactions between Quaternary faults in the northern Rio Grande Rift. In Machette, M., Coates, M.-M., and Johnson, M., editors, *2007 Rocky Mountain Section Friends of the Pleistocene Field Trip—Quaternary Geology of the San Luis Basin of Colorado and New Mexico, September 7–9, 2007*, number 2007–1193, pages 187–197.

Schwartz, F., Fang, Y., and Parthasarathy, S. (2005). Patterns of evolution of research strands in the hydrologic sciences. *Hydrogeology Journal*, 13(1):25–36.

Selker, J., van de Giesen, N., Westhoff, M., Luxemburg, W., and Parlange, M. (2006). Fiber optics opens window on stream dynamics. *Geophysical Research Letters*, 33.

Sharp, Z. (2007). *Principles of Stable Isotope Chemistry*. Pearson Prentice Hall, Upper Saddle River, NJ.

Sklash, M., Stewart, M., and Pearce, A. (1986). Storm runoff generation in humid headwater catchments: 2. A case study of hillslope and low-order stream response. *Water Resources Research*, 22(8):1273–1282.

Smolen, J. and van der Spek, A. (2003). *Distributed Temperature Sensing: A DTS Primer for Oil and Gas Production*. Shell International Exploration and Production, The Hague, The Netherlands.

Stewart, I., Cayan, D. R., and Dettinger, M. (2005). Changes toward earlier streamflow timing across western North America. *Journal of Climate*, 18:1136–1155.

Stober, I. and Bucher, K. (2005). The upper continental crust, an aquifer and its fluid: Hydraulic and chemical data from 4 km depth in fractured crystalline basement rocks at the KTB test site. *Geofluids*, 5:8–19.

Street-Perrott, F. and Barker, P. (2008). Biogenic silica: a neglected component of the coupled global continental biogeochemical cycles of carbon and silicon. *Earth Surface Processes and Landforms*, 33:1436–1457.

Thyne, G., Gillespie, J., and Ostdick, J. (1999). Evidence for interbasin flow through bedrock in the southeastern Sierra Nevada. *GSA Bulletin*, 111(11):1600–1616.

Tiedeman, C., Goode, D., and Hsieh, P. (1997). Numerical simulation of ground water flow through glacial deposits and crystalline bedrock in the Mirror Lake area, Grafton County, New Hampshire. USGS Professional Paper 1572, USGS.

Tóth, J. (1963). A theoretical analysis of groundwater flow in small drainage basins. *Journal of Geophysical Research*, 68(16):4795–4812.

TSV (2012). Taos Ski Valley history. Available at: `http://www.skitaos.org/content/history`.

Tyler, S., Selker, J., Hausner, M., Hatch, C., Torgersen, T., Thodal, C., and Schladow, S. (2009). Environmental temperature sensing using Raman spectra DTS fiber-optic methods. *Water Resources Research*, 45.

Umstot, T. and Wilson, J. (2011). The hydrology of the San Gabriel Mountains near Los Angeles, California. Presented as part of NMT Earth and Environmental Science Department Hydrology Lecture Series.

Upson, J. (1939). Physiographic subdivisions of the San Luis Valley, Southern Colorado. *Journal of Geology*, pages 721–736.

USDA, N. R. C. S. (2008). Soil Survey Geographic (SSURGO) database for Taos County and parts of Rio Arriba and Mora Counties, New Mexico. Available at `http://SoilDataMart.nrcs.usda.gov/`.

USDA, N. R. C. S. (2012). National Elevation Data (10 m). Available at `http://ned.usgs.gov/` by the NRCS National Cartography and Geospatial Center.

USGS (2006). National Land Cover Data Set (NLCD). Available at `http://datagateway.nrcs.usda.gov/GDGOrder.aspx` by the USGS Multi-Resolution Land Characteristics (MRLC) Consortium.

USGS, G. A. P. (2004). Digital landcover dataset for the southwestern United States. Available at `http://earth.gis.usu.edu/swgap/`.

Warneck, P. (1987). *Chemistry of the Natural Atmosphere*. Academic Press, Inc., San Diego, CA.

Wasiolek, M. (1995). Subsurface recharge to the Tesuque aquifer system from selected drainage basins along the western side of the Sangre de Cristo Mountains near Santa Fe, New Mexico. Water-Resources Investigations Report 94-4072, USGS.

Williams, A., Lund, L., Johnson, J., and Kabala, Z. (1998). Natural and anthropogenic nitrate contamination of groundwater in a rural community, California. *Environmental Science and Technology*, 32:32–39.

Wilson, J. and Guan, H. (2004). Mountain-block hydrology and mountain-front recharge. *Groundwater recharge in a desert environment: the southwestern United States*, pages 113–137.

Winter, T. and Rosenberry, D. (1995). The interaction of ground water with prairie pothole wetlands in the Cottonwood Lake area, east-central North Dakota. *Wetlands*, 15(3):193–211.

Winter, T., Rosenberry, D., and LaBaugh, J. (2003). Where does the ground water in small watersheds come from? *Ground water*, 41(7):989–1000.

Wood, W. (1981). Guidelines for collection and field analysis of ground-water samples for selected unstable constituents. In *Techniques of Water-Resources Investigations of the United States Geological Survey, Book 1*, chapter D2. US Geological Survey, Alexandria, VA.

Woolhiser, D., Smith, R., and Goodrich, D. (1990). KINEROS, a kinematic runoff and erosion model: Documentation and user manual. Technical Report ARS-77, US Department of Agriculture Agricultural Research Service.

Zijl, W. (1999). Scale aspects of groundwater flow and transport systems. *Hydrogeology Journal*, 7:139–150.

Appendices

APPENDIX A

DISTRIBUTED TEMPERATURE SENSING SURVEY

Distributed Temperature Sensing (DTS) relies on the Raman spectra backscattering of laser light in a glass fiber optic cable to determine temperature along the distance of the fiber. The Anti-Stokes (high frequency) component of the Raman backscattering is strongly temperature dependent while the Stokes (low frequency) component shows little temperature effect. By comparing the ratio of the two, the temperature can be calculated (Smolen and van der Spek, 2003). This technique allows continuous measurements with high spatial and temporal resolution across kilometers-long study areas. This makes it useful for a variety of hydrologic field experiments, making it increasingly popular in the field of hydrology (Selker et al., 2006; Tyler et al., 2009)

In November 2010, a distributed temperature sensing (DTS) unit was deployed overnight on an approximately 1km-long stretch of the Rio Hondo near the mountain front of the Sangre de Cristos [Figure A.1]. The aim was to detect any temperature anamolies indicating possible groundwater upwelling along the mountain front. The DTS temperature profiling of the Rio Hondo was performed with a Sensortran Gemini dual-laser DTS system. The spatial resolution of this system is 1 m with accuracy of $\pm 0.3^{o}$C. Hobo temperature probes were placed at intervals along the cable to check the DTS results. Since solar radiation and cloud cover can affect temperature readings, we have only used the night-time data for

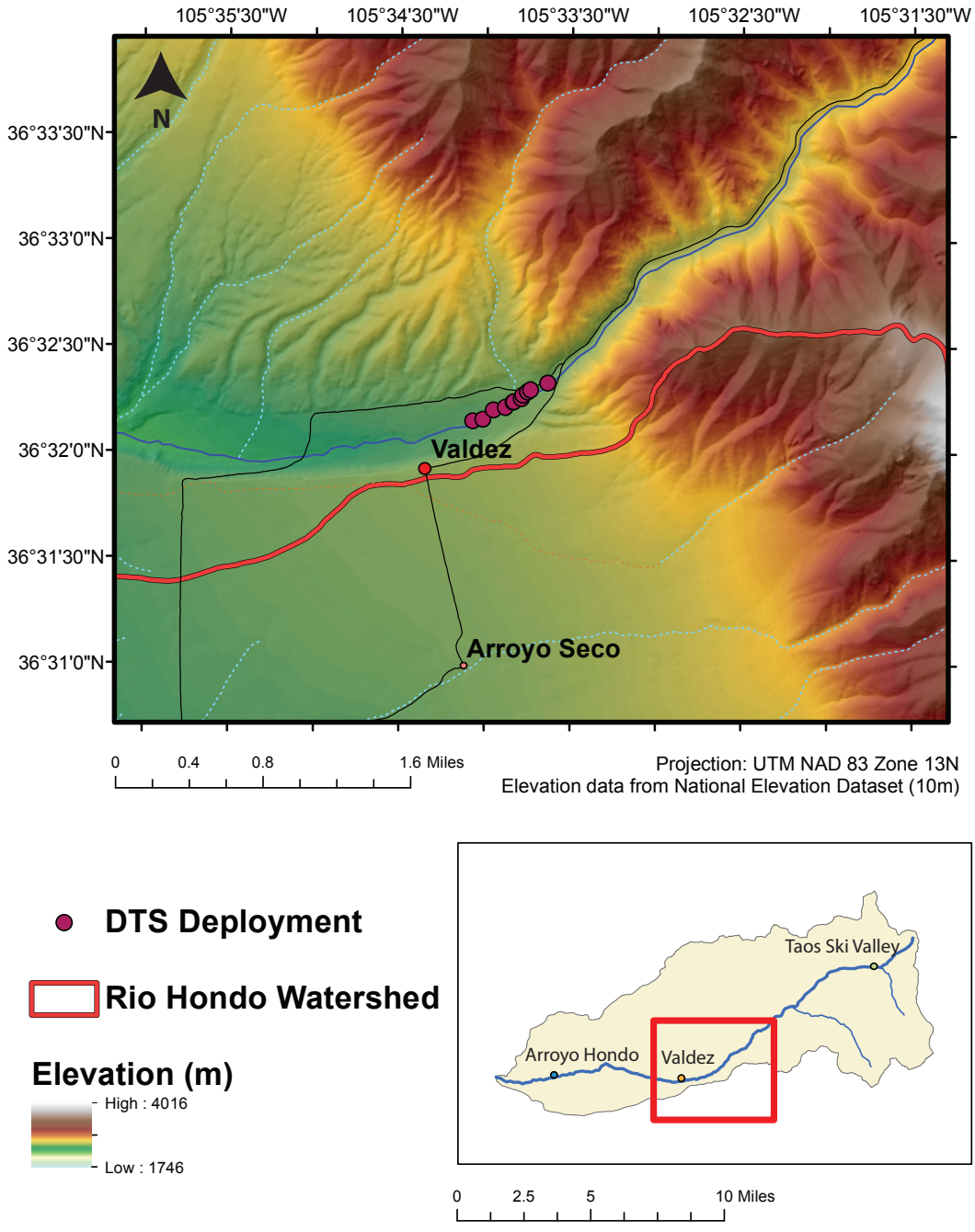

Figure A.1: Location of DTS deployment in the Rio Hondo. The DTS cable covered approximately 1 km of the Rio Hondo riverbed at the mountain front near Valdez, NM.

analyis. Since groundwater is also expected to be warmer than surface-water at this time of year, any groundwater inputs should be more pronounced at night when surface-water is even cooler. The results of this deployment indicate that while water generally cools as it moves downstream, one point near the mountain front is consistently warmer (by 0.5 -1 ^{o}C) than expected [Figure A.2]. This could be due to upwelling along the Sangre de Cristo fault zone that runs through this area (Rawling, 2005). Even without this small spike, the river water does appear to be warmer upstream. If we assume that warm water is likely groundwater, then this warming upstream could indicate either some discrete or diffuse upwelling points above our deployment zone that are contributing warmer groundwater to the river. As that water travels downstream, it would cool as it comes in contact with the atmosphere, unless it is again infused with more warm groundwater discharge. Another explanation is the existence of an atmospheric temperature inversion which leads to warmer air at higher altitude, a condition that can be common on clear winter nights. Since our deployment covers about 30 m of elevation, this could explain why upstream water is warmer and cools as it flows downstream. In our deployment, the downstream air temperature is consistently colder than the air temperature at the upstream end but unfortunately, this upstream air temperature measurement is too close to the end of the fiber optic cable to be completely reliable. In the future, consistent measurements of both upstream and downstream air temperatures during the deployment could more decisively determine the existence of a temperature inversion or other atmospheric condition that could be influencing stream temperatures. There is a portion of the river near the downstream end, where the water appears to warm again. In this area, there are wetlands with diffuse spring discharge, which may be contributing warmer water to the river as well. Future DTS deployments that

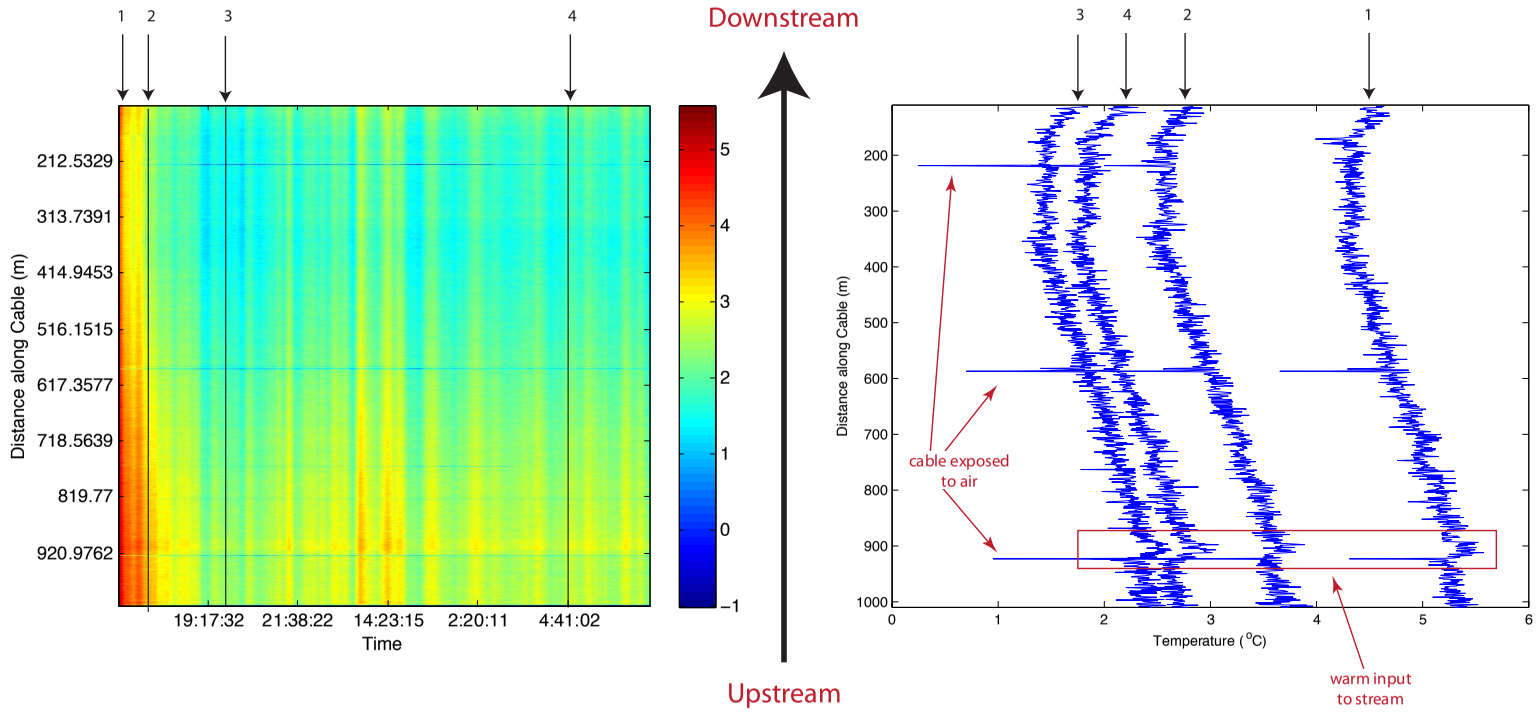

Figure A.2: DTS Results. The figure on the left shows a colormap of the temperature along the entire cable (spatial scale on vertical axis) throughout the night (temporal scale on horizontal axis). The warm patch (red) at the beginning of the night shows some residual warmth from the daytime temperatures. The spike in temperature that we propose may be groundwater upwelling is visible as a brighter yellow section continuing throughout the night at around meter marking 920 m. To show these temperature trends in more detail, different time cross-sections (black vertical lines) were picked and plotted separately in the figure on the right. This plot shows more clearly how the overall temperature in the river changes throughout the night. Note that the large spikes in cold temperature do not signify a change in stream temperature, but rather are places where the cable is exposed to the atmosphere.

cover more distance both above and below the mountain front fault zone could possibly determine other areas of significant groundwater discharge and further explore the trends observed in this deployment. The data from this and future DTS deployments could also be used in a simple, cross-sectional hydrothermal model that could better describe the groundwater flow system in this area.

APPENDIX B

RIO HONDO STREAMFLOW RECORDS

Since 1912, three USGS gauging stations have been operational at some point on the Rio Hondo. However, only gauging station 08267500: Rio Hondo near Valdez, NM is currently active [Figure B.1]. The following excercises only use data from this active gauge. Several measures were used to evaluate the effect of climate change on streamflow. Since climate change is predicted to cause decreases in streamflow, the first test is whether daily discharge has decreased. However, there is no noticeable downward trend in Rio Hondo discharge over the period 1934-2012 [Figure B.2]. Climate change is also predicted to accelerate the beginning of spring snowmelt. Thus, another test is whether spring snowmelt has begun earlier in the year. The day when spring snowmelt starts is defined as the date at which streamflow has the most negative cumulative departure from the yearly mean flow (Cayan et al., 2001). According to this calculation though, the Rio Hondo has not been experiencing an earlier spring [Figure B.3]. A changed environment that warms earlier in the year would also push the center of mass of the annual flow earlier in the year. The center of mass of annual discharge (CT) is determined using the formula given in Stewart et al. (2005): $CT = \Sigma(t_i q_i)/\Sigma q_i$, where t_i is the time in days from the beginning of the year and q_i is the streamflow on that day. A test for this, however, shows that the center of mass is generally unchanged since 1934 [Figure B.4]. Based on these measures,

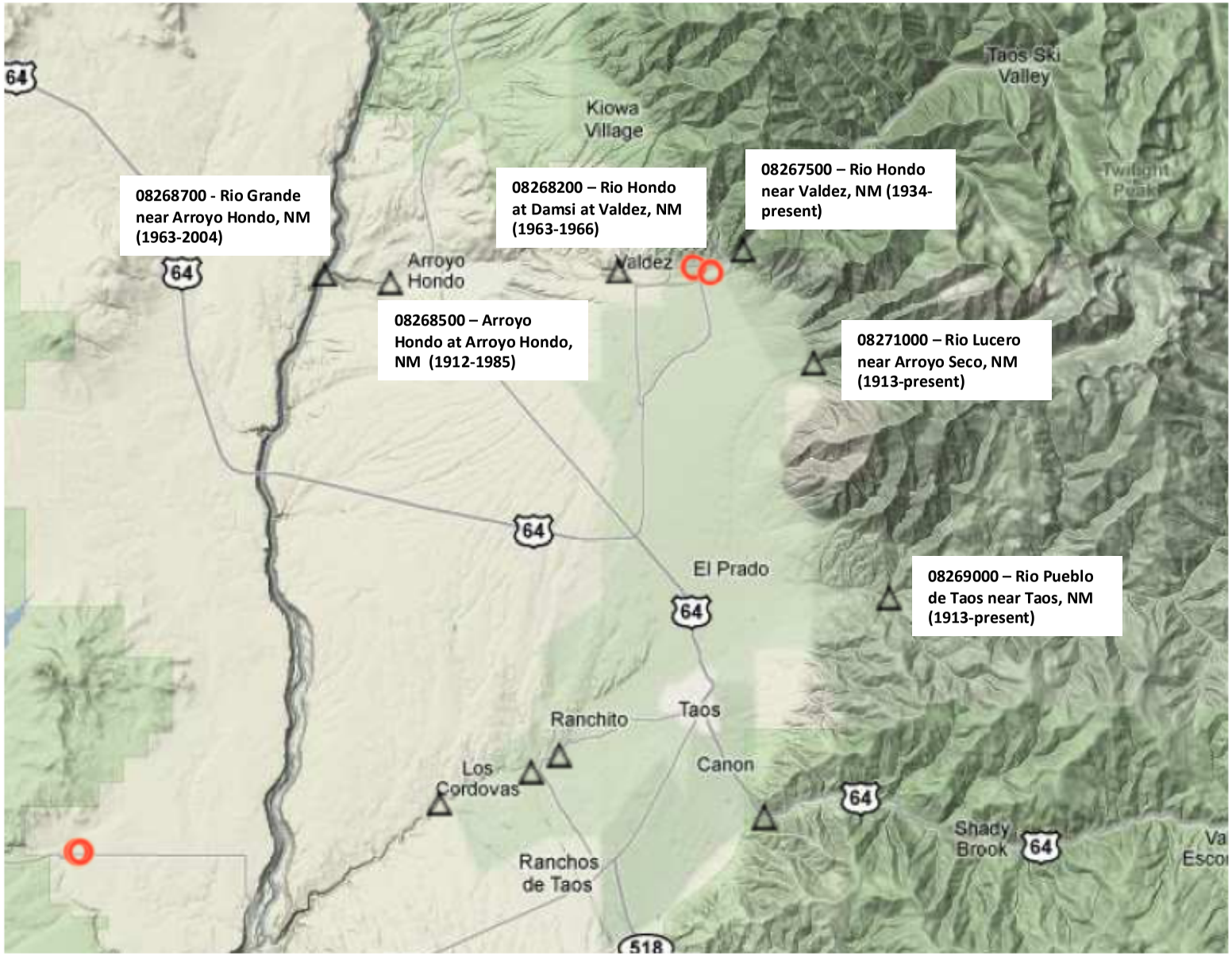

Figure B.1: USGS Gauging Stations on or near Rio Hondo (black triangles indicate gauging stations).

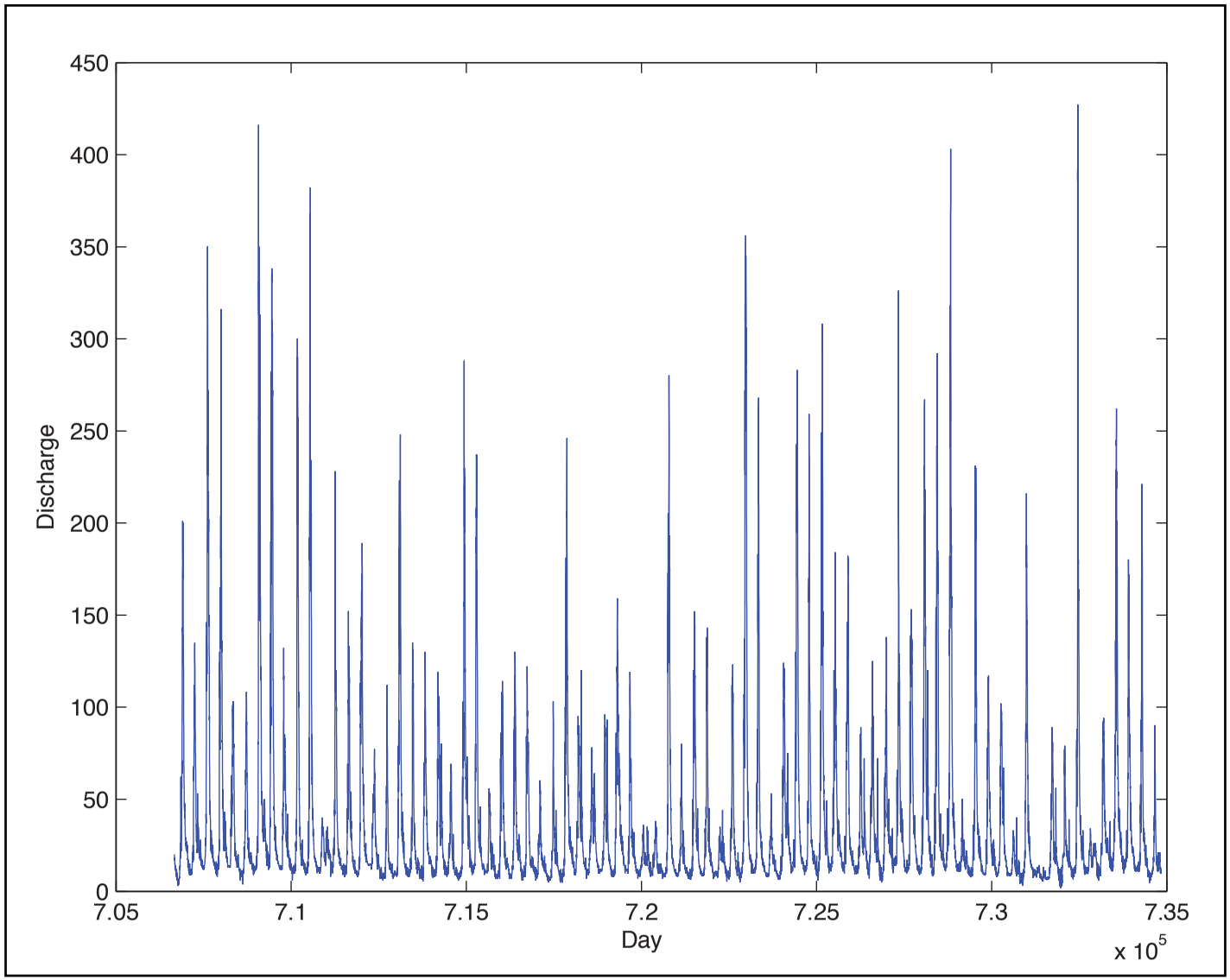

Figure B.2: Rio Hondo Discharge 1934-2012

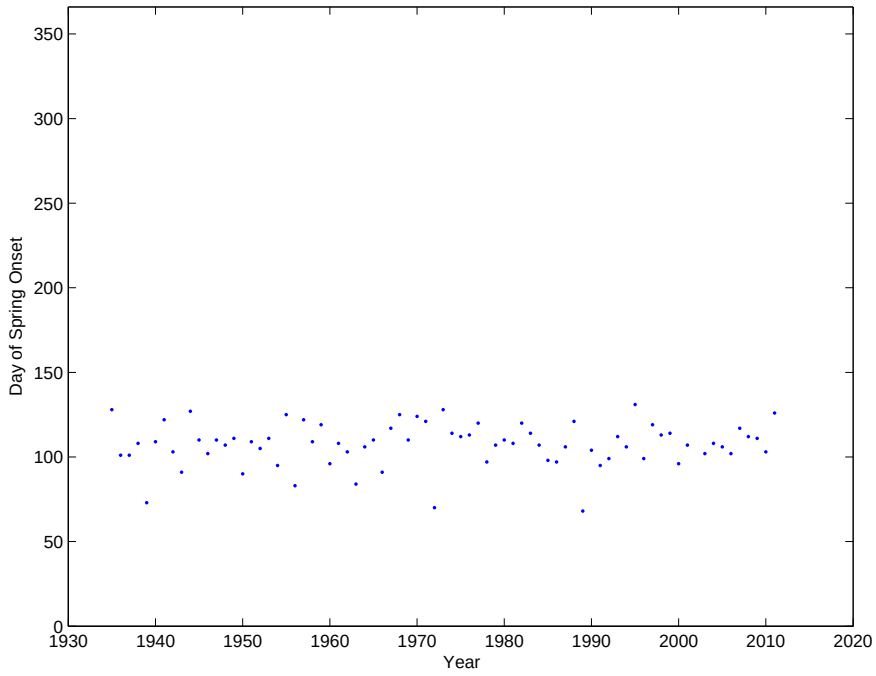

Figure B.3: Onset of spring snowmelt pulse in Rio Hondo 1934-2012.

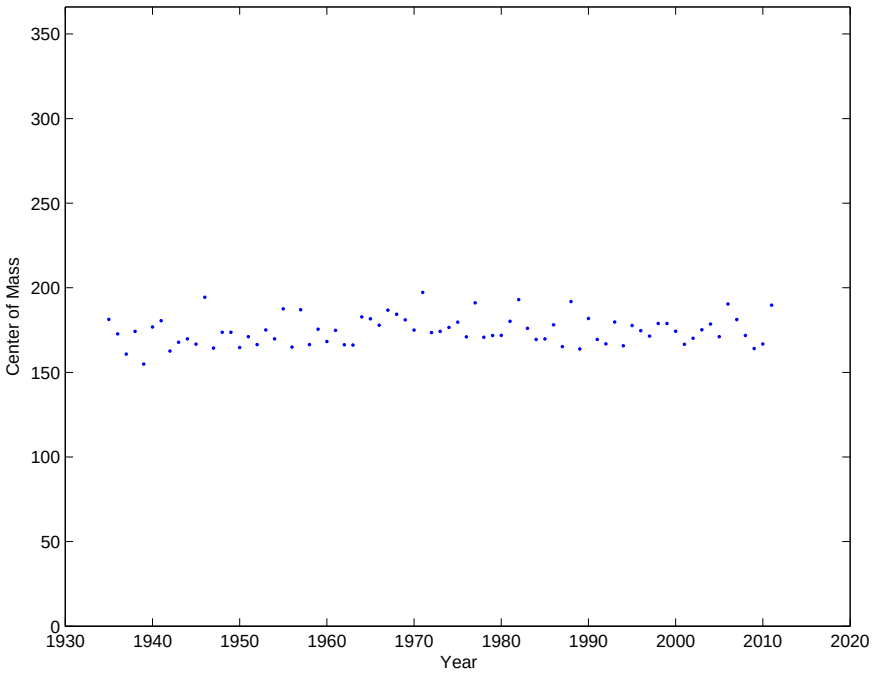

Figure B.4: Center of mass of annual streamflow in Rio Hondo 1934-2012.

Rio Hondo does not appear to have experienced any significant changes expected as a result of climate change yet. However, as the environment of northern New Mexico continues to change, as predicted in NMOSE (2006b), perhaps Rio Hondo will suffer some of these consequences in the future.

APPENDIX C

RESULTS OF STABLE ISOTOPE AND MAJOR ION ANALYSES

Sample ID	Sample Location	UTM-E	UTM-N	Elevation (m)
ISO1	TSV ridge isotope collector	459142	4047922	3642
ISO2	TSV near Whistlestop Isotope Collector	459184	4048617	3356
ISO3	TSV parking lot isotope collector	459099	4050201	2837
ISO4	Rio Hondo Valley isotope collector	454413	4047722	2561
ISO5	Valdez isotope collector	449178	4043485	2300
ISO6	Arroyo Hondo isotope collector	439312	4043543	2053
RGS1	Stagecoach spring discharging to Rio Grande	435150	4040576	1971
RGS2	Rio Grande upstream of Stagecoach spring	435150	4040608	1971
RHR1	USGS gauge	450182	4044206	2345
RHR2	Arroyo Hondo Gorge	436772	4043424	1995
RHR3	Gates of Valdez	445702	4043495	2209
RHR4	Arroyo Hondo Bridge	440346	4043512	2074
RHR5	Acequia return flow in Arroyo Hondo	438922	4043270	2041
RHR6	Reservoir at Bavarian	460689	4048151	3109
RHR7	Rio Hondo upstream of Bavarian	460641	4048041	3109
RHR8	Rio Hondo upstream of TSV resevoir	460379	4049171	2985
RHR9	Tributary entering TSV reservoir	460411	4049243	2988
RHR10	Rio Hondo at TSV near foot bridge	459810	4050045	2875
RHR11	East Fork	459866	4050220	2895
RHR12	Gavilan Canyon (near Inn at TSV)	457164	4050092	2745
RHR13	Italianos Canyon	455679	4048878	2645
RHR14	Manzanitas Canyon	454655	4047865	2565
RHR15	Rio Hondo upstream of South Fork	454493	4047770	2553
RHR16	South Fork	454459	4047740	2551
RHR17	Yerba Canyon	453573	4047210	2504
RHR18	Rio Hondo above TSV spring	460738	4047703	3151

Sample ID	Sample Location	UTM-E	UTM-N	Elevation (m)
RHR20	AS waterfall	451861	4043142	2565
RHS1	Patterson spring	449069	4043551	2291
RHS2a	Booster station	460775	4047979	3122
RHS2b	Arroyo Seco horse pasture spring	451074	4041924	2432
RHS3	AS waterfall ceiling	451861	4043142	2565
RHS4	TSV water supply spring	460737	4047706	3151
RHS5	Soil seep at Manzanitas Canyon	454655	4047865	2565
RHS6	Acequia seepage Valdez	449133	4043485	2291
RHW1	Arroyo Hondo (SK) well	438825	4042646	2066
RHW2	Valdez (EP) well	447516	4043543	2263
RHW3	Arroyo Seco (EM) well	446745	4041841	2297
RHW4	El Salto (BC) well	451711	4042803	2531
RHW5	El Salto (NO)	450828	4042920	2481
RHW6	Rio Hondo Valley (TML) Well	457609	4050164	2766
RHW7	South Fork (TEC) well	454432	4047762	2549
RHW8	South Fork (MC) well	454445	4047694	2560
RHW9	Valdez (HdV) well	449583	4044054	2353
RHW11	El Salto (NOs) well	451048	4042669	2440
Snow1	Near TSV water supply spring	460744	4047704	3151
Snow2	Residual snow from TSV ridge	459142	4047922	3649
Snow3	Residual Snow near Bavarian	460834	4048213	3123
Snow4	Residual snow at TSV tributary	459864	4050223	2886
Snow5	Snowmelt runoff downhill of Ski Patrol	459435	4048257	3559
Snow6	Residual snow near Ski Patrol	459312	4048032	3600
Snow7	Snowmelt runoff below Whistlestop	459198	4048932	3269
SOIL1	Soil core below Ski Patrol building	459435	4048257	3559

Sample ID	Sample Location	UTM-E	UTM-N	Elevation (m)
SOIL2	Soil core near ISO2	459184	4048617	3356
SOIL3	Soil core below Whistlestop	459198	4048932	3269
SOIL4	Soil core from TSV ridge	459263	4048008	3607
USGS-TSV	USGS snow sampler at TSV	460163	4047596	3320

Table C.1: Sample locations for all water samples.

Sample ID	Date	$\delta^{18}O$	$\delta^{2}D$	Ca	Mg	Na	K	Alkalinity	Cl	SO_4	NO_3	SiO_2	Br
		‰	‰	ppm	ppm	ppm	ppm	ppm as HCO_3	ppm	ppm	ppm	ppm	ppm
RHR1	7/9/10	-13.9	-97.6	20.13	1.96	3.56	0.14	58.27	1.76	12.60	0.96	3.49	
RHR16	7/8/10	-13.7	-95.9	11.57	1.44	2.81	0.30	32.95	0.70	12.58	0.72	4.23	
RHR15	7/8/10	-14.1	-98.9	22.27	1.20	3.22	0.15	65.90	1.57	14.25	1.02	3.02	
RHR11	7/8/10	-14.4	-101.3	22.16	4.01	2.52	0.09	84.94	0.77	12.41	0.51	3.33	
RHR10	7/8/10	-14.0	-97.9	18.72	1.25	2.23	0.10	50.95	0.71	4.96	1.52	2.67	
RHR9	7/8/10	-14.2	-100.4	21.72	2.33	2.71	0.23	73.83	0.74	18.12	0.66	3.94	
RHR8	7/8/10	-14.0	-97.9	17.82	1.03	1.49	0.10	45.76	0.67	5.00	1.46	2.65	
RHR7	7/8/10	-14.1	-98.4	19.92	0.88	1.27	0.10	41.06	0.64	19.32	1.35	2.49	
RHR12	7/8/10	-14.4	-102.5	17.12	1.52	2.74	0.10	60.10	0.69	21.25	0.32	3.96	
RHR14	7/9/10	-13.9	-99.0	22.02	2.28	2.85	0.13	69.86	0.84	3.46	0.56	4.50	18.30
RHR14	7/9/10	-13.9	-98.9	22.09	2.28	3.15	0.15	69.56	0.85	17.21	0.42	4.67	
RGS1	7/9/10	-14.1	-104.6	25.50	5.32	69.59	6.04	179.39	26.15	72.14	2.77	30.72	1.06
RGS2	7/9/10	-13.0	-97.7	28.97	6.66	25.54	2.45	111.36	9.85	41.30	3.04	14.62	
RHR4	7/9/10	-13.7	-97.1	37.40	4.68	7.62	0.46	124.47	12.52	14.38	0.77	7.85	
RHR2	7/9/10	-13.4	-96.5	47.73	8.81	19.49	0.66	191.47	9.18	21.55	0.85	9.49	0.98
RHR1	11/19/10	-13.0	-93.1	23.84	2.29	3.75	0.25	72.00	1.78	14.79	0.95	3.33	
RHR2	11/19/10	-13.3	-95.4	40.75	6.44	10.89	0.71	146.44	4.25	21.91	1.51	6.88	0.03
RHR3	11/19/10	-13.5	-96.1	29.31	3.80	4.94	0.44	95.19	3.22	16.62	0.57	4.80	0.01
RHR4	11/19/10	-13.5	-96.0	29.66	3.88	5.10	0.52	98.85	2.95	15.64	0.43	4.78	0.01
RHR5	11/19/10	-13.3	-96.2	49.58	9.81	17.76	0.72	192.81	6.36	31.76	3.08	10.37	0.08
RHR6	11/20/10	-13.2	-91.1										
RHR7	11/20/10	-13.5	-93.1	24.80	0.41	1.53	0.10	50.03	1.09	29.77	1.31	0.01	
RHR8	11/20/10	-13.5	-93.3					0.00					
RHR9	11/20/10	-14.2	-99.7	22.11	2.23	2.22	0.25	73.22	0.85	4.96	0.77	3.36	

Sample ID	Date	$\delta^{18}O$	$\delta^{2}D$	Ca	Mg	Na	K	Alkalinity	Cl	SO_4	NO_3	SiO_2	Br
		‰	‰	ppm	ppm	ppm	ppm	ppm as HCO_3	ppm	ppm	ppm	ppm	ppm
RHR10	11/20/10	-13.6	-95.1	26.79	1.61	1.70	0.11	64.68	0.68	20.56	1.35	2.48	
RHR11	11/20/10	-14.3	-101.0	24.20	5.22	1.61	0.06	92.75	0.83	5.24	0.51	2.76	
RHR12	11/20/10	-14.3	-102.1										
RHR13	11/20/10	-14.0	-99.6										
RHR14	11/20/10	-13.8	-98.5	28.00	2.37	2.81	0.30	79.32	0.78	20.35	0.30	4.15	0.00
RHR15	11/20/10	-13.9	-97.8	25.14	2.23	3.37	0.21	76.88	2.25	12.75	0.83	2.78	
RHR16	11/20/10	-13.5	-95.2	16.77	1.72	2.69	0.25	40.27	0.28	19.52	1.06	4.04	
RHR17	11/20/10	-13.8	-98.6										
RHW1	11/19/10	-13.4	-95.7	42.45	8.84	74.91	0.78	294.10	3.96	66.88	1.37	9.22	0.01
RHW2	11/19/10	-13.9	-98.5	35.61	5.37	5.43	0.74	117.15	2.02	21.21	0.49	7.38	0.01
RHW3	11/19/10	-13.7	-97.3	66.95	22.96	26.54	1.00	346.58	4.13	19.50	6.51	9.79	0.02
RHS1	11/20/10	-13.7	-96.7	27.87	2.86	4.55	0.38	85.42	3.00	17.23	0.49	3.88	0.01
RHS4	12/1/10	-12.3	-83.8										
RHS2a	12/1/10	-12.3	-84.3										
RHR1	3/26/11	-13.2	-95.1	23.35	2.41	4.27	0.54	73.22	4.30	15.21	0.83	0.45	
RHR4	3/27/11	-13.1	-95.1	34.65	4.29	5.82	1.76	109.46	6.49	24.04	0.45	2.91	
RHR11	3/26/11	-13.8	-100.3	22.94	5.42	1.91	0.52	92.99	0.45	5.84	0.45	0.28	
RHR12	3/25/11	-14.1	-103.1	17.59	1.59	1.90	0.30	55.53	0.46	7.87	0.30	1.30	
RHR14	3/25/11	-13.6	-98.2	27.97	2.49	2.35	0.52	76.88	0.85	23.09	0.37	1.54	
RHR15	3/25/11	-13.6	-98.5	24.87	2.45	4.84	0.54	81.40	2.50	5.43	0.30	1.20	
RHR16	3/25/11	-13.2	-95.0	15.99	1.76	2.20	0.49	39.66	0.47	19.69	0.95	1.66	
RHR18	3/26/11	-13.2	-92.5	25.31	1.02	1.82	0.46	53.69	0.22	32.64	1.62	0.05	
RHS1	3/27/11	-13.5	-97.1	25.60	2.77	5.13	0.74	71.88	5.75	19.78	1.13	0.89	
RHS2b	3/25/11	-13.2	-96.3	60.89	11.88	21.66	0.14	273.97	7.28	13.13	0.08	20.61	0.13

Sample ID	Date	$\delta^{18}O$	$\delta^{2}D$	Ca	Mg	Na	K	Alkalinity	Cl	SO_4	NO_3	SiO_2	Br
		‰	‰	ppm	ppm	ppm	ppm	ppm as HCO_3	ppm	ppm	ppm	ppm	ppm
RHS4	3/26/11	-13.1	-92.3	25.00	1.03	1.77	0.44	46.13	0.23	33.66	1.73	0.00	
RHS3	3/25/11	-12.9	-100.3										
RHS5	3/27/11	-13.4	-98.5	27.82	2.46	3.11	0.73	78.35	0.60	24.16	0.25	2.16	
RHW4	3/25/11	-13.0	-96.2	39.21	6.37	11.75	0.15	148.27	1.59	24.02	1.04	5.50	0.07
RHW5	3/27/11	-12.8	-96.3	53.17	16.06	19.13	1.13	109.83	4.93	168.80	0.00	7.93	0.15
Snow1	3/26/11	-12.9	-97.3										
ISO2	3/26/11	-18.2	-136.1										
ISO5	3/26/11	-19.2	-145.0										
Snow2	3/26/11	-9.1	-64.1										
Snow3	4/30/11	-13.9	-102.2										
Snow4	4/30/11	-12.5	-94.4										
RHW6	4/30/11	-13.9	-98.8	35.71	3.64	7.97	1.23	108.61	11.69	11.72	2.01	3.45	0.00
RHW7	4/30/11	-13.5	-95.7	15.67	1.37	3.55	1.13	108.61	2.73	15.38	1.53	4.11	0.00
RHW8	4/30/11	-13.5	-95.1	16.54	1.50	2.27	0.87	39.78	2.99	17.62	2.13	3.97	0.46
RHW9	4/30/11	-11.6	-87.4	81.65	34.29	25.07	1.20	182.44	11.39	238.13	0.65	10.21	0.55
RHR1	6/10/11	-13.0	-90.2	18.55	1.26	1.94	0.64	51.25	1.91	13.71	1.28	2.60	0.00
RHR2	6/11/11	-12.6	-88.8	36.65	5.30	8.91	1.14	131.80	3.98	18.52	1.46	6.23	0.00
RHR4	6/10/11	-12.8	-89.7	25.24	2.59	3.27	0.97	80.18	2.77	7.82	0.70	4.08	0.00
RHR11	6/10/11	-13.4	-93.7	17.08	2.99	1.94	0.92	72.00	1.30	4.21	0.76	2.50	0.39
RHR12	6/11/11	-13.3	-94.3	16.90	1.03	2.13	0.78	57.36	1.08	3.41	0.59	3.04	0.00
RHR14	6/10/11			22.34	1.73	2.02	0.74	66.26	1.25	13.58	0.57	3.60	0.00
RHR15	6/10/11	-13.0	-90.4	22.13	1.38	1.82	0.64	59.80	1.71	15.50	1.52	2.24	0.00
RHR16	6/10/11	-13.1	-91.3	10.47	0.68	1.28	0.66	27.58	1.30	10.51	1.20	3.11	0.00
RHR18	6/10/11	-13.0	-89.8	21.29	0.53	0.98	0.44	48.81	1.25	24.62	2.03	1.81	0.00

Sample ID	Date	$\delta^{18}O$	$\delta^{2}D$	Ca	Mg	Na	K	Alkalinity	Cl	SO_4	NO_3	SiO_2	Br
		‰	‰	ppm	ppm	ppm	ppm	ppm as HCO_3	ppm	ppm	ppm	ppm	ppm
RHR20	6/11/11	-11.3	-84.7	4.36	0.73	2.90	0.49	24.41	1.29	3.12	0.59	6.71	0.00
RHS1	6/10/11	-12.8	-89.4	27.00	2.74	4.56	0.86	86.64	2.09	5.63	0.68	3.84	0.00
RHS3	6/11/11	-11.4	-85.5	5.74	1.22	3.10	0.72	16.47	1.27	3.30	0.48	8.11	0.00
RHS4	6/10/11	-12.9	-88.9	22.35	0.60	1.81	0.71	46.74	2.08	26.82	2.38	1.95	0.00
RHS5	6/10/11	-12.8	-90.2	25.67	1.96	2.22	0.61	73.22	1.43	17.95	0.61	4.05	0.00
RHW5	6/11/11	-11.4	-84.5	55.07	16.58	20.45	1.34	108.31	5.07	151.81	0.51	11.22	0.36
RHW6	6/11/11	-12.7	-90.1	35.92	3.68	7.15	0.85	115.20	13.01	12.01	1.80	3.39	0.00
RHW9	6/11/11	-11.3	-82.4	72.97	30.91	28.07	0.93	133.02	4.96	238.13	0.47	10.80	0.38
RHR10	6/11/11	-12.9	-89.3	22.73	0.00	0.72	0.12	49.18	1.44	21.60	1.92	0.01	0.00
Snow5	6/9/11	-11.0	-78.4										
Snow6	6/9/11	-15.4	-114.1										
Snow7	6/9/11	-9.6	-72.1	7.80	0.92	0.70	1.37	26.85	1.18	2.08	0.76	1.57	0.00
ISO2	6/9/11	-13.3	-93.1										
ISO3	6/10/11												
ISO5	6/10/11	-12.4	-88.3										
ISO6	6/10/11	-14.1	-102.6										
SOIL1	6/9/11	-12.7	-93.0										
SOIL2	6/9/11	-13.7	-109.7										
SOIL3	6/9/11	-14.8	-128.1										
RHR1	9/10/11	-13.4	-93.6	23.65	1.78	2.93	0.56	58.50	2.78	13.03	0.92	2.95	
RHR2	9/9/11	-12.8	-90.2	54.52	9.14	17.77	2.37	173.51	14.06	30.16	1.56	9.64	0.40
RHR4	9/10/11	-13.0	-91.9	43.82	4.90	6.09	1.84	123.71	5.37	14.94	0.49	6.87	
RHR10	9/9/11	-13.5	-94.1	25.44	0.99	0.92	0.37	56.10	1.16	18.92	1.48	2.10	
RHR11	9/9/11	-13.0	-91.9	23.89	4.25	0.85	0.43	76.51	1.22	5.24	0.59	2.52	

Sample ID	Date	$\delta^{18}O$	$\delta^{2}D$	Ca	Mg	Na	K	Alkalinity	Cl	SO_4	NO_3	SiO_2	Br
		‰	‰	ppm	ppm	ppm	ppm	ppm as HCO_3	ppm	ppm	ppm	ppm	ppm
RHR14	9/9/11	-14.0	-99.0	26.85	1.83	1.92	0.49	62.51	1.56	20.02	0.95	3.72	
RHR15	9/9/11	-13.2	-92.8	25.27	1.79	2.76	0.48	64.01	2.98	12.06	1.93	2.61	
fRHR18	9/9/11	-13.9	-98.3	22.92	0.31	0.54	0.19	37.70	0.98	25.49	1.52	1.63	
RHR20	9/10/11	-16.5	-109.1	4.78	0.78	2.65	0.22	15.20	1.72	4.09	0.87	7.86	0.84
RHS1	9/10/11	-13.8	-97.9	22.73	3.00	4.95	0.87	69.51	2.98	16.90	0.89	3.73	
RHS3	9/10/11	-12.0	-89.7	7.11	1.73	2.72	0.39	26.70	1.39	4.57	1.12	11.11	
RHS4	9/9/11	-14.1	-99.1	22.44	0.30	0.52	0.18	34.00	0.95	27.19	1.54	1.59	
RHS5	9/9/11	-13.8	-98.2	27.79	1.88	2.05	0.35	61.00	1.19	20.13	0.51	3.85	
RHS6	9/10/11	-13.5	-96.4	24.41	4.46	4.61	0.77	70.51	3.14	15.20	0.45	7.89	
RHW6	9/9/11	-14.0	-99.9	34.07	3.21	6.78	0.61	89.31	10.00	11.70	2.46	3.00	
SOIL2	11-Sep	-7.9	-68.6										
SOIL4	11-Sep	-14.5	-151.8										
ISO1	11-Sep	-7.2	-35.3										
ISO2	11-Sep	-7.3	-38.0										
ISO3	11-Sep	-5.9	-30.9										
ISO4	11-Sep	-5.2	-26.3										
ISO5	11-Sep	-4.1	-20.5										
ISO6	11-Sep	-4.2	-19.7										
USGS-TSV	11-Sep	-16.6	-122.4	0.33	0.03	0.04	0.08	0.16	0.02	0.21	0.16		
RHR1	11/18/11	-13.6	-96.0	25.18	2.48	4.07	0.79	70.17	9.41	16.20	0.72		
RHR2	11/18/11	-13.5	-95.8	41.00	6.34	11.06	1.23	139.12	3.37	14.91	1.35		
RHR10	11/18/11	-13.6	-95.2	27.82	1.72	1.96	0.66	65.04	5.22	21.29	1.78		0.62
RHR11	11/18/11	-14.2	-101.1	24.45	5.20	1.84	0.69	89.94	1.24	20.88	2.02		
RHR15	11/18/11	-13.8	-96.9	27.54	2.52	4.02	0.75	76.39	3.62	14.83	0.65		

Sample ID	Date	$\delta^{18}O$	$\delta^{2}D$	Ca	Mg	Na	K	Alkalinity	Cl	SO_4	NO_3	SiO_2	Br
		‰	‰	ppm	ppm	ppm	ppm	ppm as HCO_3	ppm	ppm	ppm	ppm	ppm
RHR16	11/18/11	-12.6	-89.3	16.40	1.82	2.90	0.97	39.05	3.31	13.37	1.45		
RHR18	11/18/11	-13.7	-95.3	25.72	1.06	1.87	0.55	46.01	1.21	29.90	1.58		
RHR20	11/19/11	-10.8	-74.6	3.82	1.11	2.96	0.43	13.91	1.21	6.53	1.90		
RHS1	11/19/11	-13.6	-96.1	28.84	3.12	5.13	0.91	84.20	10.68	18.59	0.64		
RHS4	11/18/11	-13.5	-94.7	25.89	1.08	0.80	0.47	43.93	1.09	31.41	1.30		
RHW5	11/18/11	-13.2	-97.3	49.46	15.74	22.57	1.42	102.51	1.14	149.61	2.12		
RHW6	11/18/11	-13.8	-98.0	36.41	3.84	6.82	0.90	109.59	10.80	11.37	1.75		
RHW10	11/19/11	-12.2	-91.4	73.09	31.24	24.51	1.23	205.02	4.94	209.08	0.66		0.67
RHW11	11/19/11	-12.8	-93.2	21.03	4.58	9.74	0.81	99.09	8.83	4.89	0.67		0.87
RHS3	11/19/11			7.32	2.09	4.30	0.95						

Table C.2: Results from stable isotope and geochemical analyses for all water samples.

Site ID	Location	Latitude	Longitude	Elevation (m)
CO00	Alamosa	37.4421	-105.868	2285
CO91	Wolf Creek Pass	37.4686	-106.787	3287
NM07	Bandelier	35.7788	-106.266	1997
NM12	Capulin Volcano	36.779	-103.981	2190

Table C.3: Locations of NADP stations used in this work

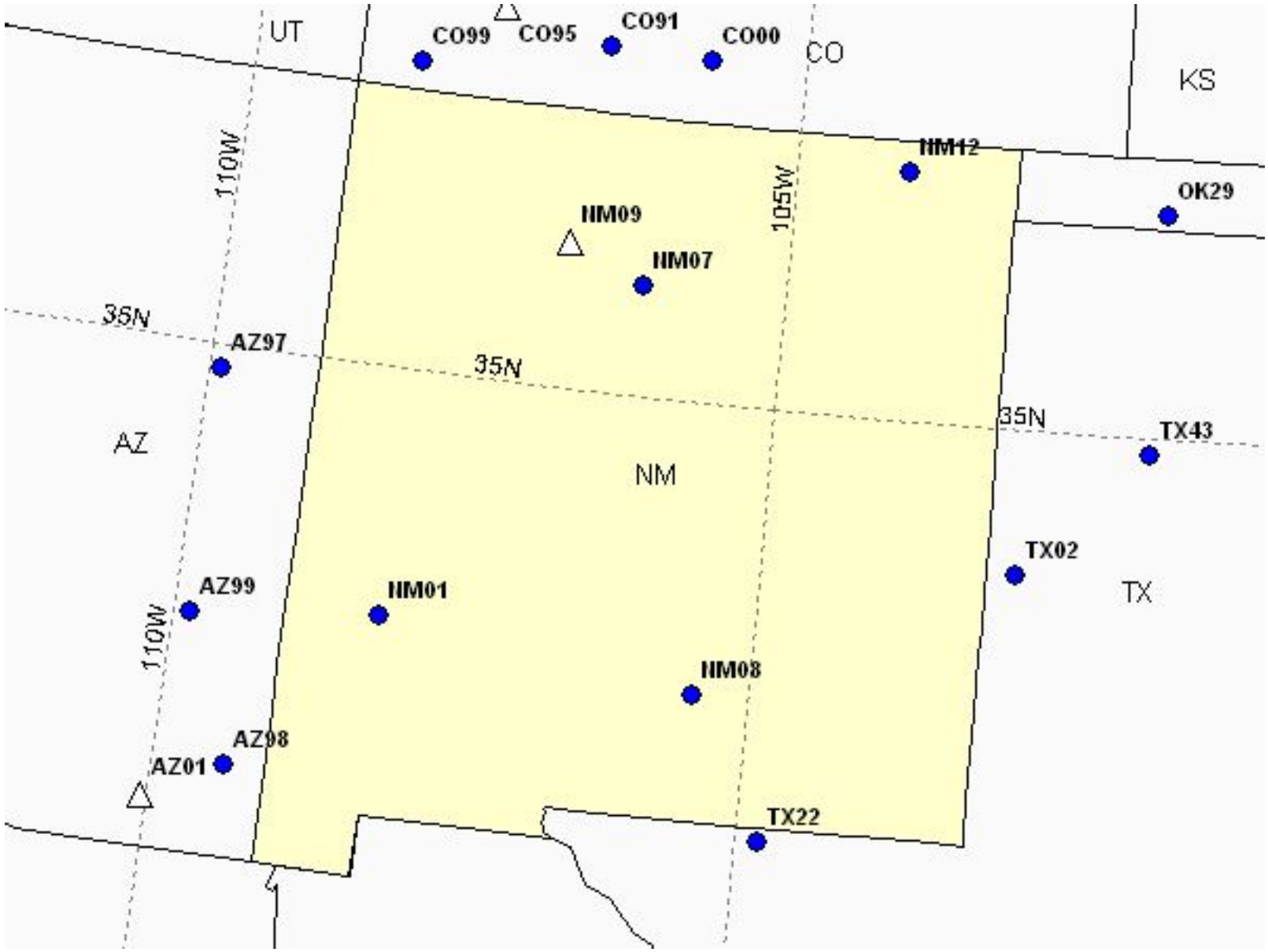

Figure C.1: Locations of National Atmospheric Deposition Program (NADP) sites. The data from NADP sites NM07, NM12, CO00 and CO91 were used to represent the chemistry of precipitation in the Rio Hondo region.

Sample Site	Sampling Date	Ca (ppm)	Mg (ppm)	Na (ppm)	K (ppm)	Cl (ppm)	SO_4 (ppm)
CO00	7/8/10	0.329	0.029	0.061	0.032	0.109	0.67
CO91	7/8/10	0.126	0.014	0.023	0.021	0.052	0.358
NM07	7/8/10	0.116	0.009	0.017	0.009	0.049	0.265
NM12	7/8/10	0.171	0.013	0.032	0.02	0.062	0.424
CO00	11/20/10	0.078	0.006	0.113	0.014	0.03	0.601
CO91	11/20/10	0.098	0.01	0.037	0.015	0.041	0.561
CO91	11/20/10	0.553	0.039	0.141	0.054	0.087	0.571
NM07	11/20/10	0.494	0.028	0.023	0.031	0.067	1.073
NM07	11/20/10	0.174	0.016	0.014	0.01	0.041	0.14
NM12	11/20/10	0.25	0.015	0.02	0.035	0.046	0.636
NM12	3/26/11	0.112	0.008	0.017	0.008	0.047	0.325
NM07	3/26/11	0.021	0.002	0.005	0.004	0.015	0.129
NM07	3/26/11	0.053	0.004	0.011	0.008	0.022	0.159
NM07	3/26/11	0.659	0.04	0.241	0.023	0.129	0.634
CO91	3/26/11	0.045	0.004	0.028	0.018	0.038	0.417
CO91	3/26/11	0.11	0.01	0.064	0.025	0.062	0.235
CO91	3/26/11	0.308	0.027	0.09	0.022	0.078	0.431
CO91	3/26/11	0.108	0.012	0.039	0.012	0.024	0.222
CO00	3/26/11	0.159	0.015	0.317	0.021	0.029	0.888
CO00	3/26/11	0.222	0.017	0.107	0.053	0.095	0.349
CO00	3/26/11	4.815	0.16	0.76	0.203	0.232	2.038
NM12	6/10/11	0.402	0.038	0.077	0.063	0.101	0.803
NM07	6/10/11	0.306	0.026	0.042	0.016	0.065	0.635
NM07	6/10/11	0.711	0.06	0.061	0.003	0.145	1.061
CO91	6/10/11	0.292	0.028	0.044	0.021	0.055	0.503
CO91	6/10/11	0.209	0.017	0.033	0.019	0.045	0.237

CO91	6/10/11	2.253	0.174	0.109	0.269	0.124	0.925
CO00	6/10/11	2.696	0.113	0.217	0.124	0.102	0.796
NM12	9/10/11	0.376	0.027	0.093	0.068	0.133	0.702
NM12	9/10/11	0.206	0.014	0.026	0.022	0.051	0.453
NM07	9/10/11	0.801	0.041	0.075	0.046	0.106	1.073
NM07	9/10/11	0.596	0.048	0.078	0.042	0.124	1.282
CO91	9/10/11	0.112	0.01	0.016	0.017	0.036	0.335
CO91	9/10/11	0.077	0.008	0.011	0.008	0.033	0.299
CO00	9/10/11	0.147	0.011	0.018	0.017	0.035	0.182
CO00	9/10/11	0.333	0.027	0.061	0.081	0.091	0.519

Sample Site	**Sampling Date**	**pH**	**Conductivity (μS/cm)**	**NO_3 (ppm)**
CO00	7/8/10	5.23	9.69	1.566
CO91	7/8/10	5.05	6.55	0.833
NM07	7/8/10	5.15	5.74	0.79
NM12	7/8/10	5.48	5.43	0.812
CO00	11/20/10	5.78	4.47	0.389
CO91	11/20/10	5.03	6.62	0.681
CO91	11/20/10	5.68	7.01	0.782
NM07	11/20/10	5.02	11.8	1.761
NM07	11/20/10	4.93	7.6	1.252
NM12	11/20/10	5.58	5.95	0.695
NM12	3/26/11	5.62	3.9	0.582
NM07	3/26/11	5.45	3.09	0.369
NM07	3/26/11	5.34	3.3	0.305
NM07	3/26/11	6.27	8.7	1.54

CO91	3/26/11	5.12	5.09	0.385
CO91	3/26/11	4.79	9.89	1.421
CO91	3/26/11	5.26	6.56	1.007
CO91	3/26/11	5.45	3.35	0.444
CO00	3/26/11	5.6	6.26	0.639
CO00	3/26/11	5.99	6.3	1.147
CO00	3/26/11	7.18	32.4	0.758
NM12	6/10/11	6.43	8.32	0.775
NM07	6/10/11	5.33	6.68	0.716
NM07	6/10/11	5.35	9.1	1.368
CO91	6/10/11	5.64	5.35	0.873
CO91	6/10/11	5.67	3.3	0.418
CO91	6/10/11	6.78	16	1.173
CO00	6/10/11	7.1	18.4	0.528
NM12	9/10/11	6.08	8.59	1.3
NM12	9/10/11	5.12	7.7	1.484
NM07	9/10/11	6.22	11.4	2.156
NM07	9/10/11	5.1	15.82	3.102
CO91	9/10/11	5.02	6.28	0.803
CO91	9/10/11	4.83	8.22	0.989
CO00	9/10/11	5.83	4.3	0.881
CO00	9/10/11	6.24	9.42	1.637

Table C.5: NADP geochemical data from NADP (2012)

APPENDIX D

DISCUSSION ON PICARRO STABLE ISOTOPE INSTRUMENT

Since the mountain front wells, as discussed in Section 3.5, have such a unique stable isotopic signature, these and other control samples (non- mountain front well samples) were re-run in order to see if the results were replicable. Fortunately, we found that the mountain front wells did again show the same trend, offset parallel to the local water line. However, during the re-run, we noticed that all of the samples, including the control samples, were consistently shifted to the left of their original values [Figure D.1]. This doesn't affect our interpretation of the stable isotope results presented in Section 3.5 since we still see the same behavior in our major water types across seasons. However, this does have implications for the Picarro instrument used at NMT and the interpretation of its analyses. This discussion is therefore included as an appendix for the benefit of those who rely on the results of this instrument. One explanation for the shift we observed is that the laser in the machine was re-calibrated right before we re-ran the samples, which might account for the consistency of the shift across all the samples. However, by plotting the old and new values against one another [Figure D.2], it is clear that the samples don't just plot parallel to a 1:1 line but are more scattered. Therefore, it's not simply an issue of calculating a correction factor for the samples taken before the laser adjustment. One explanation for this scattering is the method of calibration. The data are calibrated using values from

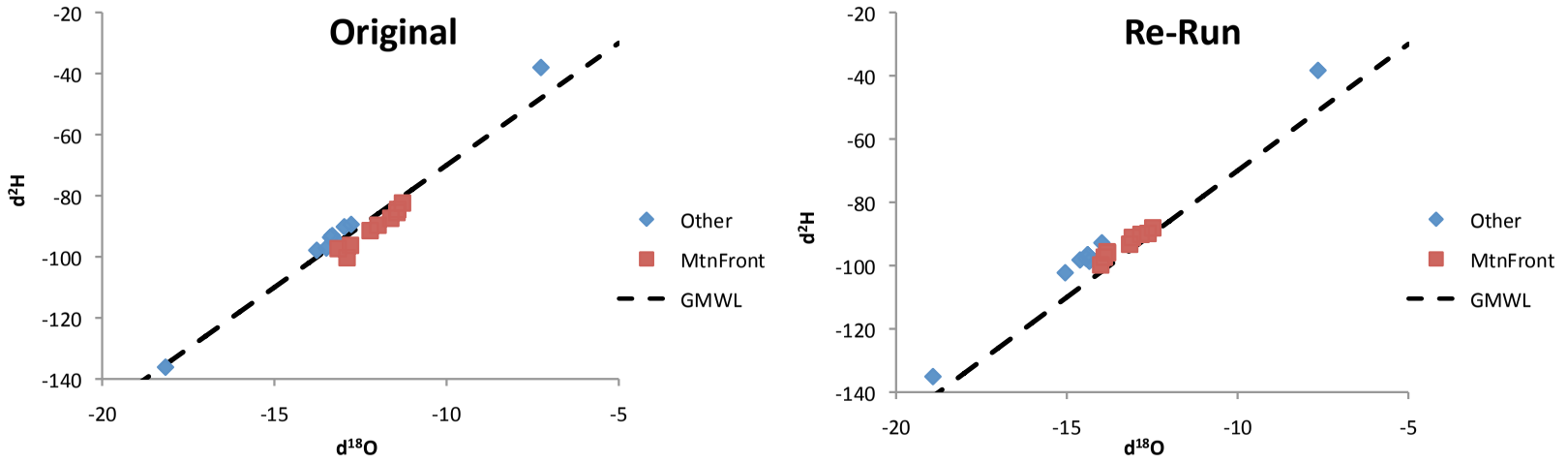

Figure D.1: Results of stable isotope results for mountain front wells and control samples from original runs and from the re-run.

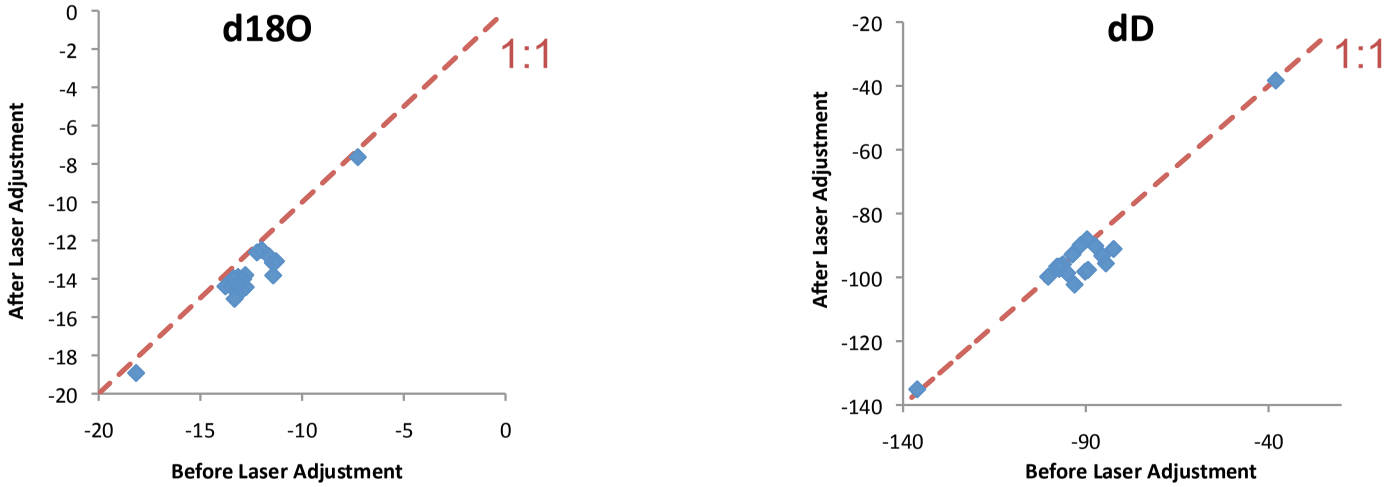

Figure D.2: Comparison of stable isotope results from the same samples before and after Picarro laser adjustment.

standard solutions run at the same time as the samples. Sometimes these standards run low and it is possible that the standards might run so low that they undergo increased fractionation due to air-water interactions within the bottle. In this case, the calibration for each season of Old values would be slightly different. This could also explain why some of my original sample results show much less seasonal variation in the re-run [Figure D.3] since in the re-run there is one calibration factor rather than 3 from different runs. Another possible explanation for having less scatter in the re-run results is a slight methodological difference between the original runs and the re-run. In the original runs, each sample was analyzed 3 times and these analysis results were averaged before calibration. A sample analysis result was only thrown out if it was sufficiently different from the other 2 analysis results. In the re-run, each sample was analyzed 6 times and then the first 3 analysis results were automatically thrown out, to account for any possible memory effects in the machine. Then the last 3 sample analysis results were averaged and calibrated using the standards. If there were memory effects in the analysis results when only 3 analyses were used, then this would also explain the scatter in the original runs. In the future, there should be a consistent analysis protocol for the Picarro in which standards are freshly made with each run, the samples are analyzed 6 times each, and random samples are re-run at intervals to check that results are replicable.

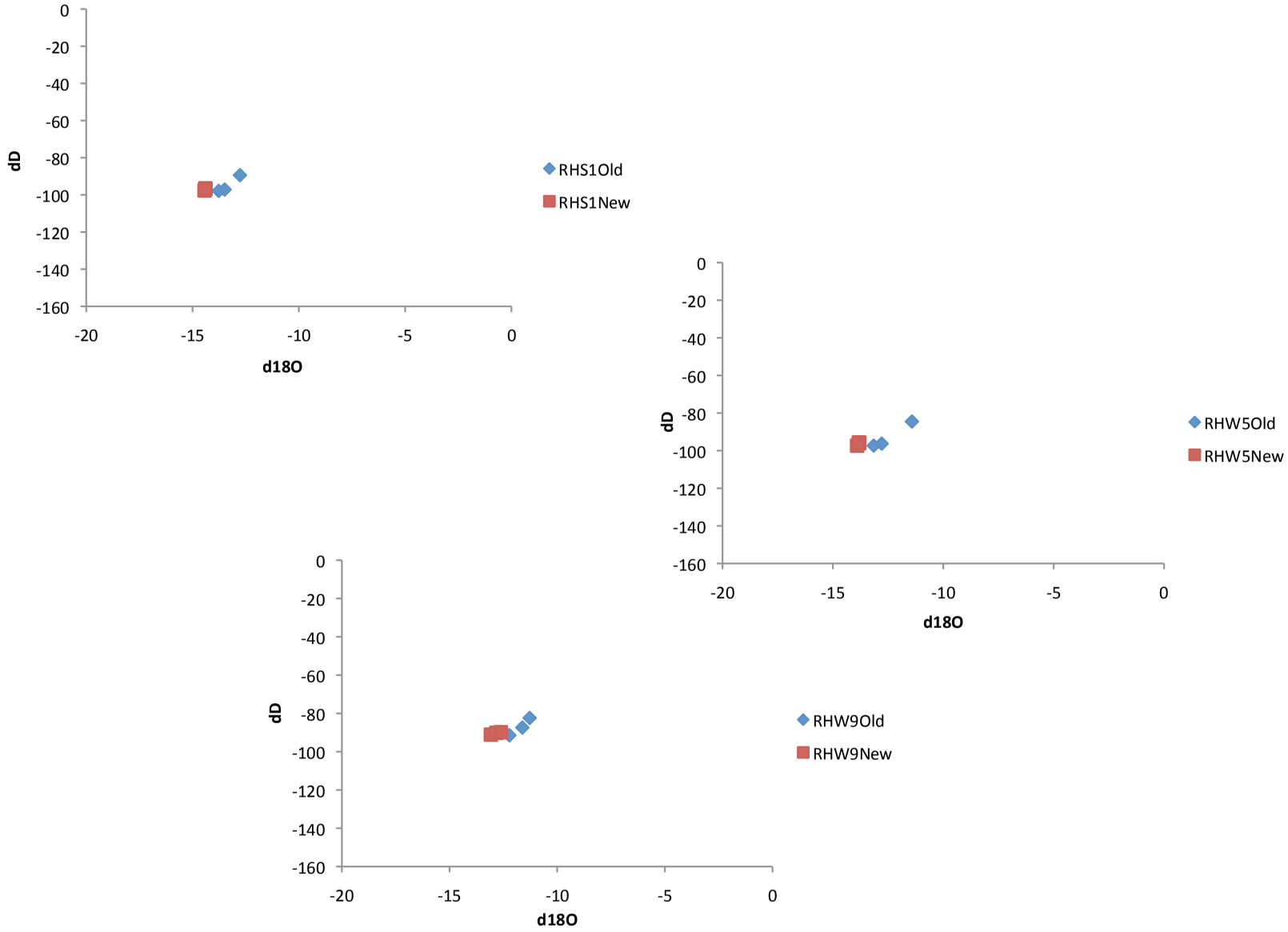

Figure D.3: Comparison of individual samples' stable isotope results before and after Picarro laser adjustment.

APPENDIX E

RESULTS OF MODEL SENSITIVITY ANALYSES

E.1 Model Width

Model	Model Width	Origin	Discharge (m^2/s)	Total age flux (m^2yr/s)
Whole	30000	0	955	858797
Trad	4988	11523	1027	2494029
Extend1	9976	8428	925	712387
Extend2	14963	6535	962	778239
MtValley	6881	11523	1163	3384469
MtCenter	4988	13416	898	2415512
Hillslope	3095	13416	796	1549157

Table E.1: Sensitivity of Discharge and Age to Model Width

Model	DS Divide location (m)	US Divide location (m)
Whole	11870.5	16873.5
Trad	11523	16510
Extend1	11782.5	17277.5
Extend2	11821.5	16947.5

Table E.2: Sensitivity of groundwater divide to Model Width

E.2 Model Thickness

Model	Model Thickness (m)	Discharge (m^2/s)	Total age flux (m^2yr/s)
Whole	5000	955	858797
	4500	953	861124
	4000	951	864202
	3500	950	869912

	3000	949	880248
	2750	947	889556
	2500	946	900679
	2250	942	907827
	2000	937	897818
	1750	926	849450
	1500	907	747010
	1250	871	623765
	1000	808	498768
	975	799	486291
	950	790	473805
	925	781	461289
	900	771	448845
	875	760	436357
	850	749	423891
	825	738	411412
	800	726	398956
	775	713	386497
	750	700	373974
	725	686	361527
	700	671	349081
	675	656	336626
	650	640	324121
	625	623	311735
	600	606	299305
	575	588	286828
	550	569	274362
	525	550	261950
	500	529	249522
	475	509	237103
	450	487	224696
	425	464	212275
	400	441	199869
	375	418	187468
	350	393	175050
	325	368	162689
	300	342	150267
	275	316	137846
	250	289	125442
	225	262	113176

	200	234	100538
	175	206	88040
	150	177	75345
	125	148	62627
	100	119	49379
	75	89	36637
	50	60	22758
	25	30	10899
Trad	5000	1027	2494029
	4500	1026	2244633
	4000	1024	1995354
	3500	1022	1746028
	3000	1016	1496622
	2750	1012	1371907
	2500	1006	1247042
	2250	997	1122297
	2000	984	997676
	1750	965	872971
	1500	935	748249
	1250	890	623535
	1000	818	498791
	975	808	486330
	950	799	473848
	925	789	461384
	900	778	448911
	875	767	436442
	850	755	423969
	825	743	411505
	800	730	399029
	775	717	386560
	750	703	374093
	725	689	361624
	700	674	349157
	675	658	336688
	650	642	324217
	625	625	311754
	600	607	299287
	575	589	286824
	550	570	274358
	525	550	261894

	500	530	249436
	475	509	236972
	450	487	224512
	425	465	212054
	400	442	199594
	375	418	187137
	350	393	174683
	325	368	162226
	300	343	149769
	275	316	137315
	250	289	124855
	225	262	112393
	200	234	99923
	175	206	87437
	150	177	74940
	125	148	62413
	100	119	49859
	75	89	37261
	50	60	24658
	25	30	12026
Extend1	5000	925	712387
	4500	927	708917
	4000	929	705594
	3500	931	703150
	3000	934	702562
	2750	935	703145
	2500	936	704842
	2250	935	710962
	2000	931	722943
	1750	923	712109
	1500	905	675615
	1250	870	612252
	1000	807	496859
	975	799	484723
	950	790	472525
	925	781	460291
	900	771	448009
	875	760	435708
	850	749	423364
	825	738	411031

	800	726	398653
	775	713	386265
	750	700	373857
	725	686	361452
	700	671	349035
	675	656	336597
	650	640	324160
	625	623	311720
	600	606	299273
	575	588	286823
	550	569	274378
	525	550	261927
	500	530	249476
	475	509	237025
	450	487	224576
	425	465	212130
	400	441	199684
	375	418	187239
	350	393	174797
	325	368	162355
	300	342	149911
	275	316	137470
	250	289	125037
	225	262	112561
	200	234	100084
	175	206	87604
	150	177	75065
	125	148	62479
	100	119	49842
	75	89	37119
	50	60	24398
	25	30	11797
Extend2	5000	962	778239
	4500	960	776124
	4000	958	776203
	3500	955	779226
	3000	952	785324
	2750	950	789266
	2500	948	793396
	2250	944	796495

	2000	938	794775
	1750	927	782023
	1500	907	731061
	1250	871	623442
	1000	808	498822
	975	799	486367
	950	790	473866
	925	781	461404
	900	771	448930
	875	760	436460
	850	749	423979
	825	738	411510
	800	726	399029
	775	713	386564
	750	700	374103
	725	686	361624
	700	671	349160
	675	656	336695
	650	640	324231
	625	623	311768
	600	606	299319
	575	588	286861
	550	569	274407
	525	550	261957
	500	529	249507
	475	509	237065
	450	487	224622
	425	465	212189
	400	441	199748
	375	418	187320
	350	393	174889
	325	368	162474
	300	342	150024
	275	316	137611
	250	289	125152
	225	262	112699
	200	234	100219
	175	206	87699
	150	177	75149
	125	148	62528

	100	119	49827
	75	89	37010
	50	60	23875
	25	30	10972

Table E.3: Sensitivity of Discharge and Age to Model Thickness

Model	**Model Thickness (m)**	**US Divide location (m)**
Whole	5000	16873.5
	4000	16870.5
	3000	16868.5
	2000	16856.5
	1000	16669.5
	900	16640.5
	800	16614.5
	700	16590.5
	600	16569.5
	550	16560.5
	500	16551.5
	450	16544.5
	400	16537.5
	350	16531.5
	300	16525.5
	250	16521.5
	200	16517.5
	150	16514.5
	100	16512.5
	50	16511.5
	25	16510.5
Trad	5000	16510
	4000	16510
	3000	16510
	2000	16510
	1000	16510
	900	16510
	700	16510
	500	16510
	400	16510
	200	16510

	25	16510
Extend1	5000	17277.5
	4000	17209.5
	3000	17093.5
	2000	16910.5
	1000	16659.5
	900	16634.5
	700	16589.5
	500	16551.5
	400	16537.5
	200	16517.5
	25	16510.5
Extend2	5000	16947.5
	4000	16920.5
	3000	16892.5
	2000	16860.5
	1000	16669.5
	900	16640.5
	700	16590.5
	500	16551.5
	400	16537.5
	200	16517.5
	25	16510.5

Table E.4: Sensitivity of groundwater divide to model thickness

E.3 Permeability

	K (m/s)	**Discharge (m^2/s)**	**Total age flux (m^2yr/s)**
Whole	1.0E-13	9.6E-04	2.5E+06
	3.8E-13	3.6E-03	2.5E+06
	1.4E-12	1.4E-02	2.2E+06
	5.5E-12	5.2E-02	1.6E+06
	2.1E-11	2.0E-01	1.1E+06
	7.9E-11	7.5E-01	9.4E+05
	3.0E-10	2.8E+00	8.8E+05
	1.1E-09	1.1E+01	8.7E+05
	4.3E-09	4.1E+01	8.6E+05

	1.6E-08	1.5E+02	8.6E+05
	6.2E-08	5.9E+02	8.6E+05
	2.3E-07	2.2E+03	8.6E+05
	8.9E-07	8.5E+03	8.6E+05
	3.4E-06	3.2E+04	8.6E+05
	1.3E-05	1.2E+05	8.6E+05
	4.8E-05	4.6E+05	8.6E+05
	1.8E-04	1.7E+06	8.6E+05
	7.0E-04	6.6E+06	8.6E+05
	2.6E-03	2.5E+07	8.6E+05
	1.0E-02	9.6E+07	8.6E+05
Trad	1.0E-13	1.0E-03	2.5E+06
	3.8E-13	3.9E-03	2.5E+06
	1.4E-12	1.5E-02	2.5E+06
	5.5E-12	5.6E-02	2.5E+06
	2.1E-11	2.1E-01	2.5E+06
	7.9E-11	8.1E-01	2.5E+06
	3.0E-10	3.1E+00	2.5E+06
	1.1E-09	1.2E+01	2.5E+06
	4.3E-09	4.4E+01	2.5E+06
	1.6E-08	1.7E+02	2.5E+06
	6.2E-08	6.3E+02	2.5E+06
	2.3E-07	2.4E+03	2.5E+06
	8.9E-07	9.1E+03	2.5E+06
	3.4E-06	3.4E+04	2.5E+06
	1.3E-05	1.3E+05	2.5E+06
	4.8E-05	5.0E+05	2.5E+06
	1.8E-04	1.9E+06	2.5E+06
	7.0E-04	7.1E+06	2.5E+06
	2.6E-03	2.7E+07	2.5E+06
	1.0E-02	1.0E+08	2.5E+06
Extend1	1.0E-13	9.3E-04	2.4E+06
	3.8E-13	3.5E-03	2.2E+06
	1.4E-12	1.3E-02	1.7E+06
	5.5E-12	5.1E-02	1.1E+06
	2.1E-11	1.9E-01	7.9E+05
	7.9E-11	7.3E-01	7.3E+05
	3.0E-10	2.8E+00	7.2E+05
	1.1E-09	1.0E+01	7.1E+05
	4.3E-09	4.0E+01	7.1E+05

	1.6E-08	1.5E+02	7.1E+05
	6.2E-08	5.7E+02	7.1E+05
	2.3E-07	2.2E+03	7.1E+05
	8.9E-07	8.2E+03	7.1E+05
	3.4E-06	3.1E+04	7.1E+05
	1.3E-05	1.2E+05	7.1E+05
	4.8E-05	4.5E+05	7.1E+05
	1.8E-04	1.7E+06	7.1E+05
	7.0E-04	6.4E+06	7.1E+05
	2.6E-03	2.4E+07	7.1E+05
	1.0E-02	9.3E+07	7.1E+05
Extend2	1.0E-13	9.6E-04	2.5E+06
	3.8E-13	3.6E-03	2.4E+06
	1.4E-12	1.4E-02	1.9E+06
	5.5E-12	5.3E-02	1.2E+06
	2.1E-11	2.0E-01	9.2E+05
	7.9E-11	7.5E-01	8.2E+05
	3.0E-10	2.9E+00	7.9E+05
	1.1E-09	1.1E+01	7.8E+05
	4.3E-09	4.1E+01	7.8E+05
	1.6E-08	1.6E+02	7.8E+05
	6.2E-08	5.9E+02	7.8E+05
	2.3E-07	2.3E+03	7.8E+05
	8.9E-07	8.5E+03	7.8E+05
	3.4E-06	3.2E+04	7.8E+05
	1.3E-05	1.2E+05	7.8E+05
	4.8E-05	4.6E+05	7.8E+05
	1.8E-04	1.8E+06	7.8E+05
	7.0E-04	6.7E+06	7.8E+05
	2.6E-03	2.5E+07	7.8E+05
	1.0E-02	9.6E+07	7.8E+05
MtValley	1.0E-13	1.2E-03	2.5E+06
	3.8E-13	4.4E-03	2.7E+06
	1.4E-12	1.7E-02	3.1E+06
	5.5E-12	6.3E-02	3.3E+06
	2.1E-11	2.4E-01	3.4E+06
	7.9E-11	9.1E-01	3.4E+06
	3.0E-10	3.5E+00	3.4E+06
	1.1E-09	1.3E+01	3.4E+06
	4.3E-09	5.0E+01	3.4E+06

	1.6E-08	1.9E+02	3.4E+06
	6.2E-08	7.2E+02	3.4E+06
	2.3E-07	2.7E+03	3.4E+06
	8.9E-07	1.0E+04	3.4E+06
	3.4E-06	3.9E+04	3.4E+06
	1.3E-05	1.5E+05	3.4E+06
	4.8E-05	5.6E+05	3.4E+06
	1.8E-04	2.1E+06	3.4E+06
	7.0E-04	8.1E+06	3.4E+06
	2.6E-03	3.1E+07	3.4E+06
	1.0E-02	1.2E+08	3.4E+06
MtCenter	1.0E-13	9.0E-04	1.5E+06
	3.8E-13	3.4E-03	1.7E+06
	1.4E-12	1.3E-02	2.1E+06
	5.5E-12	4.9E-02	2.3E+06
	2.1E-11	1.9E-01	2.4E+06
	7.9E-11	7.1E-01	2.4E+06
	3.0E-10	2.7E+00	2.4E+06
	1.1E-09	1.0E+01	2.4E+06
	4.3E-09	3.8E+01	2.4E+06
	1.6E-08	1.5E+02	2.4E+06
	6.2E-08	5.5E+02	2.4E+06
	2.3E-07	2.1E+03	2.4E+06
	8.9E-07	8.0E+03	2.4E+06
	3.4E-06	3.0E+04	2.4E+06
	1.3E-05	1.1E+05	2.4E+06
	4.8E-05	4.3E+05	2.4E+06
	1.8E-04	1.6E+06	2.4E+06
	7.0E-04	6.2E+06	2.4E+06
	2.6E-03	2.4E+07	2.4E+06
	1.0E-02	9.0E+07	2.4E+06
Hillslope	1.0E-13	8.0E-04	1.5E+06
	3.8E-13	3.0E-03	1.5E+06
	1.4E-12	1.1E-02	1.5E+06
	5.5E-12	4.3E-02	1.5E+06
	2.1E-11	1.6E-01	1.5E+06
	7.9E-11	6.2E-01	1.5E+06
	3.0E-10	2.4E+00	1.5E+06
	1.1E-09	9.0E+00	1.5E+06
	4.3E-09	3.4E+01	1.5E+06

	1.6E-08	1.3E+02	1.5E+06
	6.2E-08	4.9E+02	1.5E+06
	2.3E-07	1.9E+03	1.5E+06
	8.9E-07	7.1E+03	1.5E+06
	3.4E-06	2.7E+04	1.5E+06
	1.3E-05	1.0E+05	1.5E+06
	4.8E-05	3.8E+05	1.5E+06
	1.8E-04	1.5E+06	1.5E+06
	7.0E-04	5.5E+06	1.5E+06
	2.6E-03	2.1E+07	1.5E+06
	1.0E-02	8.0E+07	1.5E+06

Table E.5: Sensitivity of Discharge and Age to permeability

Model	K (m/s)	DS Divide location (m)	US Divide location (m)
Whole	1.00E-02	11870.5	16873.5
	2.60E-03	11870.5	16873.5
	3.36E-06	11870.5	16873.5
	1.62E-08	11870.5	16873.5
	1.13E-10	11870.5	16873.5
	1.44E-12	11870.5	16873.5
	1.00E-13	11870.5	16873.5
Trad	1.00E-02	11523	16510
	2.60E-03	11523	16510
	3.36E-06	11523	16510
	1.62E-08	11523	16510
	1.13E-10	11523	16510
	1.44E-12	11523	16510
	1.00E-13	11523	16510
Extend1	1.00E-02	11782.5	17277.5
	2.60E-03	11782.5	17277.5
	3.36E-06	11782.5	17277.5
	1.62E-08	11782.5	17277.5
	1.13E-10	11782.5	17277.5
	1.44E-12	11782.5	17277.5
	1.00E-13	11782.5	17277.5
Extend2	1.00E-02	11821.5	16947
	2.60E-03	11821.5	16947
	3.36E-06	11821.5	16947

	1.62E-08	11821.5	16947
	1.13E-10	11821.5	16947
	1.44E-12	11821.5	16947
	1.00E-13	11821.5	16947

Table E.6: Sensitivity of groundwater divide to permeability

E.4 Slope

Model	Slope	Discharge (m^2/s)	Total age flux (m^2yr/s)
Whole	0.05	952	995483
	0.06	954	921480
	0.07	955	858797
	0.08	957	804828
	0.09	958	757410
	0.1	960	715295
	0.11	962	677597
	0.12	964	643300
	0.13	966	612124
	0.14	968	583252
	0.15	971	556959
	0.16	973	532560
	0.17	976	509910
	0.18	979	489016
	0.19	982	469981
	0.2	985	454870
	0.21	988	439749
	0.22	991	426834
	0.23	995	414487
	0.24	998	403312
	0.25	1002	393209
	0.26	1006	384364
	0.27	1010	376053
	0.28	1014	368511
	0.29	1018	362140
	0.3	1023	355194
	0.31	1027	350333
	0.32	1032	346114

	0.33	1037	341986
	0.34	1042	338764
	0.35	1047	334710
	0.36	1053	331192
	0.37	1061	328721
	0.38	1072	324540
	0.39	1086	322789
	0.4	1104	321530
	0.41	1124	319002
	0.42	1148	319153
	0.43	1173	320453
	0.44	1200	321439
	0.45	1228	322647
	0.46	1259	323329
	0.47	1290	323248
	0.48	1323	322710
	0.49	1357	321193
	0.5	1391	319082
Trad	0.05	992	2494593
	0.06	1008	2494338
	0.07	1027	2494029
	0.08	1048	2494154
	0.09	1071	2494330
	0.1	1100	2495236
	0.11	1136	2494245
	0.12	1188	2491144
	0.13	1248	2491586
	0.14	1309	2491553
	0.15	1371	2491410
	0.16	1433	2491292
	0.17	1495	2491222
	0.18	1559	2491191
	0.19	1622	2491188
	0.2	1687	2491204
	0.21	1751	2491234
	0.22	1816	2491272
	0.23	1881	2491316
	0.24	1947	2491363
	0.25	2013	2491414
	0.26	2078	2491463

	0.27	2144	2491517
	0.28	2210	2491568
	0.29	2275	2491617
	0.3	2341	2491664
	0.31	2406	2491709
	0.32	2470	2491752
	0.33	2535	2491791
	0.34	2598	2491827
	0.35	2661	2491859
	0.36	2723	2491885
	0.37	2784	2491906
	0.38	2845	2491926
	0.39	2904	2491935
	0.4	2962	2491943
	0.41	3019	2491942
	0.42	3074	2491939
	0.43	3128	2491927
	0.44	3181	2491908
	0.45	3232	2491883
	0.46	3281	2491846
	0.47	3328	2491807
	0.48	3374	2491759
	0.49	3417	2491701
	0.5	3459	2491636
Extend1	0.05	930	857210
	0.06	927	778257
	0.07	925	712387
	0.08	923	656363
	0.09	922	607976
	0.1	922	565678
	0.11	922	528380
	0.12	923	495247
	0.13	925	465675
	0.14	927	439120
	0.15	931	415176
	0.16	936	393561
	0.17	941	373964
	0.18	948	356221
	0.19	955	340661
	0.2	964	327769

	0.21	974	316820
	0.22	986	307820
	0.23	998	300456
	0.24	1013	294296
	0.25	1028	289279
	0.26	1045	285193
	0.27	1064	281827
	0.28	1084	279023
	0.29	1106	276361
	0.3	1130	273744
	0.31	1156	270388
	0.32	1183	268757
	0.33	1210	269302
	0.34	1237	269609
	0.35	1263	269507
	0.36	1289	269022
	0.37	1314	268176
	0.38	1338	266964
	0.39	1361	265393
	0.4	1383	263459
	0.41	1404	261159
	0.42	1423	258492
	0.43	1441	255456
	0.44	1457	252055
	0.45	1470	248288
	0.46	1482	244171
	0.47	1491	239710
	0.48	1498	234918
	0.49	1502	229810
	0.5	1504	224402
Extend2	0.05	956	917001
	0.06	959	841533
	0.07	962	778239
	0.08	965	723936
	0.09	969	676587
	0.1	973	634789
	0.11	977	597602
	0.12	982	564264
	0.13	987	534203
	0.14	993	506966

	0.15	999	482187
	0.16	1005	459553
	0.17	1012	438828
	0.18	1020	419906
	0.19	1028	402802
	0.2	1037	388873
	0.21	1046	376266
	0.22	1056	365209
	0.23	1066	355999
	0.24	1077	348125
	0.25	1088	341172
	0.26	1100	335545
	0.27	1113	330451
	0.28	1127	326393
	0.29	1141	322546
	0.3	1156	319197
	0.31	1171	316141
	0.32	1187	313282
	0.33	1204	310636
	0.34	1222	307958
	0.35	1240	305056
	0.36	1259	301497
	0.37	1277	301098
	0.38	1294	300773
	0.39	1309	300352
	0.4	1323	299669
	0.41	1336	298774
	0.42	1350	296232
	0.43	1364	293089
	0.44	1380	289650
	0.45	1396	285827
	0.46	1414	281739
	0.47	1432	277220
	0.48	1450	272386
	0.49	1469	267074
	0.5	1488	261398
MtValley	0.05	1086	3338021
	0.06	1123	3363460
	0.07	1163	3384469
	0.08	1205	3402234

	0.09	1251	3418604
	0.1	1304	3427001
	0.11	1376	3420672
	0.12	1455	3420168
	0.13	1534	3419705
	0.14	1613	3419336
	0.15	1691	3419104
	0.16	1770	3418994
	0.17	1849	3418982
	0.18	1927	3419046
	0.19	2005	3419167
	0.2	2083	3419328
	0.21	2161	3419524
	0.22	2239	3419744
	0.23	2317	3419984
	0.24	2394	3420248
	0.25	2471	3420521
	0.26	2547	3420810
	0.27	2623	3421105
	0.28	2699	3421410
	0.29	2775	3421721
	0.3	2849	3422038
	0.31	2924	3422357
	0.32	2997	3422674
	0.33	3070	3422990
	0.34	3142	3423301
	0.35	3214	3423600
	0.36	3285	3423888
	0.37	3354	3424158
	0.38	3423	3424403
	0.39	3491	3424624
	0.4	3557	3424813
	0.41	3623	3424968
	0.42	3687	3425083
	0.43	3750	3425162
	0.44	3811	3425205
	0.45	3871	3425210
	0.46	3929	3425187
	0.47	3986	3425133
	0.48	4040	3425058

	0.49	4093	3424963
	0.5	4144	3424851
MtCenter	0.05	795	2364821
	0.06	847	2392423
	0.07	898	2415512
	0.08	949	2435353
	0.09	1000	2452983
	0.1	1050	2470046
	0.11	1100	2476559
	0.12	1149	2476847
	0.13	1198	2475295
	0.14	1246	2474357
	0.15	1293	2473779
	0.16	1339	2473418
	0.17	1384	2473200
	0.18	1429	2473079
	0.19	1472	2473028
	0.2	1515	2473029
	0.21	1556	2473072
	0.22	1596	2473146
	0.23	1635	2473244
	0.24	1673	2473366
	0.25	1709	2473506
	0.26	1744	2473660
	0.27	1777	2473823
	0.28	1810	2473994
	0.29	1840	2474166
	0.3	1869	2474333
	0.31	1896	2474492
	0.32	1922	2474632
	0.33	1946	2474744
	0.34	1969	2474821
	0.35	1990	2474851
	0.36	2009	2474821
	0.37	2027	2474724
	0.38	2043	2474553
	0.39	2058	2474306
	0.4	2071	2473990
	0.41	2082	2473617
	0.42	2093	2474390

	0.43	2105	2475300
	0.44	2126	2474786
	0.45	2154	2474292
	0.46	2192	2473846
	0.47	2241	2473440
	0.48	2303	2473055
	0.49	2385	2472697
	0.5	2490	2472533
Hillslope	0.05	722	1549365
	0.06	759	1549324
	0.07	796	1549157
	0.08	833	1548943
	0.09	870	1548715
	0.1	906	1548490
	0.11	943	1548269
	0.12	980	1548058
	0.13	1016	1547856
	0.14	1052	1547663
	0.15	1088	1547478
	0.16	1124	1547302
	0.17	1159	1547132
	0.18	1194	1546968
	0.19	1228	1546813
	0.2	1262	1546660
	0.21	1295	1546513
	0.22	1327	1546368
	0.23	1359	1546226
	0.24	1389	1546086
	0.25	1418	1545948
	0.26	1446	1545810
	0.27	1473	1545674
	0.28	1499	1545536
	0.29	1523	1545400
	0.3	1546	1545263
	0.31	1567	1545125
	0.32	1587	1544985
	0.33	1605	1544843
	0.34	1621	1544700
	0.35	1635	1544555
	0.36	1647	1544408

	0.37	1657	1544259
	0.38	1665	1544108
	0.39	1671	1543955
	0.4	1675	1543799
	0.41	1677	1543641
	0.42	1677	1543481
	0.43	1675	1543320
	0.44	1671	1543159
	0.45	1665	1542997
	0.46	1657	1542836
	0.47	1648	1542675
	0.48	1637	1542517
	0.49	1625	1542362
	0.5	1611	1542211

Table E.7: Sensitivity of Discharge and Age to regional slope

Model	**Slope**	**DS Divide location (m)**	**US Divide location (m)**
Whole	0.05	11754.5	16760.5
	0.08	11920.5	16920.5
	0.10	12006.5	17001.5
	0.20	12238.5	17174.5
	0.30	11943.5	16776.5
	0.40	11564.5	16259.5
	0.50	11125.5	15659.5
Trad	0.05	11523.0	16510.0
	0.08	11523.0	16510.0
	0.10	11523.0	16510.0
	0.20	11523.0	16510.0
	0.30	11523.0	16510.0
	0.40	11523.0	16510.0
	0.50	11523.0	16510.0
Extend1	0.05	11680.5	16981.5
	0.08	11827.5	18403.7
	0.10	11905.5	18403.7
	0.20	12073.5	18403.7
	0.30	11591.5	18403.7
	0.40	8428.2	18403.7
	0.50	8428.2	18403.7

Extend2	0.05	11714.5	16805.5
	0.08	11867.5	17010.5
	0.10	11947.5	17121.5
	0.20	12138.5	17403.5
	0.30	11766.5	17060.5
	0.40	11282.5	16541.5
	0.50	6535.2	15891.5

Table E.8: Sensitivity of groundwater divide location to regional slope

E.5 Amplitude

Model	Amplitude (m)	Discharge (m^2/s)	Total age flux (m^2yr/s)
Whole	50	322	430349
	77.5	496	593659
	105	670	714964
	132.5	844	808640
	160	1018	884934
	187.5	1193	949207
	215	1367	1004500
	242.5	1541	1053396
	270	1715	1097247
	297.5	1889	1136625
	325	2063	1172489
	352.5	2237	1205352
	380	2411	1235870
	407.5	2586	1264069
	435	2760	1290738
	462.5	2934	1315473
	490	3108	1338984
	517.5	3282	1361055
	545	3456	1382268
	572.5	3630	1402524
	600	3804	1421222
Trad	50	553	2489267
	77.5	646	2490422
	105	762	2495395
	132.5	922	2494133

	160	1087	2494103
	187.5	1255	2494460
	215	1424	2494606
	242.5	1594	2494661
	270	1764	2494732
	297.5	1934	2494813
	325	2105	2494897
	352.5	2275	2494985
	380	2446	2495072
	407.5	2617	2495146
	435	2788	2495230
	462.5	2960	2495311
	490	3131	2495388
	517.5	3302	2495361
	545	3473	2495154
	572.5	3645	2494891
	600	3816	2494730
Extend1	50	297	280475
	77.5	468	437831
	105	641	561093
	132.5	815	659162
	160	988	740272
	187.5	1162	809154
	215	1336	868860
	242.5	1510	921396
	270	1685	968251
	297.5	1859	1010383
	325	2033	1048650
	352.5	2207	1083592
	380	2382	1115802
	407.5	2556	1145413
	435	2730	1173042
	462.5	2905	1198714
	490	3079	1222940
	517.5	3253	1245938
	545	3428	1267030
	572.5	3602	1286721
	600	3776	1305615
Extend2	50	331	343031
	77.5	504	506405

	105	678	630002
	132.5	851	726470
	160	1025	805224
	187.5	1199	871694
	215	1372	929139
	242.5	1546	979646
	270	1720	1024673
	297.5	1894	1065369
	325	2068	1102316
	352.5	2241	1136272
	380	2415	1167552
	407.5	2589	1196673
	435	2763	1223801
	462.5	2937	1249099
	490	3111	1273094
	517.5	3284	1295583
	545	3458	1316791
	572.5	3632	1337470
	600	3806	1356935
MtValley	50	721	3417049
	77.5	815	3418150
	105	912	3427032
	132.5	1061	3401447
	160	1221	3375267
	187.5	1385	3351907
	215	1550	3331062
	242.5	1716	3312401
	270	1883	3295603
	297.5	2050	3280300
	325	2217	3266288
	352.5	2385	3253434
	380	2553	3241633
	407.5	2721	3230748
	435	2889	3220677
	462.5	3057	3211353
	490	3225	3202643
	517.5	3393	3194525
	545	3561	3186891
	572.5	3730	3179740
	600	3898	3172999

MtCenter	50	553	2473375
	77.5	646	2474714
	105	741	2470261
	132.5	837	2435243
	160	933	2404990
	187.5	1029	2378611
	215	1126	2355490
	242.5	1222	2335062
	270	1319	2316847
	297.5	1416	2300484
	325	1512	2285660
	352.5	1609	2272157
	380	1706	2259801
	407.5	1802	2248506
	435	1899	2238127
	462.5	1996	2228652
	490	2093	2220016
	517.5	2189	2212050
	545	2286	2204723
	572.5	2383	2198081
	600	2480	2191995
Hillslope	50	434	1547143
	77.5	534	1548017
	105	633	1548601
	132.5	733	1548988
	160	832	1549230
	187.5	931	1549360
	215	1031	1549395
	242.5	1130	1549346
	270	1230	1549218
	297.5	1329	1549020
	325	1428	1548763
	352.5	1528	1548473
	380	1627	1548189
	407.5	1727	1547960
	435	1826	1547829
	462.5	1925	1547811
	490	2025	1547882
	517.5	2124	1548001
	545	2224	1504880

	572.5	2323	1509276
	600	2423	1513433

Table E.9: Sensitivity of Discharge and Age to hummock amplitude

Model	Amplitude (m)	DS Divide location (m)	US Divide location (m)
Whole	10	12375.5	17547.5
	62	12366.5	17384.5
	114	11996.5	17002.5
	218	11726.5	16725.5
	531	11491.5	16485.5
	791	11421.5	16415.5
	1000	11389.5	16381.5
Trad	10	11523.0	16510.0
	62	11523.0	16510.0
	114	11523.0	16510.0
	218	11523.0	16510.0
	531	11523.0	16510.0
	791	11523.0	16510.0
	1000	11523.0	16510.0
Extend1	10	11523.0	18403.7
	62	12254.5	18403.7
	114	11899.5	18403.7
	218	11652.5	16930.5
	531	11452.5	16541.5
	791	11398.5	16453.5
	1000	11373.5	16415.5
Extend2	10	6535.2	21498.6
	62	12291.5	17657.5
	114	11940.5	17114.5
	218	11686.5	16766.5
	531	11471.5	16491.5
	791	11410.5	16416.5
	1000	11381.5	16382.5

Table E.10: Sensitivity of groundwater divide location to hummock amplitude

E.6 Permeability Decay with Depth

	Decay constant (β)	Discharge (m^2/s)	Total age flux (m^2yr/s)
Whole	0.001	644	1095588
	0.002	458	1456124
	0.003	346	2518451
	0.004	274	2561014
	0.005	226	2589037
	0.006	191	2620654
	0.007	166	2654633
	0.008	146	2692013
	0.009	130	2730677
	0.01	118	2769477
	0.02	60	3169698
	0.03	40	3613299
	0.04	30	4070960
	0.05	24	4541792
	0.06	20	5029230
	0.07	17	5535257
	0.08	15	6060538
	0.09	13	6605267
	0.1	12	7169481
Trad	0.001	660	2495110
	0.002	462	2495536
	0.003	346	2501097
	0.004	274	2505111
	0.005	226	2509572
	0.006	191	2514651
	0.007	166	2519464
	0.008	146	2525746
	0.009	130	2532336
	0.01	118	2538856
	0.02	60	2604562
	0.03	40	2668743
	0.04	30	2729382
	0.05	24	2788361
	0.06	20	2847516
	0.07	17	2906836
	0.08	15	2966752
	0.09	13	3027370

	0.1	12	3088741
Extend1	0.001	643	890015
	0.002	458	1138823
	0.003	346	2033005
	0.004	274	2474202
	0.005	226	2516107
	0.006	191	2532825
	0.007	166	2545276
	0.008	146	2558383
	0.009	130	2571661
	0.01	118	2584844
	0.02	60	2718030
	0.03	40	2851886
	0.04	30	2978959
	0.05	24	3109887
	0.06	20	3239046
	0.07	17	3369966
	0.08	15	3503085
	0.09	13	3638639
	0.1	12	3776785
Extend2	0.001	645	986088
	0.002	458	1259476
	0.003	346	2338794
	0.004	274	2516932
	0.005	226	2536889
	0.006	191	2553732
	0.007	166	2570458
	0.008	146	2589162
	0.009	130	2608546
	0.01	118	2628047
	0.02	60	2829008
	0.03	40	3037309
	0.04	30	3237543
	0.05	24	3448660
	0.06	20	3657156
	0.07	17	3869928
	0.08	15	4087767
	0.09	13	4311058
	0.1	12	4539970
MtValley	0.001	676	3273502

	0.002	464	3151132
	0.003	347	2931854
	0.004	274	2744758
	0.005	226	2663291
	0.006	191	2625113
	0.007	166	2605874
	0.008	146	2598010
	0.009	130	2595972
	0.01	118	2597115
	0.02	60	2662179
	0.03	40	2746185
	0.04	30	2829670
	0.05	24	2912497
	0.06	20	2996437
	0.07	17	3081163
	0.08	15	3167170
	0.09	13	3254539
	0.1	12	3343304
MtCenter	0.001	512	2319278
	0.002	337	2202590
	0.003	246	1976864
	0.004	192	1789681
	0.005	157	1704412
	0.006	132	1658532
	0.007	114	1636395
	0.008	101	1621803
	0.009	90	1613345
	0.01	81	1608480
	0.02	41	1623834
	0.03	27	1660569
	0.04	20	1697134
	0.05	16	1733110
	0.06	14	1769445
	0.07	12	1805906
	0.08	10	1842810
	0.09	9	1880234
	0.1	8	1918212
Hillslope	0.001	496	1550166
	0.002	335	1551178
	0.003	246	1551111

	0.004	192	1551736
	0.005	157	1552840
	0.006	132	1554197
	0.007	114	1555082
	0.008	101	1557043
	0.009	90	1559176
	0.01	81	1561249
	0.02	41	1585934
	0.03	27	1611347
	0.04	20	1634822
	0.05	16	1657261
	0.06	14	1679537
	0.07	12	1701641
	0.08	10	1723786
	0.09	9	1746053
	0.1	8	1768475

Table E.11: Sensitivity of Discharge and Age to decay depth

Model	**Decay constant (β)**	**DS Divide location (m)**	**US Divide location (m)**
Whole	1.00E-03	11720.5	16708.5
	5.00E-03	11542.5	16529.5
	1.00E-02	11528.5	16515.5
	5.00E-02	11524.5	16511.5
	1.00E-01	11525.5	16511.5
Trad	1.00E-03	11523	16510
	5.00E-03	11523	16510
	1.00E-02	11523	16510
	5.00E-02	11523	16510
	1.00E-01	11523	16510
Extend1	1.00E-03	11709.5	16732.5
	5.00E-03	11542.5	16529.5
	1.00E-02	11527.5	16515.5
	5.00E-02	11523.5	16511.5
	1.00E-01	11523.5	16511.5
Extend2	1.00E-03	11717.5	16710.5
	5.00E-03	11541.5	16529.5
	1.00E-02	11527.5	16515.5
	5.00E-02	11523.5	16510.5

	1.00E-01	11523.5	16510.5

Table E.12: Sensitivity of groundwater divide location to decay depth

E.7 Anisotropy

	K_h/K_v	Discharge (m^2/s)	Total age flux (m^2yr/s)
Whole	0.01	99	245203
	0.02	141	246417
	0.03	172	259039
	0.04	199	273421
	0.05	222	287669
	0.06	244	301534
	0.07	263	314848
	0.08	281	327460
	0.09	298	339599
	0.1	313	351140
	0.2	439	446011
	0.3	534	519330
	0.4	613	581437
	0.5	682	636658
	0.6	745	687077
	0.7	803	733731
	0.8	857	777596
	0.9	907	819197
	1	955	858797
Trad	0.01	103	2634574
	0.02	145	2621319
	0.03	178	2634674
	0.04	206	2630931
	0.05	230	2614844
	0.06	252	2595326
	0.07	272	2577441
	0.08	291	2562789
	0.09	308	2551238
	0.1	325	2541847
	0.2	460	2507384
	0.3	563	2499370

	0.4	650	2496497
	0.5	727	2495257
	0.6	796	2494662
	0.7	860	2494352
	0.8	919	2494183
	0.9	974	2494086
	1	1027	2494029
Extend1	0.01	92	131148
	0.02	130	143481
	0.03	159	158817
	0.04	184	173698
	0.05	206	187732
	0.06	225	200944
	0.07	244	213416
	0.08	260	225244
	0.09	276	236505
	0.1	291	247256
	0.2	412	336430
	0.3	504	405985
	0.4	583	464512
	0.5	652	515693
	0.6	715	561580
	0.7	772	603422
	0.8	826	642129
	0.9	877	678297
	1	925	712388
Extend2	0.01	97	172375
	0.02	137	182316
	0.03	168	197173
	0.04	194	212063
	0.05	217	226391
	0.06	238	240003
	0.07	257	252969
	0.08	275	265317
	0.09	292	277142
	0.1	307	288502
	0.2	435	383083
	0.3	532	456512
	0.4	613	517770
	0.5	684	571080

	0.6	748	618939
	0.7	807	662786
	0.8	862	703550
	0.9	913	741877
	1	962	778239
MtValley	0.01	117	3715799
	0.02	166	3666096
	0.03	203	3614077
	0.04	235	3570257
	0.05	262	3539759
	0.06	287	3518507
	0.07	310	3502975
	0.08	332	3491089
	0.09	352	3481196
	0.1	371	3473924
	0.2	524	3434983
	0.3	642	3419017
	0.4	741	3409973
	0.5	828	3403827
	0.6	906	3399057
	0.7	978	3394997
	0.8	1044	3391309
	0.9	1105	3387836
	1	1163	3384469
MtCenter	0.01	90	2528167
	0.02	127	2542722
	0.03	156	2571020
	0.04	180	2576674
	0.05	201	2566519
	0.06	220	2550533
	0.07	238	2534661
	0.08	255	2521168
	0.09	270	2509253
	0.1	285	2501685
	0.2	403	2465916
	0.3	493	2453419
	0.4	569	2445366
	0.5	636	2439008
	0.6	697	2433452
	0.7	753	2428596

	0.8	804	2424013
	0.9	853	2419676
	1	898	2415509
Hillslope	0.01	80	1570362
	0.02	113	1566534
	0.03	138	1571036
	0.04	159	1580311
	0.05	178	1589942
	0.06	195	1596249
	0.07	211	1598824
	0.08	225	1598735
	0.09	239	1596991
	0.1	252	1594342
	0.2	356	1569683
	0.3	436	1559573
	0.4	503	1555120
	0.5	563	1552790
	0.6	617	1551413
	0.7	666	1550527
	0.8	712	1549842
	0.9	755	1549483
	1	796	1549155

Table E.13: Sensitivity of Discharge and Age to K_h/K_v

E.8 Heterogeneity

	Dip angle(°)	**Discharge (m^2/s)**	**Total age flux (m^2yr/s)**
Whole	45	35231	1224348
	30	30615	1109440
	15	23568	788384
Trad	45	35637	2568614
	30	30935	2464898
	15	22971	2526943
Extend1	45	36213	1676061
	30	32252	1778991
	15	23941	727631
Extend2	45	35400	1088854
	30	31631	1170335

	15	23735	688443

Table E.14: Sensitivity of dishcarge and age to heterogeneous layers at different dip angles

Model	Dip angle(°)	DS Divide location (m)	US Divide location (m)
Whole	15	12088.5	17447.5
	30	12454.5	17444.5
	45	12448.5	17436.5
Trad	15	11523	16510
	30	11523	16510
	45	11523	16510
Extend1	15	11198.5	17473.5
	30	11268.5	17477.5
	45	11606.5	17466.5
Extend2	15	11600.5	17467.5
	30	11573.5	17471.5
	45	12444.5	17452.5

Table E.15: Sensitivity of groundwater divide location to heterogeneous layers at different dip angles